Analysis and mitigation of the nonlinear impairments in fiber-optic communication systems

ANALYSIS AND MITIGATION OF THE NONLINEAR IMPAIRMENTS IN FIBER-OPTIC COMMUNICATION SYSTEMS

BY

SINA NADERI SHAHI, M.A.Sc.

A THESIS

SUBMITTED TO THE DEPARTMENT OF ELECTRICAL AND COMPUTER ENGINEERING

AND THE SCHOOL OF GRADUATE STUDIES

OF MCMASTER UNIVERSITY

IN PARTIAL FULFILMENT OF THE REQUIREMENTS

FOR THE DEGREE OF

DOCTOR OF PHILOSOPHY

Doctor of Philosophy (2013) McMaster University

(Electrical and Computer Engineering) Hamilton, Ontario, Canada

TITLE:	Analysis and mitigation of the nonlinear impairments in fiber-optic communication systems
AUTHOR:	Sina Naderi Shahi M.Sc., (Electrical Engineering) Sharif University of Technology, Tehran, Iran
SUPERVISOR:	Dr. Shiva Kumar
NUMBER OF PAGES:	xxiii, 148

To my beloved parents

Abstract

Fiber-optic communication systems have revolutionized the telecommunications industry and have played a major role in the advent of the *Information Age*. Thousands of kilometers of optical fiber are used by telecommunications companies to transmit telephone signals, Internet communication, and cable television signals throughout the world. So, working in this area has always been interesting. This thesis analyzes the nonlinearity of fiber-optic systems and proposes a system to mitigate fiber nonlinear effects. The topics of this thesis can be categorized into two parts. In the first part of thesis (Chapters 2, 3, and 4), analytical models are developed for fiber-optic nonlinear effects. It is important to have an accurate analytical model so that the impact of a specific system/signal parameter on the performance can be assessed quickly without doing time-consuming Monte-Carlo simulations. In the second part (Chapters 5, and 6), a multi-core/fiber architecture is proposed to reduce the nonlinear effects.

In Chapter 2, intrachannel nonlinear impairments are studied and an analytical model for the calculation of power spectral density (PSD) and variance of the nonlinear distortion is obtained based on quadrature phase-shift keying (QPSK) signal. For QPSK signals, intrachannel four-wave mixing (IFWM) is the only stochastic nonlinear distortion. To develop the analytical model, a first order perturbation theory

is used. For a Gaussian pulse shape, a closed form formula is obtained for the PSD of IFWM. For non-Gaussian pulses, it is not possible to find the PSD analytically. However, using stationary phase approximation approach, convolutions become multiplications and a simple analytical expression for the PSD of the nonlinear distortion can be found. The total PSD is obtained by adding the PSD of amplified spontaneous emission (ASE) PSD to that of the nonlinear distortion. Using the total PSD, bit error ratio (BER) can be obtained analytically for a QPSK system. The analytically estimated BER is found to be in good agreement with numerical simulations. Significant computational effort can be saved using the analytical model as compared to numerical simulations, without sacrificing much accuracy.

In Chapter 3, the same approach as that in Chapter 2 is used to find an analytical expression for the PSD of the intrachannel nonlinear distortion of a fiber-optic system based on quadrature amplitude modulation (QAM) signal. Unlike the QPSK signal, intrachannel cross-phase modulation (IXPM) is a stochastic process for the QAM signal which leads to the increase of the nonlinear distortion variance. In this chapter, analytical expressions for the PSDs of self-phase modulation (SPM), IXPM, IFWM, and their correlations are obtained for the QAM signal. Simulation results show good agreement between the analytical model and numerical simulation.

In Chapter 4, inter-channel nonlinear impairment is studied. This time, a first order perturbation technique is used to develop an analytical model for SPM and cross-phase modulation (XPM) distortions in a wavelength division multiplexing (WDM) system based on QAM. In this case, SPM distortion is deterministic and does not contribute to the nonlinear noise variance. On the other hand, XPM is stochastic and contributes to the noise variance. In this chapter, effects of input launch power,

fiber dispersion, system reach, and channel spacing on the nonlinear noise variance are investigated as well.

In Chapter 5, a single-channel multi-core/fiber architecture is proposed to reduce intrachannel fiber nonlinear effects. Based on the analytical model obtained in the first part of thesis, the nonlinear distortion variance scales as P^3, where P is the fiber input launch power, which suggests that decreasing the fiber input power can reduce the nonlinear distortion significantly. In this system, the input power is divided between multiple cores/fibers by a power splitter at the input of each span and a power combiner adds the output fields of multiple cores/fibers so that one amplifier can be used for each span. In this case, each core/fiber receives less power and hence adds less nonlinear distortion to the signal. In a practical system, individual fiber parameters are not identical; so the optical pulses propagating in the fibers undergo different amounts of phase shifts and timing delays due to the fluctuations of fibers' propagation constants and fibers' inverse group speeds. Optical and electrical equalizers are proposed to compensate for these inter-core/fiber dispersions. In the case of an optical equalizer, adaptive time shifters and phase shifters are adjusted such that the maximum power is obtained at the output of power combiner. Our numerical simulation results show that for unrepeatered systems, the performance (Q factor) is improved by 6.2 dB using 8-core/fiber configuration as compared to single-core fiber system. In addition, for multi-span system, the transmission reach at BER of 2.1×10^{-3} is quadrupled in 8-core/fiber configuration.

In Chapter 6, a multi-channel multi-core/fiber architecture is proposed to reduce the inter-channel nonlinear distortions. In this architecture, different channels of a

WDM system are interleaved between multiple cores/fibers which increases the channel spacing in each core/fiber. Higher channel spacing decreases the inter-channel nonlinear impairments in each core/fiber which leads to system performance improvement. At the end of each span, a multiplexer adds the channels from different cores/fibers so that one amplifier can be used for all of the channels. Unlike the single-channel multi-core/fiber system, the WDM multi-core/fiber system does not require equalizers since different cores/fibers carry channels with different frequencies. Simulation results show that for a 39-span system, the 4-core/fiber system with negligible crosstalk outperforms the single-core system by 2.2 dBQ_{20}. The impact of crosstalk between cores of a multi-core fiber (MCF) on the system performance is studied. The simulation results show that the performance of the multi-core WDM system is less sensitive to the crosstalk effect compared to conventional multi-core systems since the propagating channels in the cores are not correlated in frequency domain.

Acknowledgements

First, I would like to give my deepest gratitude to my parents who gave me strength and courage to face the difficulties in life. Second, I am deeply grateful to my supervisor, Dr. Shiva Kumar whom I have learned many lessons from. Third, I would like to thank the committee members, Dr. Max Wong, Dr. Steve Hranilovic, and Dr. Xun Li, for their helpful comments during my research. Last but not least, I would like to thank ECE department staff, specially Cheryl Gies, for providing me all the conveniences and helps in my study.

Notation and abbreviations

ASE	amplified spontaneous emission
AWGN	additive white Gaussian noise
BER	bit error ratio
CDMA	code division multiple access
CSI	channel state information
DCF	dispersion compensating filter
D-IFWM	degenerate intrachannel four-wave mixing
DSF	dispersion-shifted fiber
DSP	digital signal processing
EDFA	erbium-doped fiber amplifier
ESP	electrical signal processing
FWHF	full width at half maximum
FWM	four-wave mixing
GVD	group velocity distortion
IFWM	intrachannel four-wave mixing
IM-DD	intensity-modulation direct-detection
ISI	inter-symbol interference
IXPM	intrachannel cross-phase modulation

LMS	least mean square
LO	local oscillator
LPF	low pass filter
MCF	multi-core fiber
MF	matched filter
MMF	multi-mode fiber
MZM	Mach-Zehnder modulator
ND-IFWM	non-degenerate intrachannel four-wave mixing
NLPN	nonlinear phase noise,
NLSE	nonlinear Schrodinger equation
OFDM	orthogonal frequency-division multiplexing
PBS	polarization beam splitter
PDF	probability density function
PDM	polarization-division multiplexing
PLL	phase-locked loop
PMD	polarization mode dispersion
PM-QPSK	polarization multiplexed quadrature phase-shift keying
PRBS	pseudo-random bit sequence
PSD	power spectral density
PSK	phase-shift keying
QAM	quadrature amplitude modulation
QPSK	quadrature phase-shift keying
RZ	return-to-zero

SDM	spatial-division multiplexing
SE	spectral efficiency
SLM	spatial light modulator
SMF	single-mode fiber
SNR	signal-to-noise ratio
SPM	self-phase modulation
SRS	stimulated Raman scattering
TF	transmission fiber
WDM	wavelength division multiplexing
XPM	cross-phase modulation

Contents

Abstract **iv**

Acknowledgements **viii**

Notation and abbreviations **ix**

1 Introduction **1**

1.1 Evolution of fiber-optic communication system 1

1.1.1 WDM system 5

1.1.2 Multi-core fibers 7

1.2 Impairments in fiber-optic communication systems 8

1.2.1 Noise 8

1.2.2 Linear distortions 9

1.2.3 Kerr nonlinearity 13

1.3 Thesis layout 23

1.4 Publications list 26

2 Analytical modeling of a single channel nonlinear fiber-optic system based on QPSK **29**

2.1 Introduction 29
2.2 Mathematical derivation of power spectral density 31
2.2.1 ND-IFWM 36
2.2.2 D-IFWM 37
2.2.3 Correlation between D-IFWM and ND-IFWM 38
2.2.4 Total PSD 38
2.2.5 Stationary phase approximation 39
2.2.6 Variance 42
2.2.7 Computational cost 43
2.3 Results and discussions 44
2.3.1 Stationary phase approximation with raised-cosine pulse . . . 48
2.3.2 BER calculation 50
2.4 Conclusions 52

3 Analytical modeling of a single channel nonlinear fiber-optic system based on QAM 54

3.1 Introduction 54
3.2 Mathematical expression for power spectral density 56
3.2.1 ND-IFWM 57
3.2.2 D-IFWM 57
3.2.3 IXPM 57
3.2.4 SPM 58
3.2.5 IXPM and SPM correlation 59
3.2.6 Total PSD 60
3.3 Simulation results 61

3.4 Conclusions 64

4 Analytical modeling of XPM in WDM fiber-optic system based on QAM 65

4.1 Introduction 65

4.2 SPM and XPM analytical model 67

4.3 Variance calculation 72

4.4 Results and discussion 75

4.5 Conclusions 83

5 Reduction of nonlinear impairments in fiber transmission system using fiber and/or transmitter diversity 84

5.1 Introduction 84

5.2 Multi-core/fiber system configuration 86

5.3 Polarization mode dispersion effect 95

5.4 Simulation setup and results 97

5.4.1 Case 1: unrepeatered fiber system with fiber diversity and optical equalizer 100

5.4.2 Case 2: unrepeatered fiber system with fiber diversity and transmitter diversity 100

5.4.3 Case 3: multi-span fiber system with in-line optical equalizers 102

5.4.4 Case 4: multi-span fiber system with optical equalizers at the receiver 103

5.4.5 Case 5: effect of PMD 104

5.5 Conclusions 107

6 A multi-core or multi-fiber WDM system **109**

6.1 Introduction 109

6.2 Multi-core or multi-fiber WDM System Configuration 112

6.3 Simulation results 114

6.3.1 Inter-core crosstalk effect 118

6.4 Conclusions 124

7 Conclusions and future work **126**

A Gaussian pulse case **130**

B Stationary phase approximation **134**

C Differential equation solution **138**

List of Figures

1.1 Increase in the BL product through several generations [1]. 3

1.2 Historical evolution of record capacity in fiber-optic communication systems (multi-channel and single channel) [7]. 4

1.3 Block diagram of a WDM system. 5

1.4 Frequency spectrum of 12 WDM channels. Each channel symbol rate = 25 Gbaud, channel spacing = 50 GHz. 6

1.5 Cross-section of a 7-core fiber. 7

1.6 Illustration of pulse broadening effect due to PMD. 9

1.7 Illustration of pulse broadening effect due to GVD after 50 km. . . . 11

1.8 Block diagram of a multi-span fiber-optic system with DCF. 11

1.9 Received signal (a) constellation diagram, and (b) eye diagram, before dispersion compensation. QPSK modulation, $\beta_2 = -22.1$ ps^2/km, Number of spans $N = 20$, and fiber nonlinearity was ignored. 12

1.10 Received signal (a) constellation diagram, and (b) eye diagram, after dispersion compensation. Parameters are same as Fig. 1.9 12

1.11 Typical BER vs. launch power curve in a fiber-optic system. 14

1.12 Nonlinear interactions in fiber-optic system [7]. NLPN: nonlinear phase noise, SPM: self-phase modulation, IXPM: intrachannel cross-phase modulation, IFWM: intrachannel four-wave mixing, XPM: cross-phase modulation, FWM: four-wave mixing. 14
1.13 (a) A Gaussian pulse in time domain, and (b) frequency chirp $\delta\omega$ caused by fiber nonlinearity for Gaussian pulse. 16
1.14 Input pulse (input), output in linear regime (Lin: $\gamma_0 = 0$ W^{-1}km^{-1}), and output in nonlinear regime (Lin+SPM: $\gamma_0 = 2.43$ W^{-1}km^{-1}) for (a) normal dispersion $\beta_2 = 10$ ps^2/km, and (b) anomalous dispersion $\beta_2 = -10$ ps^2/km. Following parameters were assumed: $P_{peak} = 8$ mW, $T_{FWHM} = 50$ ps, no. of spans $= 1 \times 80$ km. 17
1.15 Input pulses and output pulses after DCF for (a) normal dispersion $\beta_2 = 10$ ps^2/km, and (b) anomalous dispersion $\beta_2 = -10$ ps^2/km. Following parameters were assumed: $\gamma_0 = 2.43$ W^{-1}km^{-1}, $P_{peak} = 11$ dBm, $T_{FWHM} = 20$ ps, no. of spans $= 5 \times 80$ km. 18
1.16 Input pulses and output pulses after DCF in (a) linear scale , and (b) logarithmic scale. Following parameters were assumed: $\beta_2 = 10$ ps^2/km, $\gamma_0 = 2.43$ W^{-1}km^{-1}, $P_{peak} = 11$ dBm, $T_{FWHM} = 25$ ps, no. of spans $= 8 \times 80$ km. 19
1.17 Input pulses for channels 1 and 2. The following parameters were assumed: $P_{peak} = 8$ mW, $T_{FWHM} = 50$ ps, channel spacing = 50 GHz, $\beta_2 = -10$ ps^2/km, $\gamma_0 = 2.43$ W^{-1}km^{-1}, fiber loss = 0.2 dB/km, and span length 80 km 21

1.18 Frequency spectrum of channels 1 and 2 at the input. Parameters are same as that of Fig. 1.17 21
1.19 Output pulses for channels 1 and 2. Parameters are same as that of Fig. 1.17 22
1.20 Channel 1 output pulse when (1) Lin: $\gamma_0 = 0$ W^{-1}km^{-1}, (2) Lin+SPM: no pulse presents in channel 2, and (3) Lin+SPM+XPM: both channels are present. Parameters are same as that of Fig. 1.17 22
1.21 Three WDM channels and generated FWM sidebands. 23
2.1 Classification of intrachannel nonlinear impairments ($N = 6$). 43
2.2 Block diagram of the system used for the simulation. TF: transmission fiber, and DCF: dispersion compensating fiber. 45
2.3 Analytical and numerical variances vs. peak power for (a) 5-span, and (b) 20-span system ($\beta_2 = -21$ ps^2/km). 47
2.4 Analytical and numerical variances vs. dispersion parameter for (a) 5-span, and (b) 20-span system ($P_{peak} = 0$ dBm). 47
2.5 Validation of the stationary phase approximation. Analytical and numerical variances vs. launch peak power for (a) 5-span, and (b) 20-span system. Raised-cosine pulses are used. $\beta_2 = -21$ ps^2/km. 49
2.6 Validation of the stationary phase approximation. Analytical and numerical variances vs. dispersion parameter for (a) 5-span, and (b) 20-span system. Raised-cosine pulses are used. $P = 0$ dBm. 49
2.7 Analytical and numerical BER vs. average launch power. Gaussian pulses are used. Number of spans = 20 and $\beta_2 = -9.1$ ps^2/km. . . . 52

3.1 Analytical and numerical variances vs. mean launch power for a 10-span system, $D = 17$ ps/nm.km. 62
3.2 Analytical and numerical variances vs. dispersion parameter for a 10-span system, $P_{av} = 4$ dBm. 63
4.1 Multispan WDM fiber-optic system. 76
4.2 Channel 1 and 2 (a) input signals, and (b) output signals. Following parameters were assumed: no. of symbols in channel 1 = 1, no. of symbols in channel 2 = 18, $P_{peak} = 0$ dBm, $\beta_2 = -10$ ps^2/km, no. of spans = 10. 77
4.3 Numerical and analytical SPM and XPM signals induced on channel 1. Parameters are same as that of Fig. 4.2. 78
4.4 One realization of Monte-Carlo simulation: (a) Channels 1 and 2 input signals in time domain. (b) Channels 1 and 2 output signals in time domain. Following parameters were assumed: no. of symbols in channel 1 = 1, no. of symbols in channel 2 = 38, $P_{peak} = 0$ dBm, $\beta_2 = -10$ ps^2/km, and no. of spans = 10. 79
4.5 (a) Absolute value of mean of XPM impairment, and (b) Mean of absolute square of XPM impairment. No. of Monte-Carlo simulations = 2000, and the other parameters are same as that of Fig. 4.4. 79
4.6 Variance of XPM impairment. Parameters are same as that of Fig. 4.4. 80
4.7 XPM variance versus peak power. Following parameters were assumed: no. of symbols in channel 1 = 1, no. of symbols in channel 2 = 38, $\beta_2 = -10$ ps^2/km, no. of spans = 10, no. of Monte-Carlo simulations = 2000. 81

4.8 XPM variance versus fiber dispersion. Following parameters were assumed: no. of symbols in channel 1 = 1, no. of symbols in channel 2 = 76, P_{peak} = 0 dBm, no. of spans = 10, no. of Monte-Carlo simulations = 2000. 81

4.9 XPM variance versus no. of spans. Following parameters were assumed: no. of symbols in channel 1 = 1, no. of symbols in channel 2 = 71, P_{peak} = 0 dBm, $\beta_2 = -10$ ps^2/km, no. of Monte-Carlo simulations = 2000. 82

4.10 XPM variance versus channel spacing. Following parameters were assumed: no. of symbols in channel 1 = 1, no. of symbols in channel 2 = 10, P_{peak} = 0 dBm, $\beta_2 = -10$ ps^2/km, no. of spans = 10, no. of Monte-Carlo simulations = 2000. 82

5.1 Multi-core/fiber system architecture; M: number of cores/fibers; N: number of spans; Opt. Tx.: optical transmitter; PS: power splitter; PC: power combiner; Amp: amplifier; Opt. Rx.: optical receiver. . . . 87

5.2 One realization of fiber-optic channel frequency response for single-core fiber and 2-core/fiber systems. Following parameters were assumed: No. of OFDM channels: 1024, $\sigma_{\beta_0} = 0$ rad/m and $\sigma_{\beta_1} = 10^{-3}$ ps/m. . 89

5.3 One realization of fiber-optic channel frequency response for single-core fiber and 2-core/fiber systems. Following parameters were assumed: No. of OFDM channels: 1024, $\sigma_{\beta_0} = 10^4$ rad/m and $\sigma_{\beta_1} = 0$ ps/m. . . 90

5.4 Similarity between inter-core/fiber dispersion effect in multi-core/fiber system and multipath effect in wireless system. 90

5.5 Unrepeatered multi-core/fiber system architecture with optical equalizer; M: number of cores/fibers; Opt. Tx.: optical transmitter; PS: power splitter; PC: power combiner; PM: power meter; ESP: electrical signal processor; Amp: amplifier; Opt. Rx.: optical receiver. 92
5.6 Multi-span multi-core/fiber system architecture with in-line optical equalizer; M: number of cores/fibers; N: number of spans; Opt. Tx.: optical transmitter; PS: power splitter; PC: power combiner; PM: power meter; ESP: electrical signal processor; Amp: amplifier; Opt. Rx.: optical receiver. 92
5.7 Multi-span multi-core/fiber system architecture with optical equalizer at the receiver; M: number of cores/fibers; N: number of spans; Opt. Tx.: optical transmitter; PS: power splitter; PC: power combiner; PM: power meter; ESP: electrical signal processor; Amp: amplifier; Opt. Rx.: optical receiver. 93
5.8 Unrepeatered multi-core/fiber system architecture with multi-transmitter (electrical equalizer); M: number of cores/fibers; Opt. Tx.: optical transmitter; PC: power combiner; Amp: amplifier; Opt. Rx.: optical receiver; CSI: channel state information. 94
5.9 Multi-span multi-core/fiber system architecture with optical equalizer at the receiver; M: number of cores/fibers; N: number of spans; Opt. Tx.: Optical Transmitter; PS: Power Splitter; PC: Power Combiner; PBS: polarization beam splitter; PM: Power Meter; ESP: electrical signal processor; Amp: Amplifier; Opt. Rx.: Optical Receiver. 97

5.10 Optical OFDM system; IDFT: inverse discrete Fourier transform; DFT: discrete Fourier transform; A/D: analog to digital converter; D/A: digital to analog converter; LO: local oscillator; LPF: low pass filter. . . 99
5.11 BER vs. Launch Power for 300 km unrepeatered fiber with optical equalizer (QPSK modulation). 101
5.12 BER_{min} vs. Transmission Distance for unrepeatered fiber with optical equalizer (QPSK modulation). 101
5.13 BER vs. Launch Power for 300 km unrepeatered fiber with electrical equalizer (QPSK modulation). 102
5.14 BER vs. Launch Power after 5 spans (400 km) with in-line optical equalizer (64-QAM). 103
5.15 BER_{min} vs. Transmission Distance for multi-span fiber system with in-line optical equalizer (64-QAM). 104
5.16 BER vs. Launch Power after 5 spans (400 km) with optical equalizer at the receiver (64-QAM). 105
5.17 BER vs. Launch Power after 5 spans (400 km) with optical equalizer (64-QAM). 106
5.18 BER vs. PMD parameter after 5 spans (400 km) with optical equalizer (64-QAM). 107
6.1 Block diagram of a typical MCF system, Amp. = amplifier. 111
6.2 Block diagram of multi-core/fiber WDM system, MZM = Mach-Zehnder modulator, IL = interleaver, Amp. = amplifier. 113
6.3 Input spectrum for single-core fiber system (left figure) and 2-core/fiber system (right figure). 113

6.4 Input spectrum for 4-core/fiber system. 113
6.5 Constellation diagram for channel 6 after 39 spans (3120 km) for (a) single-core fiber system and input power of −5 dBm per channel, (b) single-core fiber system and input power of −2 dBm per channel, (c) 2-core/fiber system and input power of −2 dBm per channel, and (d) 4-core/fiber system and input power of −2 dBm per channel. 116
6.6 Average BER vs. launch power per channel for a single-core fiber system for different number of spans, N = number of spans. 117
6.7 Average BER vs. launch power per channel for a 2-core/fiber system for different number of spans, N = number of spans. 118
6.8 Average BER vs. launch power per channel for a 4-core/fiber system for different number of spans, N = number of spans. 119
6.9 BER_{min} vs. transmission distance for single-core, 2-core/fiber, and 4-core/fiber systems. 119
6.10 A cross section of (a) 2-core fiber, and (b) 4-core fiber. 120
6.11 Non-frequency selective multiplexer block diagram. 122
6.12 Average BER vs. crosstalk factor for (a) 1-core and 2-core fiber, No. of spans = 37, $P_{in} = -6$ dBm for the 1-core, $P_{in} = -4$ dBm for 2-core, (b) 1-core and 4-core fiber, No. of spans = 47, $P_{in} = -6$ dBm for the 1-core, $P_{in} = -2$ dBm for 4-core. 122
6.13 Frequency selective multiplexer block diagram. 123
6.14 Average BER vs. crosstalk factor for (1) 2-core fiber, No. of spans = 37, $P_{in} = -4$ dBm, (2) 4-core fiber, No. of spans = 47, $P_{in} = -2$ dBm. 124

Chapter 1

Introduction

1.1 Evolution of fiber-optic communication system

Optical fiber communication is now an established technology. Several thousand route kilometers of fiber-optic systems are in use throughout the world and the market is still growing rapidly nowadays. Fiber-optic systems owe the popularity to its many advantages such as high bandwidth, low loss, and no electromagnetic interference [1]. While the demand for bandwidth increases exponentially at about 60% per year [2], the relative research and technology in fiber-optic system have become more important. In fiber-optic systems, information is transmitted by sending electromagnetic pulses through fiber. Since the carrier frequency is relatively high (around 100 THz) in the fiber-optic system, the available bandwidth is large (around 10 THz). Due to its high bandwidth and low loss (around 0.2 dB/km), it has replaced the copper cables in the long-haul data transmission.

First, the invention of laser in 1960s provided a suitable optical source [3]. At that time, large fiber loss was the main issue of optical fiber communication. The loss

problem is solved in 1979 by the invention of low loss fibers (0.2 db/km) [4]. Since then, fiber-optic communication progressed through several distinct generations. Fig. 1.1 shows the increase in the bit rate-distance product (BL) over different generations [1].

The first generation operated near 0.8 μm and became commercially available in 1980 [1]. The bit rate was 45 Mb/s and repeater spacing was up to 10 km. The second generation became available in 1980s. 1.3 μm wavelength was used due to less fiber loss near that wavelength ($<$ 1 dB/km). In this generation, the major limitation of the system came from pulse broadening caused by inter-modal dispersion which led to inter-symbol interference (ISI). To reduce the dispersion effect, single-mode fiber (SMF) was introduced. Comparing to multi-mode fiber (MMF), SMF is designed to support only one mode. Therefore, it does not suffer from pulse broadening caused by different propagation speeds of different modes (inter-modal dispersion). By 1987, a second generation reached bit rate of up to 1.7 Gb/s and repeater spacing of 50 km [1].

Loss of silica fiber becomes minimum near 1.55 μm (0.2 dB/km). Therefore, to take advantage of minimum loss, third generation operated at 1.55 μm. To minimize the dispersion, dispersion-shifted fiber (DSF) was used which has low dispersion at minimum loss wavelength. Third generation was commercially available in 1990 operating with 10 Gb/s and repeater spacing of up to 100 km [1]. Also, in this generation, coherent fiber-optic system was studied extensively [6]. At that time, coherent detection was pursued mainly because the fiber-optic systems were then loss-limited. Since coherent receivers have higher sensitivity than the direct detection receivers, coherent detection is more attractive for loss-limited systems. However, with the development

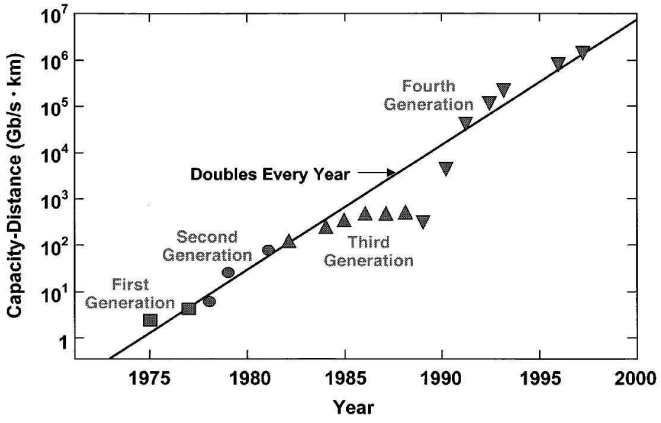

Figure 1.1: Increase in the BL product through several generations [1].

and deployment of erbium-doped fiber amplifier (EDFA) in mid 90s, fiber loss was no longer a problem and coherent receiver were abandoned due to the technical hurdles associated with aligning the phase and polarization of the local oscillator (LO) with those of the received signal.

The fourth generation of fiber-optic system introduced optical amplifiers and wavelength division multiplexing (WDM) systems. WDM systems were developed in 1990s and increased the bit rate by allowing parallel transmission of channels in the fiber. In addition, with the advent of optical amplifiers such as EDFA, amplifier spacing increased. From Fig. 1.1, it can be seen that after 1990, slope of BL product increased significantly owing to the advent of WDM systems and optical amplifiers. EDFA and WDM technology made submarine transmission systems feasible for intercontinental communication [1]. Fig. 1.2 shows the evolution of bit rate of single channel and multi-channel (WDM) systems [7]. As can be seen, the highest bit rate achieved by single channel system is about 100 Gb/s which is much less than that of WDM systems ($>$ 10 Tb/s).

Roughly in mid 2000, due to the rapid advances in digital signal processing (DSP),

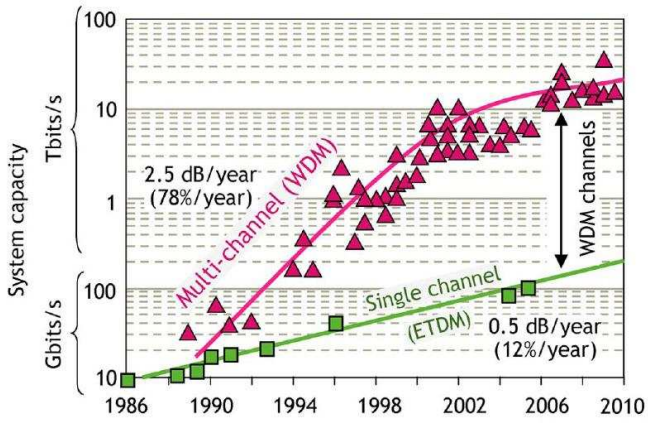

Figure 1.2: Historical evolution of record capacity in fiber-optic communication systems (multi-channel and single channel) [7].

coherent detection has drawn renewed interest [6, 8]. The polarization and phase alignment can be performed using DSP which is easier than optical phase-locked loop (PLL) used in 1990s coherent receivers. Unlike direct detection, coherent detection allows to retrieve both amplitude and phase information. The advantages of the coherent receiver are the following: (i) In the case of direct detection, the detection process is nonlinear - photo-current is proportional to the absolute square of optical field. Since the phase information is lost during detection, it is hard to compensate for dispersion and polarization mode dispersion (PMD) in electrical domain. In the case of coherent detection, the detection process is linear - the complex optical field envelope is linearly translated into electrical domain and therefore, inverse fiber transfer function can be realized using DSP to compensate for dispersion and PMD. (ii) With coherent detection, higher spectral efficiencies (SE) can be realized using advanced modulation formats that make use of both amplitude and phase modulation. High bit rate and SE was achieved by using modulation formats in which more than 1 bit can be transferred in each symbol transmission [8]. To increase the system bit rate

even more, polarization-division multiplexing (PDM) is used as well as wavelength-division multiplexing (WDM) and spectrally efficient modulation techniques such as quadrature phase shift keying (QPSK) or quadrature amplitude modulation (QAM). So far, there has been a lot of research in the areas of PDM, WDM, and modulation techniques and the maximum capacity has almost been achieved by utilizing these techniques [9]. Now, the next trend is to increase the capacity of the system by spatial-division multiplexing (SDM) through the use of multi-core fiber (MCF) systems or multi-mode fibers (MMF) [9].

1.1.1 WDM system

By the invention of wideband optical amplifiers with low noise and high gain (EDFA), the idea of parallel channel transmission was developed. The use of optical amplification in combination with WDM started a new era in the fiber-optic communications which increased system capacity dramatically (Figs. 1.1 and 1.2).

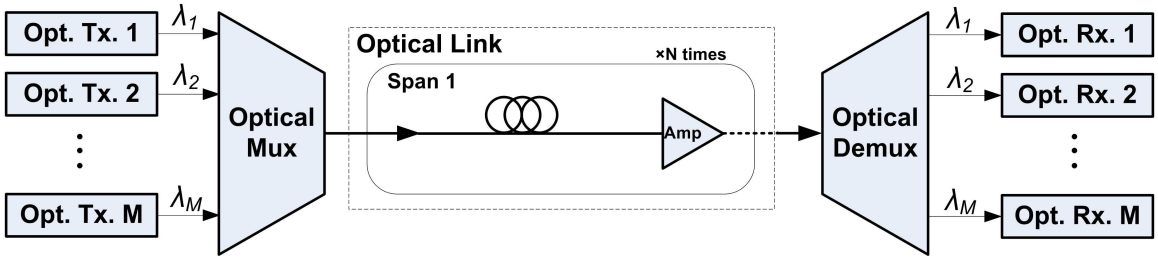

Figure 1.3: Block diagram of a WDM system.

Fig. 1.3 shows the block diagram of a WDM system. As can be seen, different optical channels with different wavelengths (λ_m) are multiplexed together with an optical multiplexer and the multiplexed channels (e.g. Fig. 1.4) is launched to an optical link. The optical link may include several spans and each span consists of an

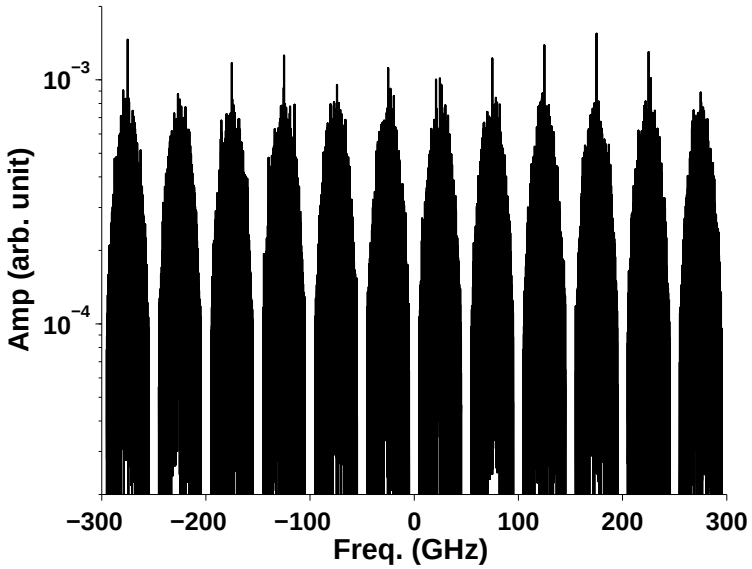

Figure 1.4: Frequency spectrum of 12 WDM channels. Each channel symbol rate = 25 Gbaud, channel spacing = 50 GHz.

optical fiber followed by an optical amplifier to compensate the corresponding fiber loss. Owing to the wideband optical amplifiers such as EDFA, all of the channels can be amplified using just one amplifier at the end of each span. At the receiver side, an optical demultiplexer separates different channels into the corresponding optical receivers. Fig. 1.4 shows the frequency spectrum of 12 WDM channels with channel symbol rate of 25 Gbaud and channel spacing of 50 GHz. The capacity can be increased by increasing number of channels. In practical implementations, the usable bandwidth is limited by the bandwidth of EDFA amplifiers. EDFA amplifiers supports signals in C-band (1525 nm - 1565 nm) and L-band (1570 nm - 1610 nm) which is on the order of 10 THz [7].

1.1.2 Multi-core fibers

Recently, there has been a significant interest in using multi-core fiber systems [9–12]. They offer spatial-division multiplexing (SDM) which is one the few remaining multiplexing techniques to increase the fiber capacity while the other techniques have almost reached the maximum capacity [9]. Fig. 1.5 shows the cross-section of a 7-core fiber. As can be seen, different cores share one cladding which leads to linear and nonlinear intraction among the cores. The amount of interaction increases as the distance between the cores decreases.

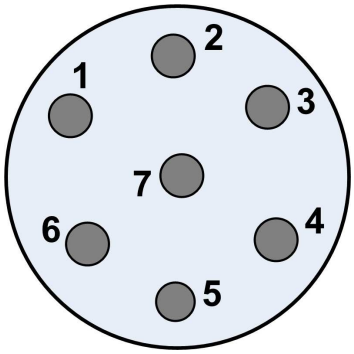

Figure 1.5: Cross-section of a 7-core fiber.

Due to importance of SDM and WDM in fiber-optic system, the second part of this thesis (Chapters 5 and 6) is dedicated to these systems. In Chapter 5, a single channel multi-core/fiber system is suggested to decrease the fiber nonlinear effect by deviding the power between different cores or fibers. In Chapter 6, a WDM multi-core/fiber system is proposed which decreases the nonlinear effect by interleaving different channels into different cores/fibers.

1.2 Impairments in fiber-optic communication systems

Generally, distortions in fiber-optic system can be classified into three categories: (1) noise, (2) linear distortions, and (3) Kerr nonlinearity [7]. These three phenomena are distributed along the fiber and influence each other. The interaction between these phenomena may lead to deterministic as well as stochastic impairments [7]. In the following, each of these distortions are explained briefly.

1.2.1 Noise

Similar to other transmission systems, optical pulses suffer from loss as they propagate through the fiber. Although the loss is low compared to other transmission systems (about 0.2 dB/km around 1550 nm wavelength), it will affect signal dramatically when the system reach is long. So, using the inline amplifiers is inevitable in fiber-optic system to recover the signal to ensure the signal-to-noise ratio (SNR) meets an acceptable limit. Amplified spontaneous emission (ASE) noise may be considered as the side-effect of using EDFA amplifiers. It is caused by spontaneous emission of photons in the amplifier and can be modeled as an additive white Gaussian noise (AWGN). For a multi-span fiber-optic link (e.g. Fig. 1.3), the noise spectral density per state of polarization is given by

$$\rho_{ASE} = (G-1)\, h f n_{\mathrm{sp}}, \tag{1.1}$$

where G is the amplifier gain, h is Planck constant, f is carrier frequency, and n_{sp} is spontaneous noise factor.

There are other sources of noise such as double Rayleigh backscatter, shot noise, and thermal noise of the receiver which can be ignored in multi-span fiber-optic system since they are much smaller than ASE noise.

1.2.2 Linear distortions

The main nonlinear distortions in fiber-optic system include group velocity distortion (GVD), and polarization mode dispersion (PMD). Since these effects are linear, they can be compensated at the receiver by linear equalizers.

Polarization mode dispersion (PMD)

Even a single-mode fiber supports two orthogonally polarized modes. In practical fiber, the random imperfections and asymmetries of the fiber cross section shape causes the optical signals in two polarizations to travel at different speeds. Fig. 1.6 shows the pulse broadening of a pulse due to the fact that different frequency components traveling at different speeds.

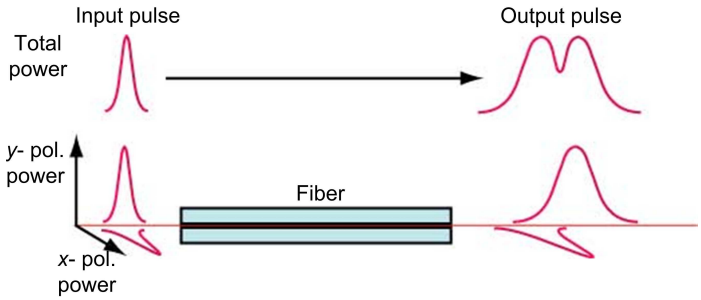

Figure 1.6: Illustration of pulse broadening effect due to PMD.

Because of the asymmetry introduced during the fiber manufacturing process and external factors such as bending or twisting, the propagation constants β_x and β_y

differ. As a result, x- and y- polarization components of the input signal arrive at the fiber output at different times leading to pulse broadening. In addition, due to random fluctuations in the fiber refractive index along the fiber axis, there is exchange of power between these polarization components that occurs randomly along the fiber. However, PMD effect can be undone by DSP [14].

Group velocity distortion (GVD)

GVD is a frequency dependence of propagation constant (β) of a single-mode fiber which causes different frequencies to propagate at different speeds. GVD is characterized by fiber dispersion coefficient (β_2) which is given by [15]

$$\beta_2 = \frac{d^2\beta}{d\omega^2}. \tag{1.2}$$

Since β_2 is a function of fiber parameters, a fiber can be designed such that it has positive β_2 (normal dispersion) or negative β_2 (anomalous dispersion). Fig. 1.7 shows the pulse broadening effect caused by GVD after 50 km. GVD pulse broadening cuases ISI which was a major limitation of early fiber-optic communication system.

Due to availability of high speed DSPs, GVD can be compensated in electrical domain by using dispersion compensating filter (DCF). Fig. 1.8 shows the block diagram of a multi-span fiber-optic system with DCF. As can be seen, fiber dispersion can be compensated in electrical domain at the DSP section. Figs. 1.9 and 1.10 show the constellation diagram and eye diagram of the received signal before and after dispersion compensation. As can be seen, before dispersion compensation, the received signal is totally unreadable (Fig. 1.9). However, after dispersion compensation, the signal is ready for the detection (Fig. 1.10).

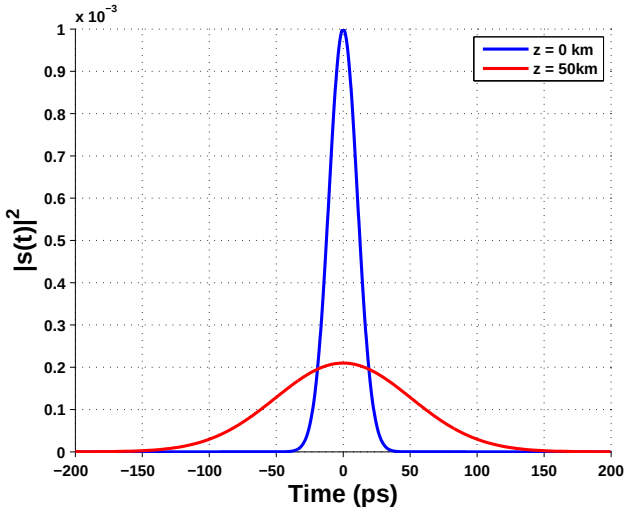

Figure 1.7: Illustration of pulse broadening effect due to GVD after 50 km.

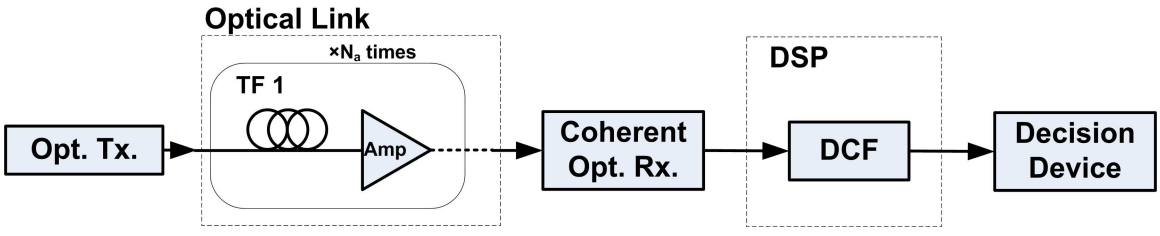

Figure 1.8: Block diagram of a multi-span fiber-optic system with DCF.

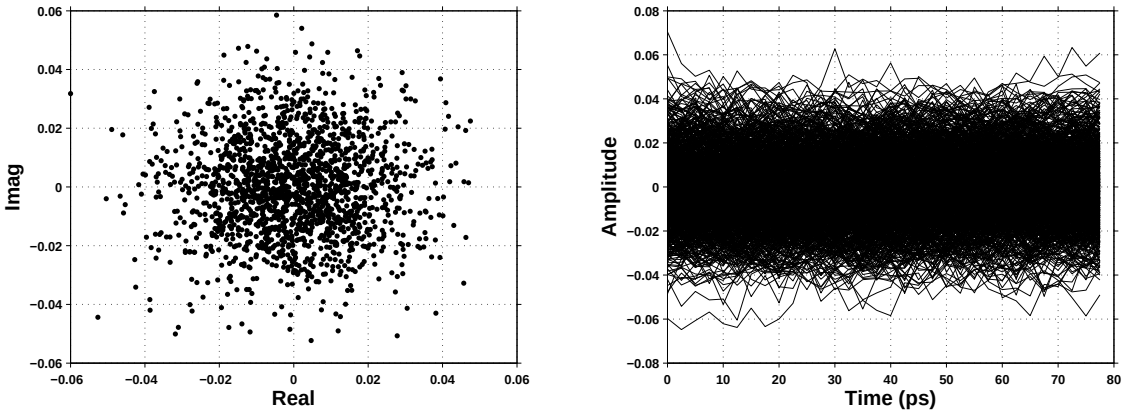

(a) (b)

Figure 1.9: Received signal (a) constellation diagram, and (b) eye diagram, before dispersion compensation. QPSK modulation, $\beta_2 = -22.1$ ps^2/km, Number of spans $N = 20$, and fiber nonlinearity was ignored.

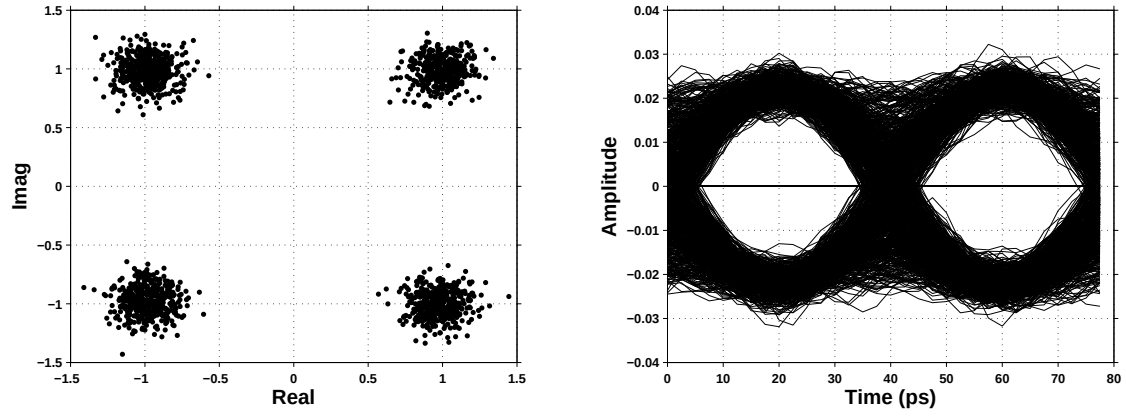

(a) (b)

Figure 1.10: Received signal (a) constellation diagram, and (b) eye diagram, after dispersion compensation. Parameters are same as Fig. 1.9

1.2.3 Kerr nonlinearity

Fiber nonlinearity originates from the intensity dependence of the fiber refractive index. In its simplest form, the refractive index can be written as [15]

$$\tilde{n}(\omega, |E|^2) = n(\omega) + n_2|E|^2, \tag{1.3}$$

where $n(\omega)$ is the linear part, $|E|^2$ is the optical intensity inside the fiber and n_2 is the nonlinear index coefficient. The impact of nonlinearity increases as the optical power increases. Thus, it enforces an upper limit to the launch power. Fig 1.11 shows a fiber-optic system typical bit error ratio (BER) as a function of launch power. As can be noticed, if the launch power is large enough (> -3 dBm in this example), the nonlinear distortion cuases system performance degredation with the increase of power.

Generally, nonlinear impairments can be divided into two categories: (1) intra-channel, and (2) inter-channel. Intrachannel impairments are the nonlinear interaction between signal and noise, and signal with itself within a channel. Inter-channel impairments are the nonlinear interaction between signals and noises from different channels. In the first part of this thesis (Chapters 2, 3 and 4), nonlinear impairments of fiber-optic system are studied and analytical models are developed for nonlinear distortion variances. Fig. 1.12 shows the different nonlinear interactions in the fiber-optic system [7]. Since the focus of this thesis is on the signal-signal nonlinear interactions, the concepts of these interactions are reviewed briefly here.

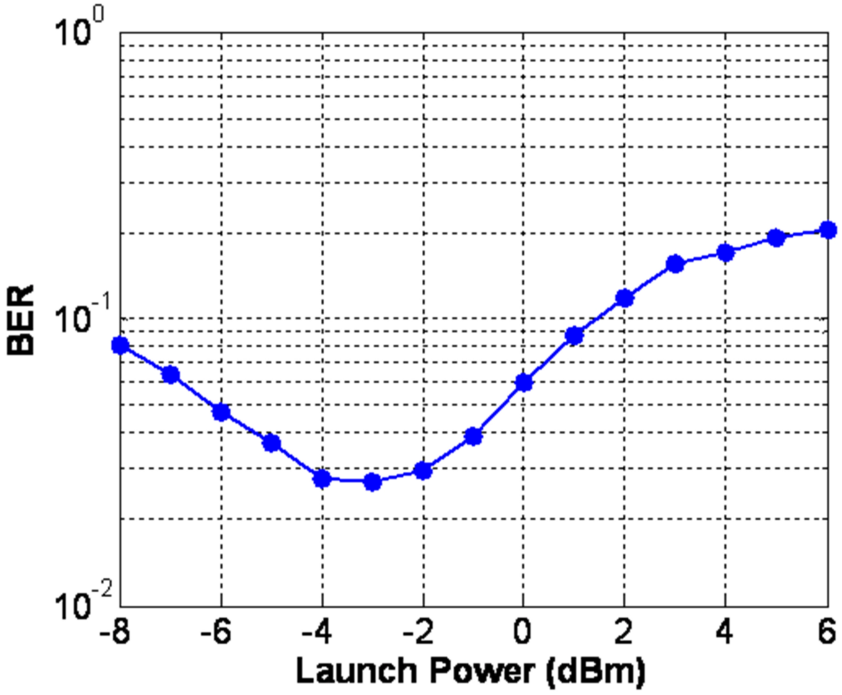

Figure 1.11: Typical BER vs. launch power curve in a fiber-optic system.

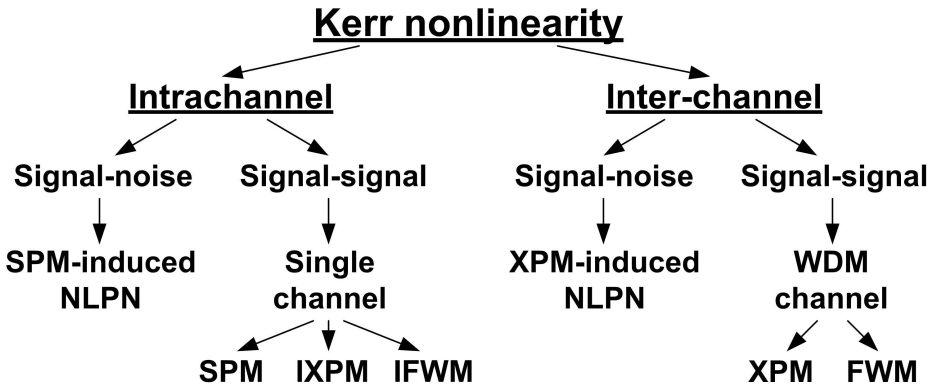

Figure 1.12: Nonlinear interactions in fiber-optic system [7]. NLPN: nonlinear phase noise, SPM: self-phase modulation, IXPM: intrachannel cross-phase modulation, IFWM: intrachannel four-wave mixing, XPM: cross-phase modulation, FWM: four-wave mixing.

Intrachannel nonlinear impairments

Intrachannel nonlinear impairment is caused by nonlinear interaction between different optical pulses within a channel. It is divided into three categories: (1) self-phase modulation (SPM), (2) intrachannel cross-phase modulation (IXPM), and (3) intrachannel four-wave mixing (IFWM). Due to the importance of intrachannel distortions in the single channel fiber-optic system performance, Chapters 2 and 3 are dedicated to analysis of intrachannel impairments for QPSK modulation and QAM modulation, respectively. In these chapters, an analytical model for the power spectral density (PSD) and variance of the nonlinear impairments for a single channel fiber-optic system is developed. The analytical PSD and varince can help to evaluate the performance of a fiber-optic system much faster than numerical methods such as Monte-Carlo simulations.

1. Self-phase modulation (SPM)

SPM refers to the self-induced phase shift experienced by an optical pulse during its propagation in optical fibers. The induced nonlinear phase shift is given by [15]

$$\phi_{NL}(z,T) = \left(\frac{L_{eff}}{L_{NL}}\right)|u(0,T)|^2, \tag{1.4}$$

$$L_{\mathrm{NL}} = \left(\gamma_0 P_0\right)^{-1}, \tag{1.5}$$

$$L_{\mathrm{eff}} = \left[1-\exp(-\alpha L)\right]/\alpha, \tag{1.6}$$

where $u(0,T)$ is the field envelope at $z=0$, γ_0 is the fiber nonlinear coefficient, P_0 is the peak power, α is the fiber loss, and L is the fiber length. Time dependence of

nonlinear phase shift induces spectral changes given by [15]

$$\delta\omega(z,T) = -\frac{\partial}{\partial T}\phi_{NL}(z,T) = -\left(\frac{L_{eff}}{L_{NL}}\right)\frac{\partial}{\partial T}|u(0,T)|^2, \tag{1.7}$$

The time dependence of $\delta\omega$ is referred as frequency chirping. Fig. 1.13 shows a Gaussian pulse at the input of the fiber (1.13(a)) and the frequency chirp caused by SPM (1.13(b)). As can be seen in Fig. 1.13(b), $\delta\omega$ is negative near the leading edge (red shift) and becomes positive near the trailing edge (blue shift).

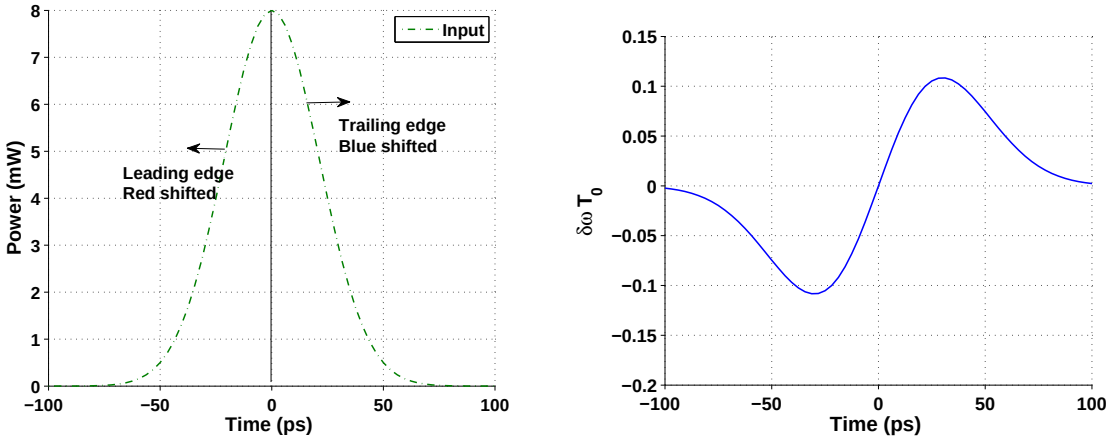

(a) (b)

Figure 1.13: (a) A Gaussian pulse in time domain, and (b) frequency chirp $\delta\omega$ caused by fiber nonlinearity for Gaussian pulse.

Fig. 1.14 shows the input pulse (input), output in linear regime (Lin: $\gamma_0 = 0$ $W^{-1}km^{-1}$), and output in nonlinear regime (Lin+SPM: $\gamma_0 = 2.43$ $W^{-1}km^{-1}$) for normal dispersion and anomalous dispersion. Since higher frequencies travel slower in the normal dispersion case, the trailing edge of the pulse (blue shift) travels slower than the leading edge (red shift). So, the pulse experiences more pulse broadening compared to the case when nonlinearity is not present (Fig. 1.14(a)). On the other

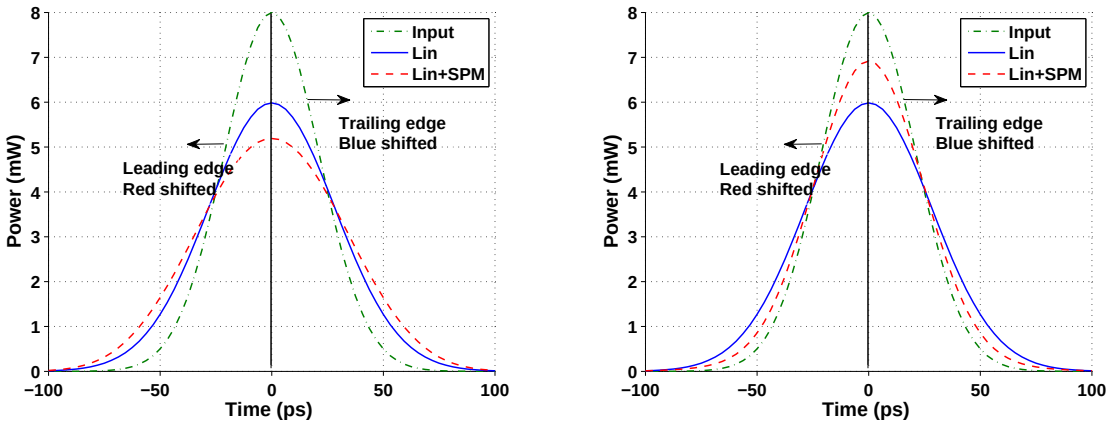

Figure 1.14: Input pulse (input), output in linear regime (Lin: $\gamma_0 = 0$ W^{-1}km^{-1}), and output in nonlinear regime (Lin+SPM: $\gamma_0 = 2.43$ W^{-1}km^{-1}) for (a) normal dispersion $\beta_2 = 10$ ps^2/km, and (b) anomalous dispersion $\beta_2 = -10$ ps^2/km. Following parameters were assumed: $P_{peak} = 8$ mW, $T_{FWHM} = 50$ ps, no. of spans $= 1 \times 80$ km.

hand, in the anomalous dispersion case, higher frequencies travel faster which causes pulse compression compared to the case in which SPM is absent (Fig. 1.14(b)).

2. Intrachannel cross-phase modulation (IXPM)

IXPM is nonlinear interaction between neighboring pulses which leads to attraction or repulsion between pulses. Fig. 1.15 shows the input and output pulses for normal dispersion and anomalous dispersion. The leading edge of second pulse red shifts the trailing edge of first pulse and the trailing edge of first pulse blue shifts the leading edge of first pulse (Eq. (1.7)). Therefore, the pulses repel each other in the normal dispersion (Fig. 1.15(a)) and attract each other in the anomalous dispersion (Fig. 1.15(b)).

3. Intrachannel four-wave mixing (IFWM)

In a single channel system nonlinear interaction of 3 pulses centered at t_1, t_2, and

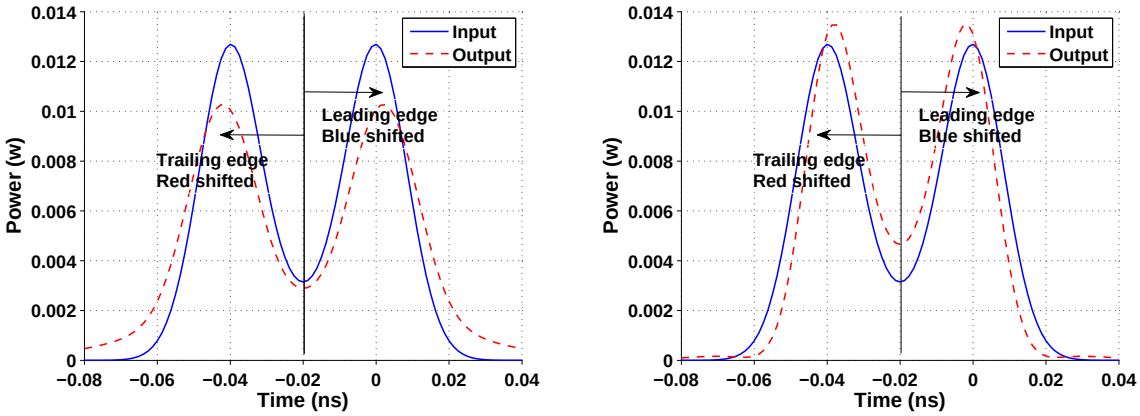

(a) (b)

Figure 1.15: Input pulses and output pulses after DCF for (a) normal dispersion $\beta_2 = 10$ ps^2/km, and (b) anomalous dispersion $\beta_2 = -10$ ps^2/km. Following parameters were assumed: $\gamma_0 = 2.43$ W^{-1}km^{-1}, $P_{peak} = 11$ dBm, $T_{FWHM} = 20$ ps, no. of spans $= 5 \times 80$ km.

t_3 of the same channel leads to echo pulses at $t_1 + t_2 - t_3$ and $t_2 + t_3 - t_1$ [16–18]. Figs. 1.16(a) and 1.16(b) show the three pulses at the input and output of the fiber-optic system after DCF in linear scale and logarithmic scale, respectively. As can be seen in Fig. 1.16(b), nonlinear interaction of the three pulses generated 1st order echo pulses and nonlinear interaction between the 1st order echo pulses and the main pulses generates 2nd order echo pulses. Typically, magnitude of the 2nd order echo pulse is sufficiently small compared to that of 1st order echo pulse such that they can be neglected. If there is a signal pulse at the location of echo pulses, the echo pulses would act as a noise leading to performance degradations.

Inter-channel nonlinear impairments

Due to intensity dependence of the fiber refractive index, self-phase modulation occurs for an optical pulse propagating in a fiber-optic system. Since the refractive index seen

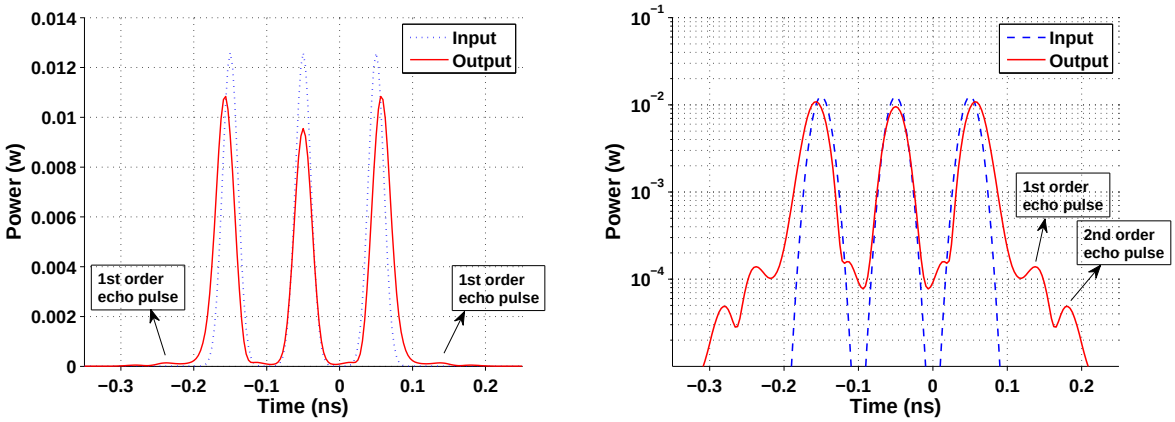

(a) (b)

Figure 1.16: Input pulses and output pulses after DCF in (a) linear scale , and (b) logarithmic scale. Following parameters were assumed: $\beta_2 = 10$ ps^2/km, $\gamma_0 = 2.43$ W^{-1}km^{-1}, $P_{peak} = 11$ dBm, $T_{FWHM} = 25$ ps, no. of spans $= 8 \times 80$ km.

by an optical pulse depends on the other propagating pulses as well as the pulse itself, coupling between the pulses happen in the WDM fiber-optics system. When two or more optical pulses with different frequencies propagate in the fiber simultaneously, they interact with each other due to the fiber nonlinearity. Inter-channel can be divided into two categories: (1) Cross-phase modulation (XPM), and (2) Four-wave mixing (FWM). Due to the impact of XPM on the performance of WDM systems, analysis of XPM impairments is presented in Chapter 4. In this chapter, an analytical model is developed for the inter-channel nonlinear impairments variance.

1. Cross-phase modulation (XPM)

Due to Kerr nonlinear effect, two propagating pulses with different wavelengths can induce nonlinear phase on each other. The instantaneous frequency change across the first pulse due to XPM nonlinear phase induced by the second pulse is given by [15]

$$\delta\omega_1(z,T) = -\gamma_0 \frac{\partial}{\partial T}|u_2(z,T)|^2, \tag{1.8}$$

where $u_2(0,T)$ is the field envelope in the second channel.

Fig. 1.17 shows two WDM channels inputs. We have launched a single pulse at symbol slot 0 in each channel, and initially the pulses are aligned. Fig. 1.18 shows the spectrum of WDM channels. We assume anomalous dispersion ($\beta_2 = -10$ ps^2/km < 0) and center wavelength of channel 2 to be lower than that of channel 1 (Fig. 1.18), so channel 2 propagates slower than channel 1. Our reference frame is fixed to channel 1 and the pulse in channel 2 moves with the inverse walk-off speed of $v_{walk}^{-1} = \beta_2\Omega$ relative to channel 1, where Ω is the channel spacing. Fig. 1.19 shows the channels at the end of a $L = 80$ km span. As can be seen, due to different channel speeds, channel 1 walked off channel 2. The pulses separation at the end of the span is given by

$$\Delta T = v_{walk}^{-1} L \cong 250\ ps \tag{1.9}$$

Fig. 1.20 shows the pulse shape of channel 1 at the end of the fiber for three different cases: (1) Linear case (Lin): $\gamma_0 = 0$ W^{-1}km^{-1} which shows the linear response of the fiber-optics system, (2) SPM case (Lin+SPM): no pulse presents in channel 2, and (3) XPM case (Lin+SPM+XPM): both channels are present. Since anomalous dispersion was assumed, in the presence of nonlinearity (Lin+SPM), the output pulse width is narrower compared to the linear case (Lin). From Fig. 1.20, it can also be seen that when both channel are present (Lin+SPM+XPM), the center of pulse has moved to the right. As the fast channel (channel 1) walks off, it induces the phase modulation on the slower channel (channel 2), and vice versa. In Fig. 1.17, the pulses are initially aligned and during the propagation, the leading edge of slow channel overlaps with the trailing edge of fast channel. The slope is positive at the

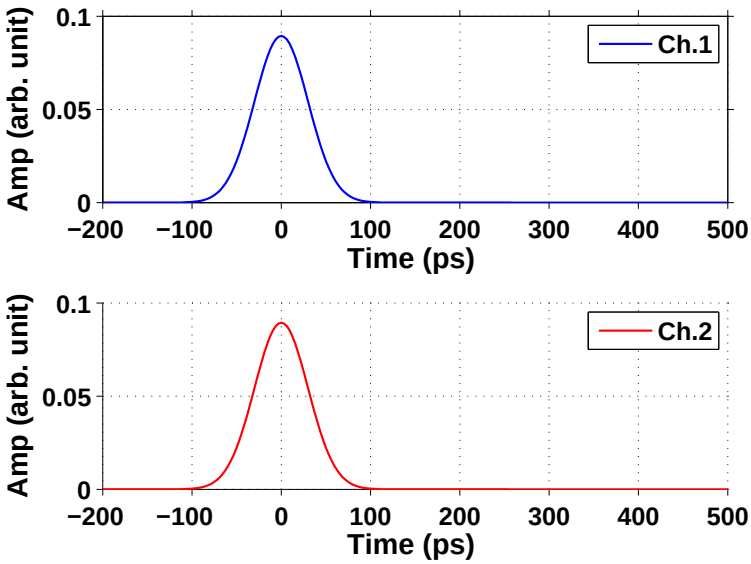

Figure 1.17: Input pulses for channels 1 and 2. The following parameters were assumed: $P_{peak} = 8$ mW, $T_{FWHM} = 50$ ps, channel spacing = 50 GHz, $\beta_2 = -10$ ps^2/km, $\gamma_0 = 2.43$ W^{-1}km^{-1}, fiber loss = 0.2 dB/km, and span length 80 km

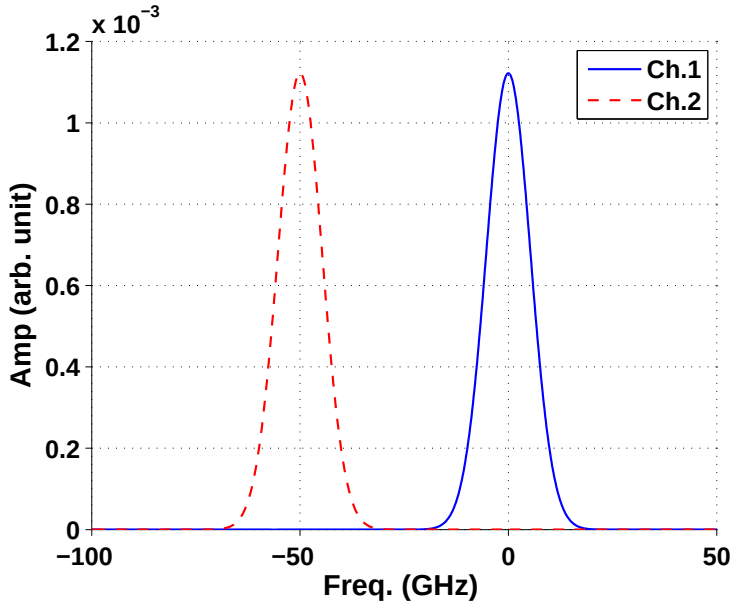

Figure 1.18: Frequency spectrum of channels 1 and 2 at the input. Parameters are same as that of Fig. 1.17

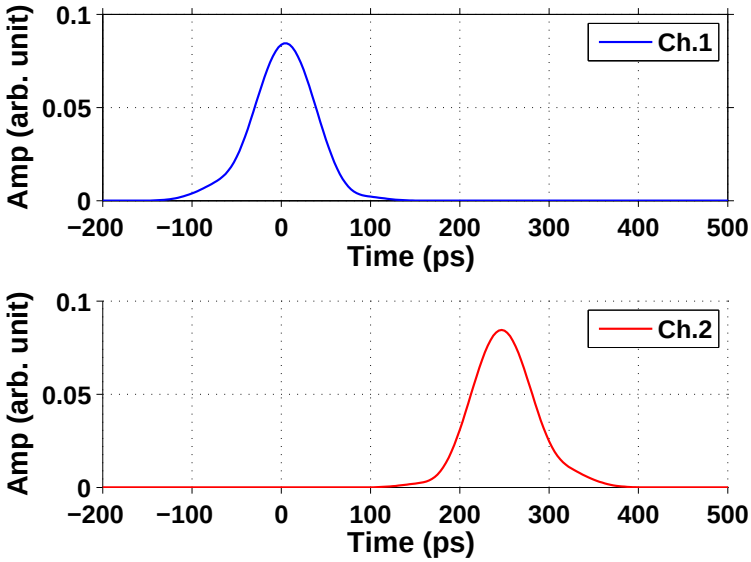

Figure 1.19: Output pulses for channels 1 and 2. Parameters are same as that of Fig. 1.17

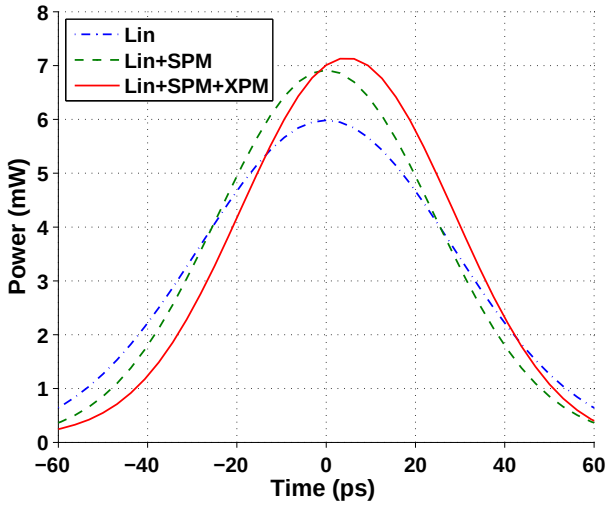

Figure 1.20: Channel 1 output pulse when (1) Lin: $\gamma_0 = 0$ $W^{-1}km^{-1}$, (2) Lin+SPM: no pulse presents in channel 2, and (3) Lin+SPM+XPM: both channels are present. Parameters are same as that of Fig. 1.17

leading edge of channel 2 and therefore, from Eq.(1.8), the instantaneous frequency is negative or in other words channel 1 is red shifted [15]. Since red shifted components travel slowly in anomalous dispersion fiber, the pulse of channel 1 arrives late or in other words, there is a timing shift due to XPM (Fig. 1.20) [19].

2. Four-wave mixing (FWM)

Similar to IFWM, nonlinear interaction among three WDM channels in frequencies f_1, f_2, and f_3 leads to FWM sidebands at $f_1 + f_2 - f_3$ and $f_2 + f_3 - f_1$ (Fig. 1.21). If there is another channel at the location of FWM sidebands, the FWM sidebands would act as a noise leading to performance degradations.

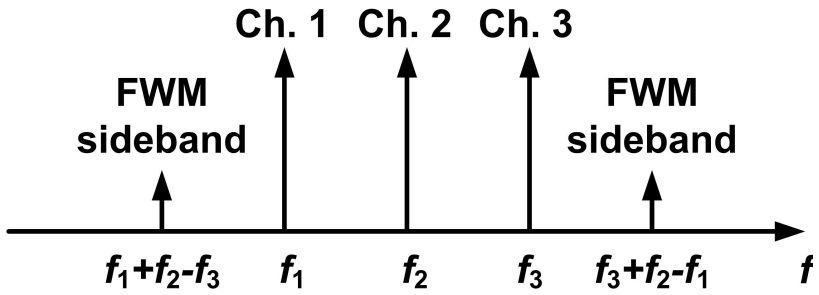

Figure 1.21: Three WDM channels and generated FWM sidebands.

1.3 Thesis layout

This thesis is organized into two parts. In the first part (Chapters 2, 3, and 4), an analysis of the nonlinear impairments is presented for the single channel as well as for multi-channel scenarios. In this part, analytical models are developed for intrachannel nonlinear impairments as well as inter-channel nonlinear impairments. In the second part (Chapters 5 and 6), a multi-core/fiber architecture is proposed to mitigate the nonlinear distortions of the fiber-optic system for single channel and multi-channel

scenarios.

In Chapter 2, a first order perturbation theory is used to develop analytical expressions for the power spectral density (PSD) of the nonlinear distortions due to intra-channel four-wave mixing (IFWM). For the Gaussian pulse shape, PSD is obtained analytically for a system based on quadrature phase-shift keying (QPSK). For non-Gaussian pulses, the PSD can not be calculated analytically. However, using the stationary phase approximations, we found that convolutions become simple multiplications and a simple analytical expression for the PSD of the nonlinear distortion is found. To validate the analytical expression, raised-cosine pulse shape is used. The PSD of the nonlinear distortion is combined with the amplified spontaneous emission (ASE) PSD to obtain the total variance and bit error ratio (BER) for a QPSK system. The analytically estimated BER is found to be in good agreement with numerical simulations.

In Chapter 3, analytical expressions for the PSDs and variances of intrachannel nonlinear impairments are obtained for a fiber-optic system based on quadrature amplitude modulation (QAM). Similar to Chapter 2, a first order perturbation theory is used to develop analytical expressions. For a constant intensity modulation such as QPSK, it can be shown that SPM and IXPM produce only a deterministic phase shift, and they do not contribute to the noise variance. However, for genaral QAM signal, IXPM is stochastic and leads to the performance degredation. In this chapter, the PSDs for SPM, IFWM, IXPM, and correlation between them are calculated analyticaly for QAM system. The numerical and analytical variances are plotted versus the launch power and dispersion parameter and effect of each parameter on the noise variance has been investigated. The total analytical variance is found to be in good

agreement with simulations.

In Chapter 4, a first order perturbation technique for the study of self-phase modulation (SPM) and cross-phase modulation (XPM) effects in WDM fiber-optics system is developed. The analytical model for the SPM and XPM distortions is developed based on QAM. Then, the variance of the noise due to the XPM distortion is obtained analytically. The variance of the XPM distortion is plotted versus input launch power, dispersion parameter, number of spans, and channel spacing. It is shown that the variance of XPM distortion increases almost linearly with the number of spans. The quick and rough estimate of the XPM penalty can be done by using the slope of the curve after one or two spans and it can be extrapolated for a fiber-optic system with larger number of spans. Simulation results show good agreement between numerical an analytical results.

In Chapter 5, a multi-core/fiber architecture is proposed to mitigate the nonlinear impairments in fiber-optic systems. The power launched to each core/fiber is reduced in multi-core/fiber architecture as compared to the case of single fiber leading to reduction in nonlinear impairments. In this system, a power splitter divides the input power between different cores/fibers so each core/fiber receives less power. At the end of each fiber span, a power combiner combines the cores/fibers outputs and passes it through just one amplifier. So, this technique does not increase the number of amplifiers. The optical pulses propagating in the fibers undergo different amount of phase shifts and timing delays due to the fluctuations of fibers' propagation constants and fibers' inverse group speeds. Optical and electrical equalization techniques are proposed to compensate for these channel effects. In the case of an optical equalizer, adaptive time shifters and phase shifters are adjusted such that the maximum power

is obtained at the output of power combiner. Our numerical simulation results show that for unrepeatered systems, the performance (Q factor) is improved by 6.2 dB using 8-core/fiber configuration as compared to single-core fiber system. In addition, for multi-span system, the transmission reach at a bit error ratio (BER) of 2.1×10^{-3} is quadrupled in 8-core/fiber configuration.

In Chapter 6, a multi-core or multi-fiber architecture with interleaver at the fiber input and wavelength division multiplexing (WDM) demultiplexer at the fiber output is proposed. In this architecture, different channels of a WDM system are interleaved into different cores/fibers and therefore, the inter-channel nonlinear impairments is suppressed. Unlike the single-channel multi-core/fiber system, WDM multi-core/fiber system does not need adaptive phase shifters and time shifters since different cores/fibers carry channels with different frequencies. It is shown that for a 39-span system, the 4-core/fiber system with negligible crosstalk outperforms the single-core system by 2.2 dBQ_{20}. The impact of crosstalk between cores of a multi-core fiber (MCF) on the system performance is studied. The simulation results show that the performance of the multi-core WDM system is less sensitive to the crosstalk effect compared to conventional multi-core systems since the propagating channels in the cores are not correlated in frequency domain.

In Chapter 7, conclusions of the present work and future plans are given.

1.4 Publications list

The research work has resulted in the following publications in each part:

Multi-core/fiber system

1. S. Naderi Shahi, and Shiva Kumar, "Reduction of nonlinear impairments in fiber

transmission system using fiber and/or transmitter diversity," *Optics Communications* **285**, p. 3553 (2012).

2. S. Naderi Shahi, and S. Kumar, "Reduction of Nonlinear Impairments in Fiber Transmission System Using Fiber Diversity," *Signal Processing in Photonics Communications* (SPPCom) Toronto, Canada, June 2011.

Multi-core/fiber WDM system

3. Sina Naderi Shahi, and Shiva Kumar "A multi-core WDM system with wavelength interleaving among cores," *Photonics North Conference*, Ottawa, Canada, June 2013.

4. Sina Naderi Shahi, and Shiva Kumar "A multi-core or multi-fiber WDM system," *Optics Communications* **294**, p. 289 (2013).

5. Sina Naderi Shahi, and Shiva Kumar "A multi-core or multi-fiber WDM System," *International Conference on Optical Engineering* (ICOE), Belgaum, India, July 2012.

Nonlinear impairments analysis

6. Shiva Kumar, Sina Naderi Shahi, and Jing Shao, "Analysis and Compensation of Nonlinear Impairments in Fiber Optic systems," Invited talk, *International Conference on Optical Engineering*, Belgaum, India, July 2012.

7. Shiva Kumar, Sina Naderi Shahi, and Dong Yang "Analytical Modeling of a Single Channel Nonlinear Fiber Optic System Based on QPSK, *Optics Express* **20**, p. 27740 (2012).

8. S. Naderi Shahi, and Shiva Kumar, "BER Calculation of a Single Channel Nonlinear Fiber Optic Transmission System Based on QPSK," *IEEE Photonics Conference* (IPC) Burlingame, USA, September 2012.

9. S. Naderi Shahi, and Shiva Kumar, "Analytical modeling of intrachannel nonlinear

impairments in QAM fiber optic system," *Signal Processing in Photonics Communications* (SPPCom) Rio Grande, Puerto Rico, July 2013.

10. S. Naderi Shahi, and Shiva Kumar, "Analytical modeling of cross-phase modulation in coherent fiber-optic system," submitted to *Optics Express*.

Chapter 2

Analytical modeling of a single channel nonlinear fiber-optic system based on QPSK

2.1 Introduction

In a highly dispersive fiber, a signal pulse broadens significantly and thereby, it interacts nonlinearly with a large number of pulses in its neighborhood. This nonlinear interaction leads to ghost or echo pulses which is known as intrachannel four-wave mixing (IFWM) [16–18, 20–22]. The propagation impairments due to IFWM in direct detection systems are analyzed in Refs. [20, 21]. In [22], analytical expressions for the complex field envelope of the echo pulse due to IFWM is derived using a first order perturbation theory assuming that the signal pulses are Gaussian. Recently, the modeling of nonlinear distortion in coherent fiber-optic systems has drawn significant interest [23–28]. In Ref. [23], propagation impairment due to four wave mixing

(FWM) in coherent orthogonal frequency-division multiplexing (OFDM) systems is studied and symmetries are used in the conventional FWM model. In Ref. [24], an analytical expression for the probability density function (PDF) of the IFWM impairments is derived for coherent fiber-optic systems based on phase-shift keying (PSK). In Ref. [25], an analytic expression for the nonlinear threshold is found by assuming that signal pulses in each symbol slot are delta functions. In Ref. [26], an analytical expression for the power spectral density (PSD) of the nonlinear interference in a WDM system is developed. To evaluate the PSD, it is necessary to carry out a triple numerical integration and the computational cost scales as M^3 where M is the number of samples in frequency domain. In this chapter we have developed an analytical expression for the PSD of intrachannel nonlinear distortion. With analytic simplifications, we found that the computational cost scales as $\sim N^2M/8$ where N is the total number of significant neighboring signal pulses. Typically, N is smaller than M leading to significant reduction in computational time. However, the direct comparison between these two approaches is not appropriate since Ref. [26] primarily focused on inter-channel impairments whereas this chapter deals with intrachannel impairments only. In Ref. [27], a general first order perturbation theory of a multichannel optical transmission system is developed and stationary phase approximation is done to evaluate the cross-phase modulation fluctuations. In Ref. [28], it is proposed to apply a large predispersion to an optical signal before fiber transmission and a stationary phase approximation is employed to approximate the solution of nonlinear Schrodinger equation (NLSE) in the limit of very strong initial predispersion. In this chapter, the stationary phase approach is used to approximate the Fourier transform of the echo pulse in a single channel so that the computational

cost of the PSD calculations can be reduced. The stationary phase approximation translates convolutions into simple multiplications leading to a simple closed form expression for the spectrum of the echo pulse. As a result, the spectrum of the echo pulse is found to be proportional to the product of the signal pulse spectra shifted by the amounts proportional to the temporal positions of the signal pulses. Finally, the PSD of the nonlinear distortion is added to the PSD of the amplified spontaneous emission (ASE) and the integration of the PSD over the receiver bandwidth leads to the total variance which is used to calculate the bit error ratio (BER). In this chapter, we consider only the case of single polarization. It is straightforward to extend the approach for the case of two polarizations.

This chapter is organized as follows. Analytical expressions for the PSD of the nonlinear distortions are derived in Section 2.2. The stationary phase approximation to calculate the spectrum of the echo pulse due to IFWM is also discussed in Section 2.2. In Section 2.3, the analytical expressions for the variance of the nonlinear distortion and BER are validated using numerical simulations. Finally, in Section 2.4, the contributions of this chapter are summarized.

2.2 Mathematical derivation of power spectral density

Let the fiber input be

$$u(t,0) = \sqrt{P} \sum_{n=-N/2}^{N/2} a_n p(t - nT_s, 0), \tag{2.1}$$

where T_s is the symbol interval, $p(t,0)$ is the pulse shape function at $z=0$, and

$$a_n = \frac{x_n + iy_n}{\sqrt{2}}, \tag{2.2}$$

x_n and y_n are real random variables that take values ± 1 with equal probability, respectively. The pulse propagation in optical fiber is described by the nonlinear Schrodinger equation (NLSE),

$$j\frac{\partial q}{\partial z} - \frac{\beta_2(z)}{2}\frac{\partial^2 q}{\partial T^2} + \gamma|q|^2 q = -j\frac{\alpha(z)}{2}q, \tag{2.3}$$

where q is the electric field envelope, $\beta_2(z)$ is the dispersion profile, γ is the nonlinear coefficient and $\alpha(z)$ is the fiber loss/gain profile. Using the transformation,

$$q(z,T) = \exp[-w(z)/2]u(z,T), \tag{2.4}$$

where $w(z) = \int_0^z \alpha(s)ds$, Eq.(2.3) can be rewritten in the lossless form as [24]

$$i\frac{\partial u}{\partial z} - \frac{\beta_2}{2}\frac{\partial^2 u}{\partial t^2} + \gamma a^2(z)|u|^2 u = 0, \tag{2.5}$$

where $a^2(z) = \exp(-w(z))$ between amplifiers. Using the perturbation technique [29], the field envelope can be expanded as

$$u = u_0 + \gamma u_1(t,z) + \cdots . \tag{2.6}$$

Here u_0 represents the 0^{th} order solution which satisfies

$$i\frac{\partial u_0}{\partial z} - \frac{\beta_2}{2}\frac{\partial^2 u_0}{\partial t^2} = 0. \tag{2.7}$$

The first order correction u_1 is

$$i\frac{\partial u_1}{\partial z} - \frac{\beta_2}{2}\frac{\partial^2 u_1}{\partial t^2} = -a^2(z)|u_0|^2 u_0. \tag{2.8}$$

Taking the Fourier transform of Eq. (2.8), we find

$$i\frac{d\tilde{u}_1}{dz} - \frac{\beta_2}{2}(2\pi f)^2\tilde{u}_1 = -a^2(z)\tilde{b}(f,z), \tag{2.9}$$

where

$$\tilde{b}(f,z) = \mathcal{F}[|u_0|^2 u_0], \tag{2.10}$$

$$\tilde{u}_1(f,z) = \mathcal{F}[u_1(t,z)], \tag{2.11}$$

$\mathcal{F}$ denotes the Fourier transform. Assuming the perfect dispersion compensation at the receiver and with $\tilde{u}_1(f,0) = 0$, Eq. (2.9) is solved to yield,

$$\tilde{u}_1(f,L_{tot}) = i\int_0^{L_{tot}} a^2(z)\tilde{b}(f,z)\exp[-i\beta_2(2\pi f)^2 z/2]dz, \tag{2.12}$$

where L_{tot} is the total transmission distance. The solution of Eq. (2.7) with the initial condition given by Eq. (2.1) is

$$u_0(t,z) = \sqrt{P}\sum_{n=-N/2}^{N/2} a_n p(t - nT_s, z), \tag{2.13}$$

where

$$p(t,z) = \mathcal{F}^{-1}[\tilde{p}(f,z)], \tag{2.14}$$

$$\tilde{p}(f,z) = \tilde{p}(f,0)\exp[i\beta_2(2\pi f)^2 z/2]. \tag{2.15}$$

From Eq. (2.10), we have

$$\begin{aligned}\tilde{b}(f,z) &= \mathcal{F}[u_0 u_0 u_0^*] \\ &= \tilde{u}_0(f,z) * \tilde{u}_0(f,z) * \tilde{u}_0^*(-f,z),\end{aligned} \tag{2.16}$$

where "$*$" denotes convolution. Using Eq. (2.13) in Eq. (2.16), we find

$$\begin{aligned}\tilde{b}(f,z) &= P^{3/2}\sum_{l=-N/2}^{N/2}\sum_{m=-N/2}^{N/2}\sum_{n=-N/2}^{N/2} a_l a_m a_n^*\{[\tilde{p}(f,z)\exp(i2\pi f l T_s)] * \\ &\quad [\tilde{p}(f,z)\exp(i2\pi f m T_s)] * [\tilde{p}^*(-f,z)\exp(i2\pi f n T_s)]\} \\ &= P^{3/2}\sum_l\sum_m\sum_n a_l a_m a_n^* \tilde{X}_{l,m,n}(f,z),\end{aligned} \tag{2.17}$$

where

$$\begin{aligned}\tilde{X}_{l,m,n}(f,z) &= [\tilde{p}(f,z)\exp(i2\pi f l T_s)] * [\tilde{p}(f,z)\exp(i2\pi f m T_s)] \\ &\quad *[\tilde{p}^*(-f,z)\exp(i2\pi f n T_s)].\end{aligned} \tag{2.18}$$

The summation in Eq. (2.17) is assumed to be from $-N/2$ to $N/2$. Substituting Eq. (2.17) into Eq. (2.12), we find

$$\tilde{u}_1(f, L_{tot}) = iP^{3/2}\sum_l\sum_m\sum_n a_l a_m a_n^* \tilde{Y}_{l,m,n}(f), \tag{2.19}$$

where

$$\tilde{Y}_{l,m,n}(f) = \int_0^{L_{tot}} a^2(z) \exp(-i\beta_2(2\pi f)^2 z/2)\tilde{X}_{l,m,n}(f,z)dz. \tag{2.20}$$

The distortion due to fiber nonlinearity is $\delta\tilde{u}_{NL} = \gamma u_1$. The PSD of the nonlinear distortion is defined as

$$\rho_{NL}(f) = \lim_{N\to\infty} \frac{1}{(N+1)T_s} E\{|\delta\tilde{u}_{NL}(f)|^2\}, \tag{2.21}$$

where $E\{\}$ denotes the ensemble average. Using Eq. (2.19), Eq. (2.21) can be written as

$$\rho_{NL}(f) = \lim_{N\to\infty} \frac{\gamma^2 P^3}{(N+1)T_s} \sum_l \sum_m \sum_n \sum_{l'} \sum_{n'} \sum_{m'} E\{a_l a_{l'}^* a_m a_{m'}^* a_n^* a_{n'}\} \tilde{Y}_{l,m,n}(f) \tilde{Y}_{l',m',n'}^*(f). \tag{2.22}$$

The PSD can be divided into two groups. They are (i) non-degenerate intrachannel four-wave mixing (ND-IFWM), and (ii) degenerate intrachannel four-wave mixing (D-IFWM). For constant intensity modulation such as QPSK, it can be shown that self-phase modulation (SPM) and intrachannel cross-phase modulation (IXPM) produce only a deterministic phase shift, which can be removed by the electrical equalizer. So, in this chapter, we ignore SPM and IXPM. The intrachannel nonlinear impairments for QAM signal is investigated in Chapter 3.

2.2.1 ND-IFWM

Let us first consider the case $l \neq m \neq n$ and $l' \neq m' \neq n'$. For QPSK signals, we have

$$E\{a_l a_{l'}^*\} = K_1 \delta_{ll'}, \tag{2.23}$$

$$E\{a_l a_{l'}\} = 0, \tag{2.24}$$

where

$$K_1 = E\{|a_l|^2\} = 1.$$

So when $l \neq m \neq n$ and $l' \neq m' \neq n'$, we have

$$E\{a_l a_{l'}^* a_m a_{m'}^* a_n^* a_{n'}\} = [\delta_{ll'}\delta_{mm'}\delta_{nn'} + \delta_{lm'}\delta_{l'm}\delta_{nn'}]. \tag{2.25}$$

δ is Kronecker delta function. Using Eqs. (2.23)-(2.25), Eq. (2.22) becomes,

$$\rho_{ND-IFWM}(f) = \lim_{N\to\infty} \frac{2\gamma^2 P^3}{(N+1)T_s} \sum_l \sum_m \sum_n |\tilde{Y}_{l,m,n}(f)|^2. \tag{2.26}$$

Equation (2.26) can be rewritten as

$$\begin{aligned}\rho_{ND-IFWM}(f) = \lim_{N\to\infty} \frac{2\gamma^2 P^3}{(N+1)T_s} \Bigg\{ & \sum_{\substack{l \\ l\neq m, l+m-n=-N/2}} \sum_m \sum_n |\tilde{Y}_{l,m,n}(f)|^2 \\ & + \sum_{\substack{l \\ l\neq m, l+m-n=-N/2+1}} \sum_m \sum_n |\tilde{Y}_{l,m,n}(f)|^2 + \ldots + \sum_{\substack{l \\ l\neq m, l+m-n=N/2}} \sum_m \sum_n |\tilde{Y}_{l,m,n}(f)|^2 \Bigg\}.\end{aligned} \tag{2.27}$$

The signal pulses located at lT_s, mT_s, and nT_s generate an echo pulse at $qT_s =$

$(l+m-n)T_s$ [16–18, 20, 21]. Therefore, q^{th} term on the right-hand side (RHS) of Eq. (2.27) represents the nonlinear distortion on the q^{th} symbol interval. Due to symmetry, the ensemble average of the nonlinear distortion should be the same on each symbol interval. In the other words, each term on the RHS of Eq. (2.27) should be equal, which yields

$$\begin{aligned}\rho_{ND-IFWM}(f) &= \frac{2\gamma^2P^3}{T_s}\sum_{\substack{l\\ l\neq m, l+m-n=0}}\sum_{m}\sum_{n}|\tilde{Y}_{l,m,n}(f)|^2 \\ &= \frac{2\gamma^2P^3}{T_s}\sum_{\substack{l\\ l\neq m}}\sum_{m}\tilde{Z}_{l,m}(f),\end{aligned} \tag{2.28}$$

where

$$\tilde{Z}_{l,m}(f) = |\tilde{Y}_{l,m,l+m}(f)|^2. \tag{2.29}$$

2.2.2 D-IFWM

Next, let us consider the case, $l = m \neq n$ and $l' = m' \neq n'$. In this case

$$E\{a_l^2(a_{l'}^*)^2a_n^*a_{n'}\} = K_1K_2\{\delta_{ll'}\delta_{nn'}\}, \tag{2.30}$$

where

$$K_2 = E\{|a_l|^4\} = 1. \tag{2.31}$$

Using Eqs. (2.30) and (2.31) in Eq. (2.22), PSD due to D-IFWM is

$$\rho_{D-IFWM} = \lim_{N\to\infty}\frac{\gamma^2P^3}{(N+1)T_s}\sum_{l}\sum_{n}|\tilde{Y}_{l,l,n}|^2. \tag{2.32}$$

Proceeding as before, we find

$$\rho_{D-IFWM} = \frac{\gamma^2 P^3}{T_s} \sum_l \tilde{Z}_{l,l}(f). \tag{2.33}$$

2.2.3 Correlation between D-IFWM and ND-IFWM

Consider the case $l = m \neq n$ and $l' \neq m' \neq n'$. Now

$$E\{a_l a_{l'}^* a_m a_{m'}^* a_n^* a_{n'}\} = E\{a_l^2 a_{l'}^* . a_{m'}^* a_n^* a_{n'}\} \tag{2.34}$$

$$= 0, \tag{2.35}$$

since

$$E\{a_l^2 a_{l'}^*\} = \begin{cases} 0, & \text{if } l \neq l' \\ E\{|a_l|^2 a_l\} = 0, & \text{if } l = l' \end{cases} \tag{2.36}$$

Therefore, from Eq. (2.22), we have $\rho_{NL}(f) = 0$. In other words, there is no correlation between D-IFWM and ND-IFWM.

2.2.4 Total PSD

Total PSD is given by

$$\rho_{NL}(f) = \rho_{ND-IFWM}(f) + \rho_{D-IFWM}(f), \tag{2.37}$$

where $\rho_{ND-IFWM}(f)$, and $\rho_{D-IFWM}(f)$ are given by Eqs. (2.28) and (2.33), respectively. For Gaussian pulses, $\tilde{X}_{l,m,n}(f)$ can be calculated as (see Appendix A)

$$\tilde{X}_{l,m,l+m} = D \exp(Af^2 + Bf + C), \tag{2.38}$$

$$A = -\frac{(\xi^2 + \delta^2)}{3\xi + i\delta}, \tag{2.39}$$

$$B = \frac{i4\pi f T_s (l+m)\xi}{3\xi + i\delta}, \tag{2.40}$$

$$C = -\frac{2\pi^2 T_s^2 \left[(l^2+m^2)\xi - lm(\xi + i\delta)\right]}{(3\xi + i\delta)(\xi - i\delta)}, \tag{2.41}$$

$$D = \frac{k^3\pi}{\sqrt{(\xi - i\delta)(3\xi + i\delta)}}, \tag{2.42}$$

$$\delta = 2\pi^2 \beta_2 z,$$

$$k = \sqrt{2\pi} T_0,$$

$$\xi = 2\pi^2 T_0^2.$$

and T_0 is $1/e$ pulse width.

2.2.5 Stationary phase approximation

For non-Gaussian pulse shapes, the convolution in Eq. (2.18) cannot be evaluated analytically. Due to the rapidly varying phase of $\tilde{p}(f, z)$ in Eq. (2.15), stationary phase approximation can be employed to approximate $\tilde{X}_{l,m,n}(f)$. Stationary phase method is a standard technique for evaluating the integrals of the form [30]

$$I = \int_{-\infty}^{\infty} G(x) e^{iy(x)} dx, \tag{2.43}$$

where $y(x)$ is a fast-varying function of x over most of the range of integration and $G(x)$ is a slowly varying function. At the rapidly varying regions of $y(x)$, the contribution to the integral is approximately zero as the area under the high frequency

sinusoids with its slowly varying envelope $G(x)$ is close to zero. The only significant contributions to the integral occurs in the regions where $dy/dx = 0$, i.e. at the points where the phase is stationary. At the vicinity of stationary phase point, x_0, $y(x)$ may be written as

$$y(x) = y(x_0) + \frac{1}{2}y''(x_0)(x - x_0)^2. \tag{2.44}$$

Using Eq. (2.44), Eq. (2.43) may be approximated as

$$I \approx G(x_0)e^{iy(x_0)} \int_{-\infty}^{\infty} e^{iy''(x_0)(x-x_0)^2/2} dx, \tag{2.45}$$

$$\approx G(x_0)e^{iy(x_0)} \sqrt{\frac{2\pi}{iy''(x_0)}} \tag{2.46}$$

Now returning to Eq. (2.18), it has double convolutions which can be analytically integrated using the stationary phase approximation when the dispersion is sufficiently large. Now Eq. (2.18) becomes (see Appendix B)

$$\tilde{X}_{l,m,l+m}(f, z) = \frac{\pi}{|\delta|}\tilde{p}\left(f - \frac{\pi l T_s}{\delta}, 0\right)\tilde{p}\left(f - \frac{\pi m T_s}{\delta}, 0\right)$$
$$\tilde{p}\left(-f + \frac{\pi(l+m)T_s}{\delta}, 0\right)\exp\left[i\left(\delta f^2 + \frac{2\pi^2 T_s^2 lm}{\delta}\right)\right]. \tag{2.47}$$

Note that the convolution in Eq. (2.18) is hard to evaluate numerically unless the pulse shape is Gaussian. But the stationary phase approximation translates the convolutions into simple multiplications as shown in Eq. (2.47), which can be easily computed. When the Nyquist pulse such as sinc pulse is used, Eq. (2.47) can be

further simplified. A sinc pulse has a rectangular spectrum,

$$\tilde{p}(f) = \begin{cases} 1, & |f| \leq B_s/2 \\ 0, & otherwise \end{cases} \tag{2.48}$$

where $B_s = 1/T_s$. Using Eq. (2.48), Eq. (2.47) can be approximated as

$$\tilde{X}_{l,m,l+m}(f,z) = \frac{\pi}{|\delta|}\tilde{p}'_{l,m}(f)\exp\left[i\left(\delta f^2 + \frac{2\pi^2 T_s^2 lm}{\delta}\right)\right], \tag{2.49}$$

where

$$\tilde{p}'_{l,m}(f) = \begin{cases} 1, & lt \leq f \leq rt \\ 0, & otherwise \end{cases} \tag{2.50}$$

$$lt = max(l, m, l+m)\frac{\pi T_s}{\delta} - \frac{B_s}{2}, \tag{2.51}$$

$$rt = min(l, m, l+m)\frac{\pi T_s}{\delta} + \frac{B_s}{2}. \tag{2.52}$$

Property 1:

$X_{l,m,l+m}$ is invariant under the exchange of l and m.

$$X_{l,m,l+m}(f) = X_{m,l,l+m}(f). \tag{2.53}$$

This property holds true in general (see Eq. (2.18)) even without the stationary phase approximation.

Property 2:

Since we have assumed that $p(t)$ is real and symmetric, it follows that $\tilde{p}(f)$ is symmetric and from Eq. (2.47), it is easy to see that there is a mirror symmetry,

$$X_{l,m,l+m}(f) = X_{-m,-l,-(l+m)}(-f). \tag{2.54}$$

2.2.6 Variance

Using the Wiener-Khinchin theorem, the variance is obtained as

$$\sigma_{NL}^2 = \int_{-\infty}^{+\infty} \rho_{NL}(f) \left|H_{rec}(f)\right|^2 df, \tag{2.55}$$

where $H_{rec}(f)$ is the receiver transfer function. Using Eq. (2.37), Eq. (2.55) may be written as

$$\sigma_{NL}^2 = \sigma_{ND-IFWM}^2 + \sigma_{D-IFWM}^2, \tag{2.56}$$

$$\sigma_r^2 = \int_{-\infty}^{+\infty} \rho_r(f) \left|H_{rec}(f)\right|^2 df, \tag{2.57}$$

where r = ND-IFWM, D-IFWM, and H_{rec} is receiver transfer function. From the property 2, it follows that,

$$\rho_r(f) = \rho_r(-f), \quad r = \text{ND-IFWM, D-IFWM.} \tag{2.58}$$

Now Eq. (2.57) may be written as

$$\sigma_r^2 = 2\int_{0}^{+\infty} \rho_r(f) \left|H_{rec}(f)\right|^2 df. \tag{2.59}$$

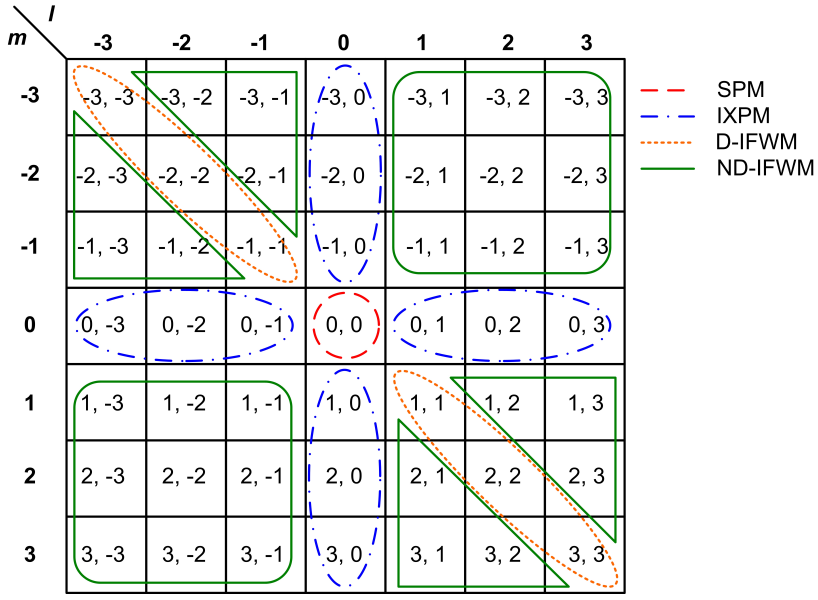

Figure 2.1: Classification of intrachannel nonlinear impairments ($N = 6$).

2.2.7 Computational cost

Figure 2.1 shows the classification of intrachannel impairments for $N = 6$ and computational cost associated with SPM, IXPM and IFWM. When Property 1 and Property 2 are not used, the computational cost per frequency calculations are as shown in Table 1.

When Property 1 is used, the computational cost per frequency for ND-IFWM is $N(N-1)/2$. If both Property 1 and Property 2 are used, the cost per frequency for ND-IFWM and D-IFWM are $N^2/4$ and $N/2$, respectively, and total computational cost per frequency (ND-IFWM + D-IFWM) is $N^2/4 + N/2$. If there are M samples in the frequency domain, total computational cost is $(N^2/4 + N/2)M$. In addition, if $|l + m| > N/2$, $|n| > N/2$, and from Eq. (2.28), it follows that the signal pulse centered at nT_s with $|n| > N/2$ does not contribute significantly for the formation of the echo pulse at $t = 0$ and hence, such a triplet may be ignored. With this

approximation, total computational cost scales as $\sim N^2M/8$ for large N. Validation of the stationary phase approximation is carried out in Section 2.3.1.

Table 2.1: Computational cost of nonlinear impairments per frequency

Nonlinear impairment	Computational cost
SPM + IXPM	2N+1
D-IFWM	N
ND-IFWM	N(N-1)
ND-IFWM + D-IFWM	N^2

2.3 Results and discussions

We carried out the numerical simulations of the fiber-optic system using the split-step Fourier method in order to test the validity of our analytical model. The multi-span system shown in Fig. 2.2 is used for simulation. N_a transmission fiber (TF) is followed by an ideal dispersion compensating fiber (DCF) which fully compensates the dispersion of the transmission fibers. The following parameters are used: fiber loss $\alpha = 0.2$ dB/km, fiber nonlinear coefficient $\gamma = 1.1$ $(\text{W.km})^{-1}$, symbol rate = 25 Gbaud, and modulation = QPSK. Gaussian pulses with full width at half maximum (FWHM) of $T_{FWHM} = 20$ psec are launched to the fiber to obtain Figs. 2.3, 2.4 and 2.7. Amplifiers spacing is 80 km. Multi-span fiber-optic system is simulated here. Laser phase noise, polarization effects, and the coherent receiver imperfections are ignored since the primary focus of this chapter is to validate our analytical model for the fiber nonlinear impairments. For numerical simulation, a pseudo-random bit sequence (PRBS) of length $2^{15} - 1$ is used for the calculation of the PSD as well as BER. A Gaussian filter with a full bandwidth of 100 GHz is used as the receiver

filter. The significant number of neighbors, $N = 20$. Equation (2.47) provides a guideline for choosing the frequency resolution. The minimum frequency shift of the pulse spectrum is $\pi T_s/\delta$. If the frequency resolution Δf is larger than $\pi T_s/\delta$, errors occur in the computation of $\tilde{X}_{l,m,l+m}(f, z)$. For a 20-span system and for $|\beta_2| = 21$ ps^2/km, $\Delta f = \pi T_s/\delta = 0.189$ GHz. With the 100 GHz bandwidth of the receiver filter, number of frequency samples, $M = 527$. Since N is much smaller than M, in this example the computational cost savings would be in order of $(527/20)^2$.

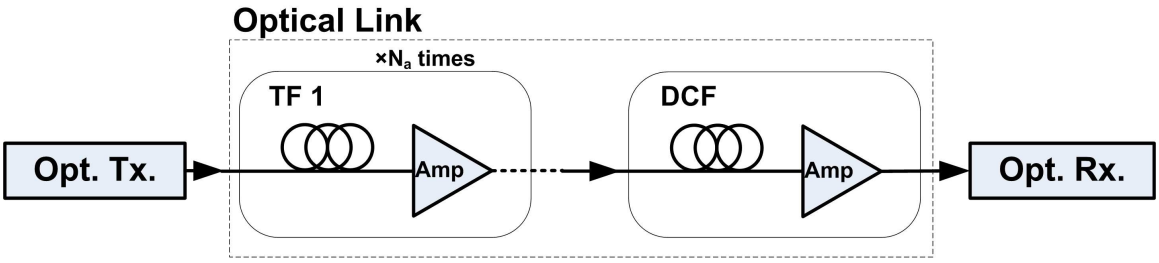

Figure 2.2: Block diagram of the system used for the simulation. TF: transmission fiber, and DCF: dispersion compensating fiber.

Figures 2.3(a) and 2.3(b) show the analytical and numerical variances as a function of the launch peak power for a 5-spans and 20-spans systems, respectively. To calculate the PSD numerically, we proceed as follows. The SPM and IXPM introduce a constant phase shift which is removed by multiplying the received signal by $\exp(i\theta)$ where θ is found adaptively. We used adaptive least mean square (LMS) equalizer to compensate the phase shift. We assumed the following parameters for the LMS algorithm: Number of filter taps = 10, number of training sequence = 2^{10}, number of samples/symbol = 2, and step size = 0.1. The numerical PSD due to the nonlinear distortion is computed by subtracting the optical field envelope at the transmitter from that at the receiver (after dispersion compensation and the phase shift removal) and then taking the Fourier transform of the difference. To account for the bit-pattern

variations, numerical simulations were performed 20 times with different bit patterns and the average PSD is computed. Over a range of powers that is of practical interest for QPSK-based system (-6 dBm to 0 dBm), the discrepancy between the analytical model and the numerical model is less than 4% and 12% in 5-span (Fig. 2.3(a)) and 20-span (Fig. 2.3(b)) systems, respectively. In addition, according to the analytical model (Eq. 2.22), the variance scales as P^3 which is in agreement with numerical results (Fig. 2.3). Later, in Chapters 5 and 6, this fact leads us to design a fiber-optic system which mitigates the nonlinearity effect by decreasing the input launch power for each fiber.

Figures 2.4(a) and 2.4(b) show the analytical and numerical variances versus the dispersion parameter for 5-spans and 20-spans systems, respectively. For a 5-span system, when the dispersion is small, there is a discrepancy between the analytical model and numerical simulations (Fig. 2.4(a)) which is due to the inaccuracy of the first order perturbation technique for the small dispersions [41]. For the 5-span system, when the dispersion is small, the variance of the nonlinear distortion is quite small. This is because the pulses do not broaden significantly, so there is no significant overlap between neighboring pulses and there is less nonlinear interaction. However, it grows quickly and beyond 7 ps/nm.km, it decays slowly. For the 20-span system, the variance decreases slowly with the transmission fiber dispersion. When the dispersion is very large, nonlinear effects are slightly reduced because of the large phase mismatch provided by dispersion which lowers the IFWM efficiency.

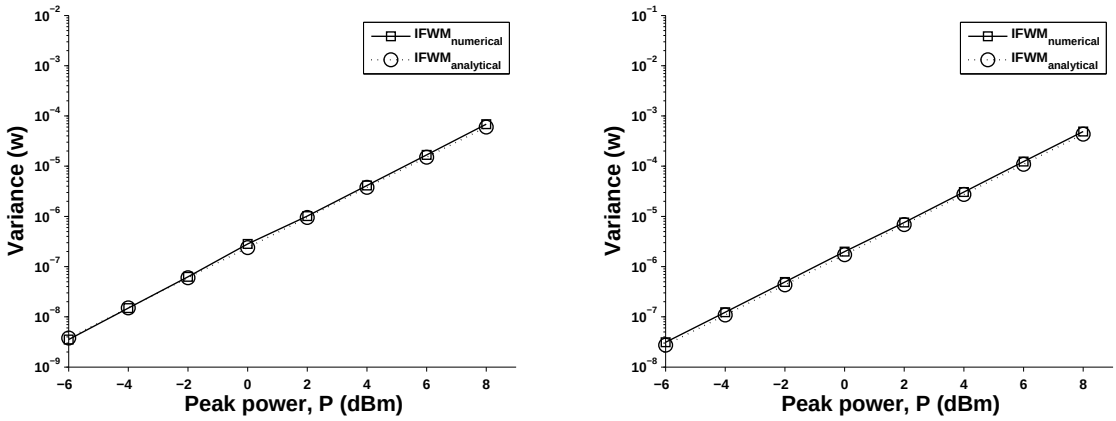

(a) (b)

Figure 2.3: Analytical and numerical variances vs. peak power for (a) 5-span, and (b) 20-span system ($\beta_2 = -21$ ps^2/km).

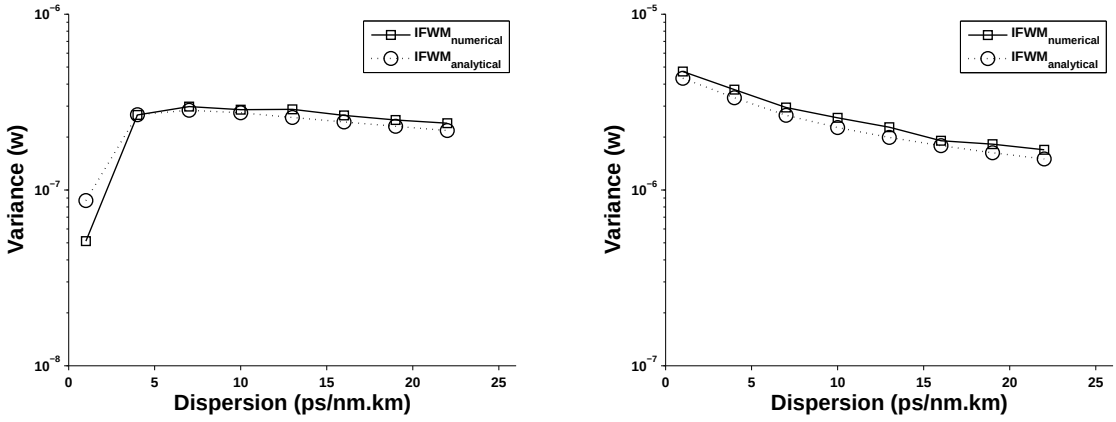

(a) (b)

Figure 2.4: Analytical and numerical variances vs. dispersion parameter for (a) 5-span, and (b) 20-span system ($P_{peak} = 0$ dBm).

2.3.1 Stationary phase approximation with raised-cosine pulse

The raised-cosine spectrum is commonly used in communication because of its compact spectrum. In this case, $\tilde{p}(f)$ is of the form [31],

$$\tilde{p}(f) = \begin{cases} 1, & |f| \leq \frac{1-a}{2T_s} \\ \frac{1}{2}\left[1 - \sin\left(\frac{\pi T_s}{a}(|f| - \frac{1}{2T_s})\right)\right], & \frac{1-a}{2T_s} < |f| \leq \frac{1+a}{2T_s} \\ 0, & |f| > \frac{1+a}{2T_s} \end{cases} \tag{2.60}$$

where a is the roll-off factor, and T_s is the symbol time interval. $\tilde{X}_{l,m,n}$ can not be calculated exactly for this pulse shape. Using the stationary phase approximation (Eq. (2.47)), total PSD and the variance is calculated. The following parameters are used for raised-cosine pulse. Roll-off factor $a = 1$ and symbol time interval $T_s = 40$ psec are assumed. Figures 2.5(a) and 2.5(b) show the variance as a function of the launch peak power for a 5-span and 20-span systems, respectively. In the range of -6 dBm to 0 dBm (that is of practical interest), the discrepancy between the analytical model and the numerical model is less than 7% in Figs. 2.5(a) and 2.5(b).

Figures 2.6(a) and 2.6(b) show the dependence of the variance on the fiber dispersion for a 5-span and 20-span systems, respectively. For a 5-span system, when the dispersion is very low, we see that the analytical model becomes inaccurate. This inaccuracy is due to two reasons: (i) first order theory becomes inaccurate for low dispersion as in the case of Fig. 2.4(a), (ii) the phase ($\propto \beta_2 f^2$) does not vary rapidly at low dispersions which makes stationary phase approximation inaccurate. However, practical fiber-optic systems use fibers with moderate to large dispersions to suppress nonlinear effects and therefore, stationary phase approximation leads to reasonably accurate results for dispersion parameter range that is of practical interest.

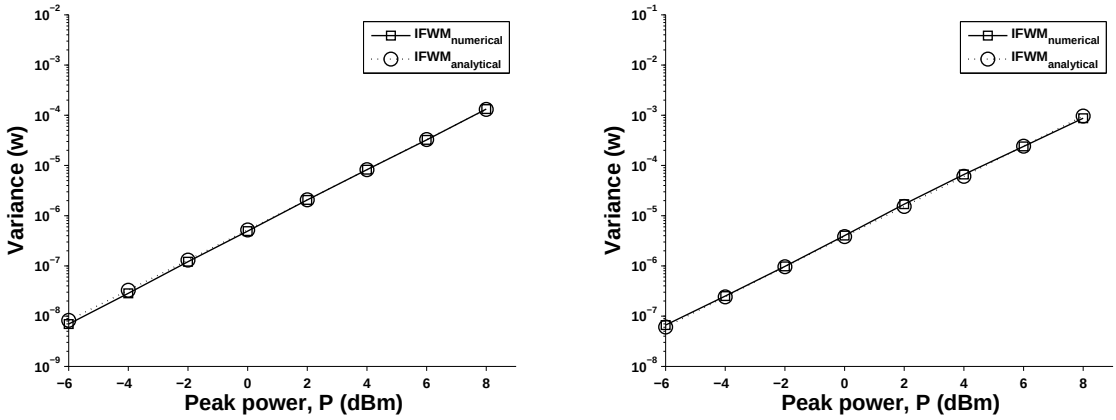

Figure 2.5: Validation of the stationary phase approximation. Analytical and numerical variances vs. launch peak power for (a) 5-span, and (b) 20-span system. Raised-cosine pulses are used. $\beta_2 = -21$ ps^2/km.

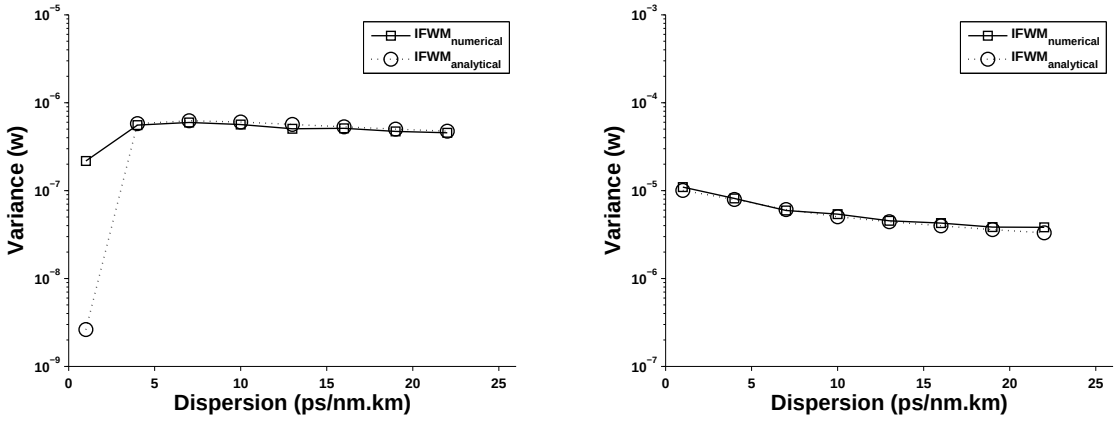

Figure 2.6: Validation of the stationary phase approximation. Analytical and numerical variances vs. dispersion parameter for (a) 5-span, and (b) 20-span system. Raised-cosine pulses are used. $P = 0$ dBm.

2.3.2 BER calculation

In this section, analytical BER is compared with numerical BER. For the analytical BER, total noise variance is calculated first and then SNR is obtained. Ignoring the interplay between the amplifier noise and nonlinearity (so called Gordon-Mollenauer noise), total PSD is given by

$$\rho_{tot}(f) = \rho_{NL}(f) + \rho_{ASE}(f), \tag{2.61}$$

where $\rho_{ASE}(f)$ is ASE noise PSD due to amplifiers,

$$\rho_{ASE} = \sum_{j=1}^{N_A} (e^{\alpha L_{a,j}} - 1) h \overline{f} n_{sp}, \tag{2.62}$$

where N_A is number of amplifiers, $L_{a,j}$ is amplifiers' spacing, α is fiber loss, h is Planck constant, $\overline{f}$ is the mean frequency of the channel, and n_{sp} is spontaneous noise factor. Using Eq. (2.61), total noise variance σ_{tot} is calculated and the probability of error P_e for QPSK is given by [31]

$$P_e = 2Q(\sqrt{2SNR}) - Q^2(\sqrt{2SNR}), \tag{2.63}$$

where Q is Q-function [31] and SNR is the signal to noise ratio,

$$SNR = \frac{P_{av}}{\sigma_{tot}^2}, \tag{2.64}$$

$$P_{av} = \frac{P}{1.88}, \tag{2.65}$$

for Gaussian pulses with 50% duty cycle, and

$$\sigma_{tot}^2 = \int \rho_{tot}(f) H_{rec}(f) df. \tag{2.66}$$

The Q-factor is defined as

$$Q(lin) = \sqrt{2}\mathrm{erfc}^{-1}(2P_e), \tag{2.67}$$

$$Q(dBQ_{20}) = 20\log_{10} Q(lin). \tag{2.68}$$

Figure 2.7 shows the analytical and numerical BER versus the launch power. We assumed the following parameters: $n_{sp} = 10$ dB, and number of spans = 20. We chose a relatively large noise figure intentionally so as to reduce the computational time of Monte Carlo simulations at large launch power. We found that the maximum discrepancy between the analytical and numerical Q-factor is less than 0.6 dBQ_{20} which is attributed to (i) non-Gaussian distribution of the IFWM pdf [24], and (ii) inaccuracy of first order perturbation technique at large launch powers. In Eq. (2.63), it is assumed that the noise is Gaussian distributed. However, in Ref. [24], it is shown that the pdf of intrachannel impairments are asymmetric and non-Gaussian. Ref. [32] has modeled the pdf of the nonlinear interference as Gaussian distribution. When the perturbation includes the Gaussian-distributed ASE and the non-Gaussian-distributed IFWM, accurate evaluation of the BER may be carried out using the Gram-Charlier technique [33], which would be the subject of a future investigation.

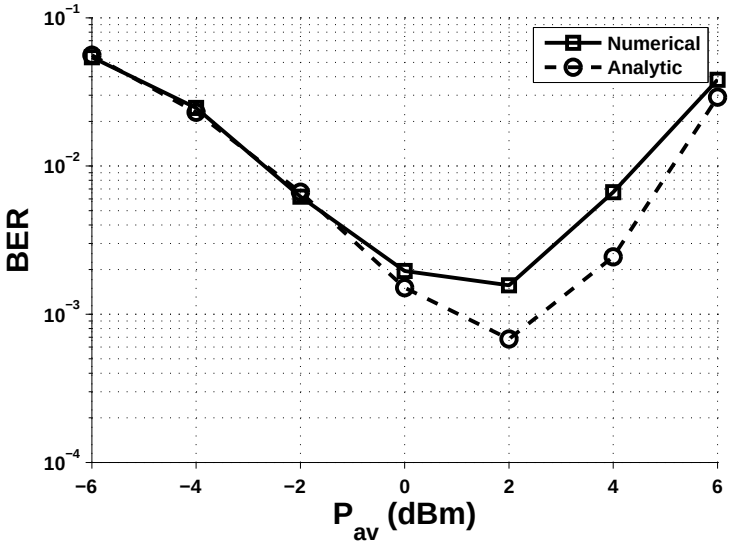

Figure 2.7: Analytical and numerical BER vs. average launch power. Gaussian pulses are used. Number of spans = 20 and $\beta_2 = -9.1$ ps^2/km.

2.4 Conclusions

We have developed analytical expressions for the PSD of the nonlinear distortions due to IFWM. Combining this PSD with that of the ASE, BER is estimated analytically which is found to be in good agreement with numerical simulations. These analytical expressions significantly reduce the computational time to estimate the BER. In addition, from the analytical model we have found that the nonlinear impairment scales as P^3 which is in good agreement with the numerical results. For non-Gaussian pulse shapes, the spectrum of the the echo pulse can not be calculated analytically. When the phase is varying rapidly as in the case of a high dispersion transmission fiber, stationary phase approximation can be employed to calculate the spectrum of the echo pulse and hence, the PSD can be calculated analytically. The stationary phase approximation translates convolutions into simple multiplications leading to a simple

analytical expression for the spectrum of the echo pulse.

Chapter 3

Analytical modeling of a single channel nonlinear fiber-optic system based on QAM

3.1 Introduction

Recently, long haul fiber-optic transmission based on quadrature amplitude modulation (QAM) has drawn significant research interest [34]. To improve the transmission performance, it is essential to understand the scaling laws of various types of nonlinear impairments. Recently, the modeling of intrachannel nonlinear distortion in coherent fiber-optic systems has drawn significant interest [24, 25, 35]. In Ref. [24], as mentioned in Chapter 2, an analytical expression for the PDF of the intrachannel four-wave mixing (IFWM) impairments is derived based on phase-shift keying (PSK). In Ref. [25], an analytic expression for the nonlinear threshold is found for delta function pulses in each symbol slot. In Ref. [35], an analytical model to calculate the

intrachannel impairments in a system based on quadrature phase shift keying (QPSK) is presented. In the case of QPSK, the amplitude and phase fluctuations caused by intrachannel cross phase modulation (IXPM) are deterministic and hence, it can be removed by linear equalizers in the digital domain. However, in the case of QAM, amplitude and phase fluctuations caused by IXPM are stochastic in nature due to multiple power levels. In this chapter, we have developed analytical expressions for the power spectral density (PSD) of intrachannel nonlinear impairments taking into account SPM, IXPM and IFWM. The analytical model provides scaling laws for various types of intrachannel nonlinear impairments and it takes significantly lower computational time than the Monte Carlo simulations to calculate the total variance.

This chapter is organized as follows. Analytical expressions for the PSD of the intrachannel nonlinear distortions for QAM signal are derived in section 3.2. Analytical expressions for different types of nonlinear interaction such as SPM, IXPM, and IFWM, are obtained in this section. In section 3.3, the analytical expressions for the variance of the nonlinear distortion are validated using numerical simulations. The effects of input lunch power and fiber dispersion on the noise variance are investigated in this chapter too. Finally, in section 3.4, the contributions of this chapter are summarized.

3.2 Mathematical expression for power spectral density

Let the fiber input be

$$u(t,0) = \sqrt{P} \sum_{n=-N/2}^{N/2} a_n p(t - nT_s, 0), \tag{3.1}$$

where T_s is the symbol interval, $p(t,0)$ is the pulse shape function at $z = 0$, and

$$a_n = \frac{x_n + iy_n}{\sqrt{2}}, \tag{3.2}$$

x_n and y_n are random variables that take values $\pm 1, \pm 3, ..., \pm(X-1)$ and $\pm 1, \pm 3, ..., \pm(Y-1)$ with equal probability, respectively. Proceeding as Section 2.2, the PSD is given by Eq. (2.22),

$$\rho_{NL}(f) = \lim_{N\to\infty} \frac{\gamma^2 P^3}{NT_s} \sum_{l} \sum_{m} \sum_{n} \sum_{l'} \sum_{n'} \sum_{m'} E\{a_l a_{l'}^* a_m a_{m'}^* a_n^* a_{n'}\} \tilde{Y}_{l,m,n}(f) \tilde{Y}_{l',m',n'}^*(f). \tag{3.3}$$

The PSD can be divided into five groups. They are (i) non-degenerate intrachannel four-wave mixing (ND-IFWM), (ii) degenerate intrachannel four-wave mixing (D-FWM), (iii) intrachannel cross-phase modulation (IXPM), (iv) self-phase modulation (SPM), and (v) IXPM and SPM correlation (SPM-IXPM). In the case of QPSK, IXPM and SPM-IXPM coupling does not lead to performance degradations and hence, it was ignored in Chapter 2. However, for QAM, we need to calculate the PSD due to the all five groups.

3.2.1 ND-IFWM

The analysis is same as Section 2.2.1. The only difference is that $K_1 = E\{|a_l|^2\} = 5$ for 16-QAM. The PSD due to ND-IFWM is given by Eq. (2.28),

$$\rho_{ND-IFWM}(f) = \frac{2\gamma^2 P^3 K_1^3}{T_s} \sum_{\substack{l \\ l\neq m, l+m-n=0}} \sum_{m} \sum_{n} |\tilde{Y}_{l,m,n}(f)|^2 \tag{3.4}$$

$$= \frac{2\gamma^2 P^3 K_1^3}{T_s} \sum_{\substack{l \\ l\neq m}} \sum_{m} \tilde{Z}_{l,m}(f), \tag{3.5}$$

where

$$\tilde{Z}_{l,m}(f) = |\tilde{Y}_{l,m,l+m}(f)|^2. \tag{3.6}$$

3.2.2 D-IFWM

Proceeding as in Section 2.2.2, we find

$$\rho_{D-IFWM} = \frac{\gamma^2 P^3 K_1 K_2}{T_s} \sum_{l} \tilde{Z}_{l,l}(f), \tag{3.7}$$

where $K_2 = E\{|a_l|^4\} = 33$ for 16-QAM.

3.2.3 IXPM

The distortion due to IXPM occurs due to the interaction of a pulse at lT_s with a pulse at mT_s with $m \neq l$. This interaction is of the form $|q_m|^2 q_l$. In other words, we have

$$l \neq m = n \quad \& \quad l' \neq m' = n'. \tag{3.8}$$

$$E\{a_l a_{l'}^* a_m a_{m'}^* a_n^* a_{n'}\} = E\{a_l a_{l'}^* |a_m|^2 |a_{n'}|^2\} = \delta_{ll'} K_1 K_{mn'}, \tag{3.9}$$

where

$$K_{mn'} = E\{|a_m|^2 |a_{n'}|^2\} = \begin{cases} E\{|a_m|^4\} = K_2 & \text{when } m = n' \\ K_1^2 & \text{when } m \neq n'. \end{cases} \tag{3.10}$$

The nonlinear distortion due to IXPM is

$$\tilde{u}_{1,IXPM}(f) = \gamma P^{3/2} \sum_l \sum_{\substack{m \\ l \neq m = n \\ m \neq l = n}} \sum_n a_l a_m a_n^* \tilde{Y}_{l,m,n}(f) \tag{3.11}$$

$$= 2\gamma P^{3/2} \sum_l \sum_{\substack{m \\ l \neq m = n}} \sum_n a_l a_m a_n^* \tilde{Y}_{l,m,n}(f). \tag{3.12}$$

Using Eqs. (3.8)-(3.11) in Eq. (3.3), the contribution to PSD due to IXPM is

$$\rho_{IXPM}(f) = \lim_{N\to\infty} \frac{4\gamma^2 P^3}{N T_s} \sum_l \sum_m \sum_{n'} K_1 K_{mn'} \tilde{Y}_{l,m,m} \tilde{Y}_{l,n',n'}^* \tag{3.13}$$

$$= \frac{4\gamma^2 P^3}{T_s} \Big\{ K_1 K_2 \sum_{\substack{m \\ m \neq 0}} |\tilde{Y}_{0,m,m}|^2 + K_1^2 \sum_{\substack{m \\ m \neq n', m \neq 0, n' \neq 0}} \sum_{n'} \tilde{Y}_{0,m,m} \tilde{Y}_{0,n',n'}^* \Big\}. \tag{3.14}$$

3.2.4 SPM

In this case, we have $l = m = n$ and $l' = m' = n'$.

$$E\{a_l a_{l'}^* a_l a_{l'}^* a_l^* a_{l'}\} = E\{|a_l|^6\} = K_3, \tag{3.15}$$

$$\rho_{SPM} = \frac{\gamma^2 P^3 K_3}{T_s} |\tilde{Y}_{0,0,0}|^2. \tag{3.16}$$

For 16-QAM, $K_3 = 245$.

3.2.5 IXPM and SPM correlation

It can be shown that the distortions due to (either of) the IFWM and IXPM (or SPM) are uncorrelated. The distortions due to ND-IFWM and D-IFWM are also uncorrelated (See section 2.2.3). However, the SPM and IXPM are correlated since both are phase-independent distortions. Considering only the SPM and IXPM, we have

$$\tilde{u}_1(f, L_{tot}) \equiv \tilde{u}_{PM}(f) = \tilde{u}_{SPM} + \tilde{u}_{IXPM}, \tag{3.17}$$

$$\tilde{u}_{SPM} = \gamma P^{3/2} \sum_{l} |a_l|^2 a_l \tilde{Y}_{l,l,l}, \tag{3.18}$$

$$\tilde{u}_{IXPM} = 2\gamma P^{3/2} \sum_{\substack{l \\ l \neq m}} \sum_{m} a_l |a_m|^2 \tilde{Y}_{l,m,m}. \tag{3.19}$$

The PSD due to SPM and IXPM is

$$\rho_{PM}(f) = \lim_{N\to\infty} \frac{E\{|u_{PM}|^2\}}{NT_s} = \rho_{SPM}(f) + \rho_{IXPM}(f) + \rho_{SPM-IXPM}(f). \tag{3.20}$$

$\rho_{SPM}(f)$ and $\rho_{IXPM}(f)$ are given by Eqs. (3.16) and (3.13), respectively. The contribution to the PSD due to the correlation between SPM and IXPM is

$$\begin{aligned}
\rho_{SPM-IXPM} &= \lim_{N\to\infty} \frac{2\gamma^2 P^3}{NT_s} \sum_{\substack{l \\ l=m=n}} \sum_{m} \sum_{n} \sum_{\substack{l' \\ l' \neq m' = n'}} \sum_{m'} \sum_{n'} E\{a_l a_l a_l^* a_{l'}^* |a_{n'}|^2\} \tilde{Y}_{l,l,l} \tilde{Y}^*_{l',n',n'} + c.c. \\
&= \lim_{N\to\infty} \frac{2\gamma^2 P^3 K_1 K_2}{NT_s} \sum_{l} \sum_{n'} \tilde{Y}_{l,l,l} \tilde{Y}^*_{l,n',n'} + c.c. \qquad (3.21) \\
&= \frac{2\gamma^2 P^3 K_1 K_2}{T_s} \sum_{\substack{n' \\ n' \neq 0}} \tilde{Y}_{0,0,0} \tilde{Y}^*_{0,n',n'} + c.c.\,, \qquad (3.22)
\end{aligned}$$

where we have used the following relation,

$$E\{|a_l|^2 a_l a_{l'}^* |a_{n'}|^2\} = \delta_{ll'} E\{|a_l|^4\} E\{|a_{n'}|^2\} = \delta_{ll'} K_2 K_1. \tag{3.23}$$

Combining Eqs. (3.13), (3.16), and (3.21), we find

$$\begin{aligned}\rho_{PM} &= \rho_{SPM} + \rho_{IXPM} + \rho_{SPM-IXPM} \\ &= \frac{\gamma^2 P^3}{T_s}\Big\{K_3|\tilde{Y}_{0,0,0}|^2 + 2K_1K_2 \sum_{\substack{n \\ n\neq 0}} (\tilde{Y}_{0,0,0}\tilde{Y}^*_{0,n,n} + c.c.) \\ &\quad + 4K_1K_2 \sum_{\substack{m \\ m\neq 0}} |\tilde{Y}_{0,m,m}|^2 + 4K_1^3 \sum_{\substack{m \\ m\neq n, m\neq 0, n\neq 0}} \sum_{n} \tilde{Y}_{0,m,m}\tilde{Y}^*_{0,n,n}\Big\}. \end{aligned} \tag{3.24}$$

3.2.6 Total PSD

Total PSD is given by

$$\rho_{NL}(f) = \rho_{ND-IFWM}(f) + \rho_{D-IFWM}(f) + \rho_{PM}(f), \tag{3.25}$$

where $\rho_{ND-IFWM}(f)$, $\rho_{D-IFWM}(f)$, and $\rho_{PM}(f)$ are given by Eq.s (3.4), (3.7), and (3.24), respectively. The total variance is given by

$$\sigma_{NL}^2 = \int_{-\infty}^{\infty} \rho_{NL}(f)\,|H_X(f)|^2\,df, \tag{3.26}$$

where $H_X(f)$ is the receiver transfer function.

3.3 Simulation results

We carried out the numerical simulation using the split-step Fourier method in order to test the validity of the analytical expressions. The fiber-optic system of Fig. 2.2 is used for simulation. The following fiber parameters were used for simulation: fiber loss $\alpha = 0.2$ dB/km, and nonlinear coefficient $\gamma = 1.1$ (W.km)$^{-1}$. For our simulation, we used 16QAM modulation with symbol rate of 25 Gbaud. Gaussian pulses with full width at half maximum (FWHM) of $T_{FWHM} = 20$ psec are launched to the fiber. A Gaussian filter with a full bandwidth of 100 GHz is used as the receiver filter. At the end of each fiber span, noiseless optical amplifiers were used to compensate the loss of fiber. Fiber length was 80 km for each span. At the receiver side, full dispersion compensation is done either in optical or electrical domain. Laser phase noise, amplifier noise, polarization effects, and receiver imperfections are ignored as in Chapter 2. To calculate the variance numerically, a pseudo-random bit sequence (PRBS) of length $2^{15} - 1$ is used.

Figure 3.1 shows the analytical and numerical nonlinear variances versus the mean peak power for a 10-span system. Numerical nonlinear variance is calculated by setting the spontaneous noise factor $n_{\rm sp} = 0$. As can be seen, the total analytical variance ($\text{total}_{\text{anl}}$) is in good agreement with numerical simulation ($\text{total}_{\text{num}}$). It can be seen that all types of intrachannel nonlinear impairments scales as P_{av}^3. The dominant nonlinear penalty comes from IXPM (ixpm_{anl} in Fig. 3.1). Since it is relatively easier to compensate for IXPM than for IFWM in digital domain, this indicates that performance improvement can be obtained by using a digital IXPM equalizer.

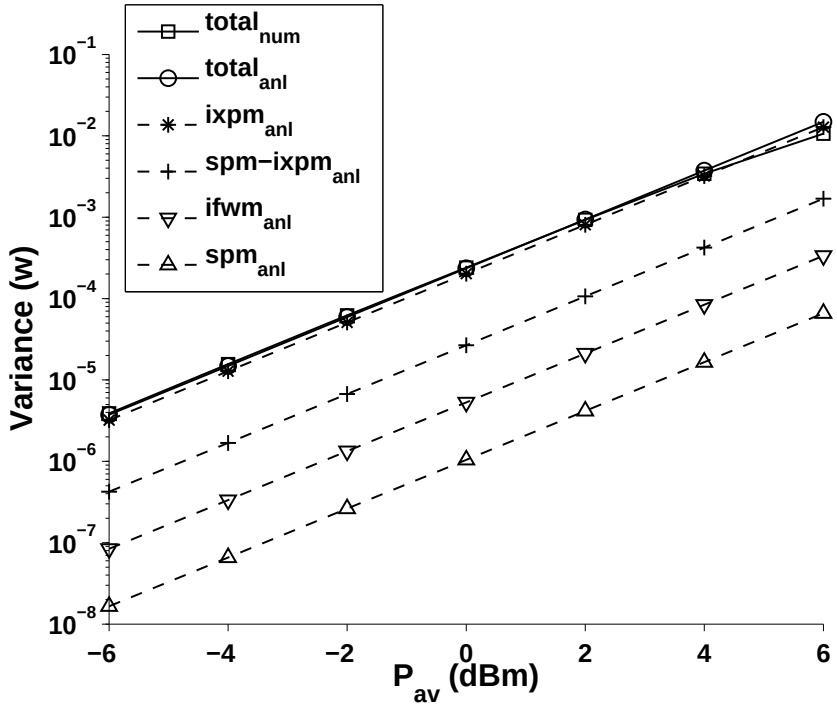

Figure 3.1: Analytical and numerical variances vs. mean launch power for a 10-span system, $D = 17$ ps/nm.km.

Fig. 3.2 shows the analytical and numerical variances versus the dispersion parameter for a 10-span system. When dispersion is too low, pulses do not broaden and therefore, IXPM and IFWM variances are quite small. In this case, main contribution to the total variance comes from SPM. As the dispersion increases, variance due to SPM decreases as the peak power reduces due to the pulse broadening, and the contributions from IXPM and IFWM increase. Total variance decreases slightly (beyond 4 ps/nm.km) as a function of increasing dispersion.

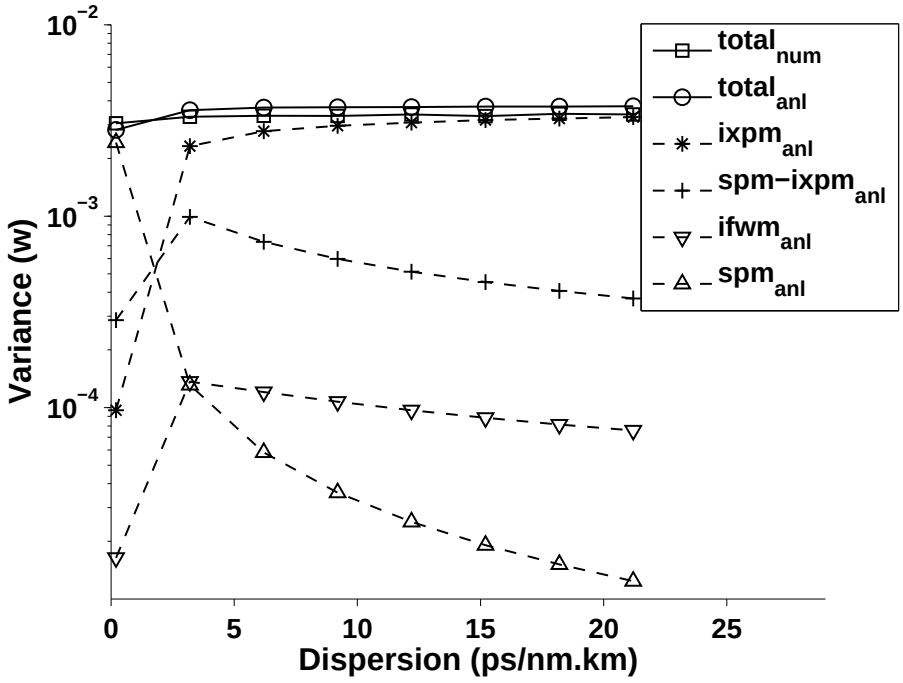

Figure 3.2: Analytical and numerical variances vs. dispersion parameter for a 10-span system, $P_{av} = 4$ dBm.

3.4 Conclusions

In conclusion, we have developed an analytical expression for the PSD due to intrachannel nonlinearity, which is found to be in good agreement with numerical simulations. The PSD is divided into 5 groups: (i) non-degenerate intrachannel four-wave mixing (ND-IFWM), (ii) degenerate intrachannel four-wave mixing (D-FWM), (iii) intrachannel cross-phase modulation (IXPM), (iv) self-phase modulation (SPM), and (v) IXPM and SPM correlation (SPM-IXPM). It is found that IXPM is the dominant impairment. Unlike the simulations, the analytical model allows to calculate the variances of SPM, IXPM and IFWM separately and hence, it may be possible to develop a digital equalizer aimed at compensating a specific type of intrachannel nonlinear impairments.

Chapter 4

Analytical modeling of XPM in WDM fiber-optic system based on QAM

4.1 Introduction

Since different WDM channels have different group speeds in dispersive fiber, symbols of a "fast" channel walk off the symbols of a "slow" channel. As the "fast" channel walks off, it induces phase distortion on the "slow" channel (XPM) and vice versa, and group velocity dispersion (GVD) converts the phase distortion into amplitude distortion [37, 38]. Each channel also experiences self-phase modulation (SPM) as it propagates through the fiber. Since SPM is a deterministic process, it does not enhance the noise in the system by itself. However, XPM effect may be considered as a stochastic process and if the symbol pattern in the other channels is unknown, it could lead to performance degradation [19].

Due to the impact of the SPM and cross-phase modulation (XPM) impairments on the performance of a wavelength-division multiplexed (WDM) systems, they have drawn considerable attention [23, 26, 27, 36–44]. In Ref. [36], XPM distortion and effect of channel spacing on XPM are investigated based on numerical simulations. In Refs. [37–39], XPM distortion in multi-span intensity-modulation direct-detection (IM-DD) is investigated in frequency domain both experimentally and theoretically. Also, the effects of bit rate and dispersion compensation are studied on the system performance. In Ref. [40], XPM and stimulated Raman scattering (SRS) distortions for a IM-DD system are studied analytically and numerically. Effect of dispersion compensation on these distortions are also investigated. In Ref. [41], second order perturbation technique is used for the study of nonlinear interaction between two single pulses in two different channels for return-to-zero (RZ) modulation.

Recently, the modeling of nonlinear distortion in coherent fiber-optic WDM systems has drawn significant interest [23, 26, 27, 42–44]. In Ref. [42], the first order Volterra series is used to estimate the channel capacity of a dispersive nonlinear optical fiber. In Ref. [43], an analytical model for XPM phase noise and polarization scattering is obtained based on Volterra analysis, and the variance and autocorrelation of the XPM phase noise and polarization scattering are calculated. In Ref. [44], an analytical expression for the PSD of inter-channel nonlinear distortion is obtained for polarization multiplexed QPSK (PM-QPSK) system in uncompensated link by assuming that the nonlinear distortion can be modeled as Gaussian periodic noise. In Ref. [23], propagation impairment due to nonlinear interaction in coherent orthogonal frequency-division multiplexing (OFDM) systems is studied. In Ref. [26], an analytical expression for the PSD of the nonlinear interference in an uncompensated

dispersion WDM system is developed. To evaluate the PSD, it is necessary to carry out a triple numerical integration. In Ref. [27], a general first order perturbation theory of a multichannel optical transmission system is developed and stationary phase approximation is done to evaluate the cross-phase modulation fluctuations. In this chapter, first order perturbation technique is used to find the nonlinear distortion due to SPM and XPM. We assume that the pulse is linear to the leading order and treat nonlinearity as a perturbation.

This chapter is organized as follows. In Section 4.2, we present a first order perturbation theory for SPM and XPM effects in fibers. Analytical expressions are obtained for the first order corrections. In Section 4.3, analytical expression for the variance of XPM impairment is obtained. In Section 4.4, the theoretical model is validated by numerical simulations. Also, effect of peak power, fiber dispersion, system reach, and channel spacing on the XPM variance is examined. Finally, in Section 4.5, the contributions of this chapter are summarized.

4.2 SPM and XPM analytical model

The pulse propagation in optical fiber is described by the nonlinear Schrodinger equation (NLS),

$$j\frac{\partial q}{\partial z} - \frac{\beta_2(z)}{2}\frac{\partial^2 q}{\partial T^2} + \gamma_0|q|^2 q = -j\frac{\alpha(z)}{2}q, \tag{4.1}$$

where q is the electric field envelope, $\beta_2(z)$ is the dispersion profile, γ_0 is nonlinear coefficient and $\alpha(z)$ is the fiber loss/gain profile. Using the transformation,

$$q(z,T) = \exp[-w(z)/2]u(z,T), \tag{4.2}$$

where $w(z) = \int_0^z \alpha(s)ds$, Eq.(4.1) can be rewritten in the lossless form as

$$j\frac{\partial u}{\partial z} - \frac{\beta_2(z)}{2}\frac{\partial^2 u}{\partial T^2} + \gamma(z)|u|^2 u = 0, \tag{4.3}$$

where $\gamma(z) = \gamma_0 \exp[-w(z)]$. We consider the interaction between two channels of a wavelength division multiplexed system (WDM). We spilt the field u into two parts,

$$u = u_1 + u_2, \tag{4.4}$$

where u_j is the field of channel j, $j = 1, 2$. Substituting Eq. (4.4) into Eq. (4.3) and ignoring the four wave mixing terms, we obtain

$$j\frac{\partial u_k}{\partial z} - \frac{\beta_2(z)}{2}\frac{\partial^2 u_k}{\partial T^2} = -\gamma(z)[|u_k|^2 + 2|u_l|^2]u_k, \quad k = 1, 2 \text{ and } l = 3 - k \tag{4.5}$$

Without loss of generality, we consider the interaction between a pulse of channel 1 in symbol slot 0 and a pulse of channel 2 in symbol slot m. We assume that the leading order solution of Eq. (4.5) is linear and treat the nonlinear terms appearing on the right hand side as perturbation. Assuming Gaussian pulse and QAM modulation, we have

$$u_1(0, T) = \sqrt{P} a_0 p(0, T), \tag{4.6}$$

$$u_2(0, T) = \sqrt{P} \sum_n a_n p(0, T - nT_s) \exp(-j\Omega t), \tag{4.7}$$

$$p(0, T) = \exp(-T^2/2T_0^2) \tag{4.8}$$

where T_s is the symbol interval, P is the peak power, Ω is the channel separation in radians, $p(0, T)$ is Gaussian pulse shape at $z = 0$, T_0 is the half-width at 1/e- intensity

point [15] and

$$a_n = \frac{x_n + iy_n}{\sqrt{2}}, \tag{4.9}$$

x_n and y_n are random variables that take values $\pm 1, \pm 3, ..., \pm(X-1)$ and $\pm 1, \pm 3, ..., \pm(Y-1)$ with equal probability, respectively. Using the perturbation technique [29, 35], the field envelope in channel k can be expanded as,

$$u_k = u_k^0 + \gamma_0 u_k^{(1)} + ..., \quad k = 1, 2 \tag{4.10}$$

where γ_0 is a small parameter and $u_k^{(m)}$ denotes the mth order solution. Here $u_k^{(0)}$ represents the 0^{th} order solution which satisfies

$$i\frac{\partial u_k^{(0)}}{\partial z} - \frac{\beta_2}{2}\frac{\partial^2 u_k^{(0)}}{\partial T^2} = 0. \tag{4.11}$$

Solving Eq. (4.11), the field $u_k^{(0)}$ is given by [15]

$$u_1^{(0)}(z, T) = \frac{\sqrt{P}T_0}{T_1} a_0 \exp\left[-\frac{T^2}{2T_1^2}\right], \tag{4.12}$$

$$u_2^{(0)}(z, T) = \frac{\sqrt{P}T_0}{T_1} \sum_n a_n \exp\left[-\frac{(T-\tau_n)^2}{2T_1^2} - j\Omega t + j\theta(z)\right], \tag{4.13}$$

where

$$T_1 = (T_0^2 - jS(z))^{1/2}, \tag{4.14}$$

$$\tau_n = nT_s + S(z)\Omega, \tag{4.15}$$

$$\theta(z) = \frac{S(z)\Omega^2}{2}, \tag{4.16}$$

and $S(z)$ is the accumulated dispersion given by

$$S(z) = \int_0^z \beta_2(s)ds. \tag{4.17}$$

Our reference frame is fixed to channel 1. The pulse in channel 2 moves with an inverse group speed of $\beta_2\Omega$ relative to channel 1.

Substituting Eq. (4.10) into Eq. (4.5) and collecting all the terms that are proportional to γ_0, we obtain

$$j\frac{\partial u_k^{(1)}}{\partial z} - \frac{\beta_2(z)}{2}\frac{\partial^2 u_k^{(1)}}{\partial T^2} = -\exp[-w(z)][|u_k^{(0)}|^2 + 2|u_l^{(0)}|^2]u_k^{(0)}. \;\; k = 1, 2 \text{ and } \; l = 3 - k. \tag{4.18}$$

To solve Eq.(4.18), we first derive the following identity. Consider a differential equation,

$$j\frac{\partial f}{\partial z} - \frac{\beta_2(z)}{2}\frac{\partial^2 f}{\partial T^2} = F(z, T), \tag{4.19}$$

where the forcing function $F(z, T)$ is of the form

$$F(z, T) = \eta(z)\exp\left\{-\sum_{k=1}^{3}[T - C_k(z)]^2 R_k(z)\right\}, \tag{4.20}$$

The solution of Eq. (4.19) is given by (Appendix C)

$$f(z, T) = -j\int_0^z \frac{\eta(s)}{\sqrt{\delta(z, s)R(s)}}\exp\left[-\sum_{k=1}^{3} C_k^2 R_k + \frac{C^2}{R}\right]\exp\left[-\frac{(D + jT)^2}{\delta(z, s)}\right]ds, \tag{4.21}$$

where

$$R = R_1 + R_2 + R_3, \tag{4.22}$$

$$C = C_1R_1 + C_2R_2 + C_3R_3, \tag{4.23}$$

$$D = \frac{jC}{R}, \tag{4.24}$$

$$\delta = \frac{1 - jRA(z,s)}{R}, \tag{4.25}$$

$$A(z,s) = 2\left[S(z) - S(s)\right]. \tag{4.26}$$

To find the first order correction for u_1 due to XPM term, $|u_2^{(0)}|^2 u_1^{(0)}$ in Eq. (4.18), we make use of the result given by Eq. (4.21). The forcing function $F(z,T)$ in this case is

$$\begin{aligned} F(z,T) &= -2\exp\left[-w(z)\right]\left|u_2^{(0)}\right|^2 u_1^{(0)}, \\ &= 2P^{3/2}a_0\eta(z)\sum_m\sum_n a_m a_n^* \exp\left\{-\sum_{k=1}^{3}\left[T - C_k(z)\right]^2 R_k(z)\right\}, \end{aligned} \tag{4.27}$$

where

$$\eta(z) = \frac{-T_0^3\exp\left[-w(z)\right]}{T_1(z)\left|T_1(z)\right|^2}, \tag{4.28}$$

$$C_1(z) = \tau_m(z),\ \ C_2(z) = \tau_n(z),\ \ C_3(z) = 0, \tag{4.29}$$

$$R_1 = R_3 = \frac{1}{2T_1^2}, \quad R_2 = \frac{1}{2(T_1^*)^2}. \tag{4.30}$$

Using Eq.(4.21), the first order correction for u_1 due to XPM is given by

$$u_1^{(1),XPM}(z,T) = i2P^{3/2}a_0\sum_m\sum_n a_m a_n^* X_{mn}(z,T) \tag{4.31}$$

where

$$X_{mn}(z,T) = \int_0^z \frac{\eta'(s)}{\sqrt{\delta(z,s)R(s)}} \exp\left[\frac{(D+iT)^2}{\delta(z,s)}\right] ds, \tag{4.32}$$

$$\eta'(s) = \eta(s) \exp\left(-\sum_{k=1}^{3} C_k^2 R_k + \frac{C^2}{R}\right), \tag{4.33}$$

The first order correction for u_1 due to SPM term, $\left|u_1^{(0)}\right|^2 u_1^{(0)}$, can be easily obtained from Eq. (4.31) by setting the angular frequency $\Omega = 0$, $\tau_m = \tau_n = 0$ and by replacing the XPM factor 2 with SPM factor 1, i.e.,

$$u_1^{(1),SPM}(z,T) = iP^{3/2} a_0 \left|a_0\right|^2 \int_0^z \frac{\eta(s)}{\sqrt{\delta(z,s)R(s)}} \exp\left(-\frac{T^2}{\delta(z,s)}\right) ds, \tag{4.34}$$

Total first order solution for u_1 is obtained by adding the SPM and XPM contributions,

$$u_1^{(1)} = u_1^{(1),SPM} + u_1^{(1),XPM}. \tag{4.35}$$

4.3 Variance calculation

The distortion due to nonlinearity is $\delta u_1 = \gamma_0 u_1^{(1)}$. The variance due to SPM and XPM is obtained by

$$\mathrm{Var}\left\{\delta u_1\right\} = \mathrm{E}\left\{\left|\delta u_1\right|^2\right\} - \left|\mathrm{E}\{\delta u_1\}\right|^2, \tag{4.36}$$

where $E\{.\}$ denotes the ensemble average. Since $u_1^{(1),SPM}$ is deterministic, it does not contribute to the variance, so we have

$$\mathrm{Var}\left\{\delta u_1\right\} = \mathrm{Var}\left\{\delta u_1^{XPM}\right\} = \mathrm{Var}\left\{\gamma_0 u_1^{(1),XPM}\right\}. \tag{4.37}$$

Using Eq. (4.31), the mean value of fiber nonlinearity distortion due to the XPM can be found as

$$\mathrm{E}\left\{\delta u_1^{XPM}\right\} = \mathrm{E}\left\{\gamma_0 u_1^{(1),XPM}\right\} = j2\gamma_0 P^{3/2} a_0 \sum_m \sum_n \mathrm{E}\left\{a_m a_n^*\right\} X_{mn}(z,T). \tag{4.38}$$

For QAM signals, we have

$$\mathrm{E}\left\{a_m a_n^*\right\} = K_1 \delta_{mn}, \tag{4.39}$$

where

$$K_1 = \mathrm{E}\left\{|a_m|^2\right\}, \tag{4.40}$$

and δ is Kronecker delta function. Using Eq. (4.39), Eq. (4.38) becomes

$$\mathrm{E}\left\{\delta u_1^{XPM}\right\} = j2\gamma_0 P^{3/2} a_0 K_1 \sum_m X_{mm}(z,T). \tag{4.41}$$

So the absolute square of the mean is obtained by

$$\left|\mathrm{E}\left\{\delta u_1^{XPM}\right\}\right|^2 = 4\gamma_0^2 P^3 |a_0|^2 K_1^2 \sum_m \sum_{m'} X_{mm}(z,T) X_{m'm'}^*(z,T). \tag{4.42}$$

Now, let us find the mean of absolute square of XPM nonlinearity. Using Eq. (4.31), we have

$$\mathrm{E}\left\{\left|\delta u_1^{XPM}\right|^2\right\} = \mathrm{E}\left\{\left|\gamma_0 u_1^{(1),XPM}\right|^2\right\} \tag{4.43}$$

$$= 4\gamma_0^2 P^3 |a_0|^2 \sum_m \sum_n \sum_{m'} \sum_{n'} \mathrm{E}\left\{a_m a_n^* a_{m'}^* a_{n'}\right\} X_{mn} X_{m'n'}^*. \tag{4.44}$$

For QAM signals, we can consider four cases:

Case 1: $m = n$ and $m' = n'$

In this case

$$\mathrm{E}\left\{a_m a_n^* a_{m'}^* a_{n'}\right\} = \mathrm{E}\left\{|a_m|^2|a_{m'}|^2\right\} \begin{cases} K_2 & m = m' \\ K_1^2 & m \neq m' \end{cases} \tag{4.45}$$

where

$$K_2 = \mathrm{E}\left\{|a_m|^4\right\}. \tag{4.46}$$

So,

$$\mathrm{E}\left\{\left|\delta u_1^{XPM}\right|^2\right\} = 4\gamma_0^2 P^3 |a_0|^2 \left(K_1^2 \sum_{\substack{m \\ m \neq m'}} \sum_{m'} X_{mm} X_{m'm'}^* + K_2 \sum_m |X_{mm}|^2 \right). \tag{4.47}$$

Case 2: $m \neq n$ and $m' \neq n'$

$$\mathrm{E}\left\{a_m a_n^* a_{m'}^* a_{n'}\right\} = K_1^2 \delta_{mm'} \delta_{nn'}. \tag{4.48}$$

So,

$$\mathrm{E}\left\{\left|\delta u_1^{XPM}\right|^2\right\} = 4\gamma_0^2 P^3 |a_0|^2 K_1^2 \sum_{\substack{m \\ m \neq n}} \sum_n |X_{mn}|^2. \tag{4.49}$$

Case 3: $m = n$ and $m' \neq n'$

$$\mathrm{E}\left\{a_m a_n^* a_{m'}^* a_{n'}\right\} = K_1 \mathrm{E}\left\{a_{m'}^* a_{n'}\right\}, \tag{4.50}$$

which equals to 0 since for QAM signals we have

$$\mathrm{E}\left\{a_{m'}^* a_{n'}\right\} = 0 \quad m' \neq n'. \tag{4.51}$$

Case 4: $m \neq n$ and $m' = n'$

Same logic as previous case, $\mathrm{E}\left\{a_m a_n^* a_{m'}^* a_{n'}\right\} = 0$.

Now, total mean of absolute square can be obtained by adding Eqs. (4.47) and (4.49)

$$\mathrm{E}\left\{\left|\delta u_1^{XPM}\right|^2\right\} = 4\gamma_0^2 P^3 |a_0|^2 \left(K_1^2 \sum_{\substack{m \\ m \neq m'}} \sum_{m'} X_{mm} X_{m'm'}^* + K_2 \sum_m |X_{mm}|^2 + K_1^2 \sum_{\substack{m \\ m \neq m'}} \sum_{m'} |X_{mm'}|^2 \right). \tag{4.52}$$

Finally, variance can be obtained by substituting Eqs. (4.42) and (4.52) in (4.36)

$$\begin{aligned} \mathrm{VAR}\left\{\left|\delta u_1^{XPM}\right|^2\right\} &= 4\gamma_0^2 P^3 |a_0|^2 \left(K_2 \sum_m |X_{mm}|^2 + K_1^2 \sum_{\substack{m \\ m \neq m'}} \sum_{m'} |X_{mm'}|^2 - K_1^2 \sum_m |X_{mm}|^2 \right), \\ &= 4\gamma_0^2 P^3 |a_0|^2 \left(\left(K_2 - K_1^2\right) \sum_m |X_{mm}|^2 + K_1^2 \sum_{\substack{m \\ m \neq m'}} \sum_{m'} |X_{mm'}|^2 \right). \end{aligned} \tag{4.53}$$

In the case of QPSK, $K_1 = K_2 = 1$. So for QPSK, we have

$$\mathrm{VAR}\left\{\left|\delta u_1^{XPM}\right|^2\right\} = 4\gamma_0^2 P^3 |a_0|^2 K_1^2 \sum_{\substack{m \\ m \neq m'}} \sum_{m'} |X_{mm'}|^2. \tag{4.54}$$

4.4 Results and discussion

To validate the analytical model, we carried out numerical simulations of the fiber-optic system shown in Fig. 4.1. Two WDM channels with QPSK modulation and Gaussian pulse shape are assumed. The wavelength division multiplexer (Mux) combines the two channels and the output of the multiplexer is launched to a multi-span

fiber-optic system with an amplifier spacing of 80 km. The fiber loss is exactly compensated with an ideal noiseless amplifier. Amplifiers ASE noise, laser phase noise, polarization effects, and the coherent receiver imperfections are ignored since the primary focus is to validate our analytical model for SPM and XPM impairments. After multi-span transmission, the channels are demultiplexed using an ideal filter whose bandwidth equals the channel spacing and passed to the optical receiver. The following parameters are used throughout the paper unless otherwise specified: nonlinear coefficient = 1.1 $W^{-1}km^{-1}$, amplifier spacing $L = 80$ km, channel spacing = 50 GHz, symbol rate = 10 Gbaud, pulse width T_{FWHM} (full width at half maximum) = 50 ps, QPSK modulation, and fiber loss $\alpha = 0.2$ dB/km.

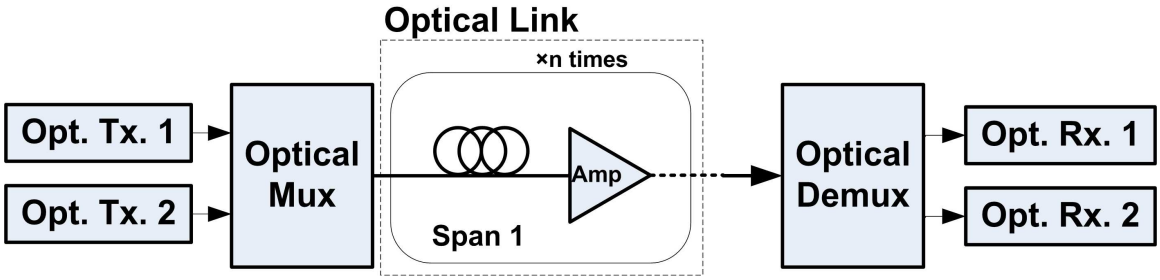

Figure 4.1: Multispan WDM fiber-optic system.

Fig. 4.2(a) shows the channels 1 and 2 input pulses in time domain. As can be seen, there is just one pulse in channel 1 and 18 pulses in channel 2. The rest of parameters are as follows: peak power $P_{peak} = 0$ dBm, fiber dispersion $\beta_2 = -10$ ps^2/km, and number of spans = 10. Fig. 4.2(b) shows the channels 1 and 2 output pulses after 10 spans. As the figure shows, faster channel (channel 1) walked off the slower channel (channel 2). Fig. 4.3 shows absolute square of the deviation of the signal field from the linear case. The distortions shown in Fig. 4.3 are due to dispersion and nonlinearity. The subscript 'num' and 'anl' correspond to the numerical and

analytical results, respectively. To compute the SPM deviation, we turned off channel 2 in both analytical model and numerical simulations. SPM deviation is obtained by subtracting the output field of channel 1 (when channel 2 is turned off) from its linear output obtained by assuming $\gamma_0 = 0$. XPM deviation is obtained by subtracting the output field of channel 1 when channel 2 is present, from the output field of channel 1 when channel 2 is absent. As can be seen, analytical SPM and XPM are in good agreement with numerical SPM and XPM.

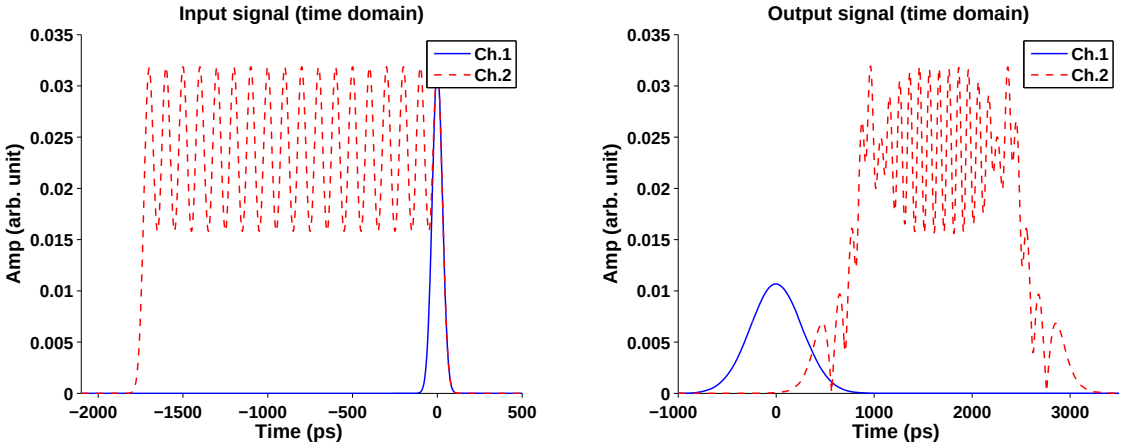

(a) (b)

Figure 4.2: Channel 1 and 2 (a) input signals, and (b) output signals. Following parameters were assumed: no. of symbols in channel 1 = 1, no. of symbols in channel 2 = 18, $P_{peak} = 0$ dBm, $\beta_2 = -10$ ps^2/km, no. of spans = 10.

To find the mean and variance numerically, Monte-Carlo simulation is carried out. Figs. 4.4(a) and 4.4(b) show the channels' input and output fields of a realization of Monte-Carlo simulation, respectively. In this case, there is one pulse in channel 1 and 38 pulses in channel 2. The rest of the parameters are as follows: peak power $P_{peak} = 0$ dBm, fiber dispersion $\beta_2 = -10$ ps^2/km, number of spans = 10, number of Monte-Carlo simulations = 2000. Fig. 4.5(a) shows the numerical and analytical first moments of SPM and XPM distortions. Fig. 4.5(b) shows the numerical and

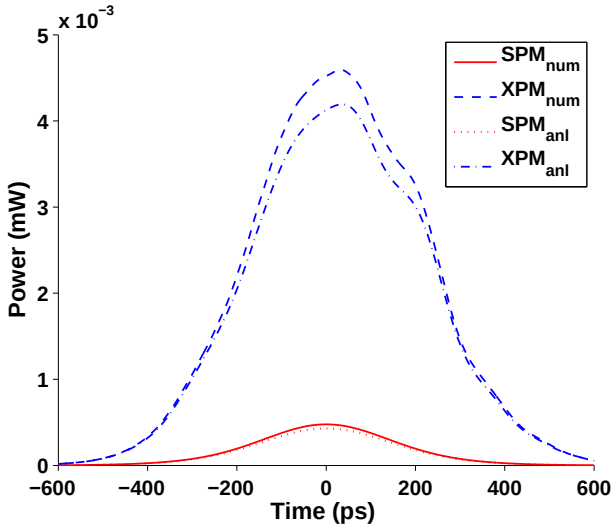

Figure 4.3: Numerical and analytical SPM and XPM signals induced on channel 1. Parameters are same as that of Fig. 4.2.

analytical second moments of SPM and XPM. Finally, Fig. 4.6 shows the numerical and analytical XPM variances. As can be seen in the Figs. 4.3, 4.5, and 4.6, the discrepancy between the analytical and numerical is more at the center of the pulse (higher power) when it is compared to the edges of the pulse (lower power). It is due to the fact that the first order perturbation technique is less accurate in higher power.

Fig. 4.7 shows the XPM variance versus peak power. As the peak power increases, the accuracy of the analytical model decreases which is due to the inaccuracy of first order perturbation technique. To get a better accuracy, higher order perturbation technique can be used [29]. From Eq. (4.54), we see that the XPM variance scales as P^3 which is in good agreement with numerical results. Fig. 4.8 shows the dependence of variance on the fiber dispersion. From Eq. (4.54), we realize that the variance is caused by the pulses overlapping. So, when the dispersion is low, pulses do not overlap significantly and hence, the variance is quite small. However, variance grows quickly

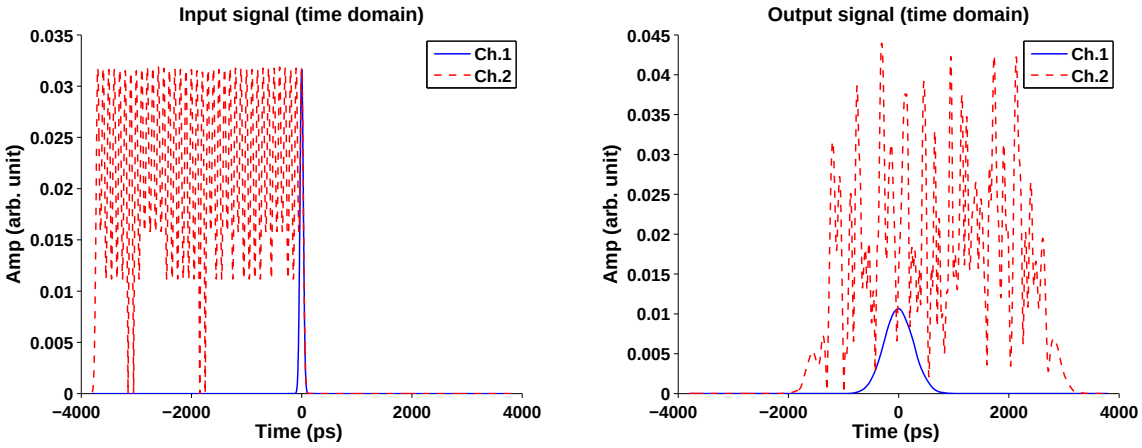

(a) (b)

Figure 4.4: One realization of Monte-Carlo simulation: (a) Channels 1 and 2 input signals in time domain. (b) Channels 1 and 2 output signals in time domain. Following parameters were assumed: no. of symbols in channel 1 = 1, no. of symbols in channel 2 = 38, $P_{peak} = 0$ dBm, $\beta_2 = -10$ ps^2/km, and no. of spans = 10.

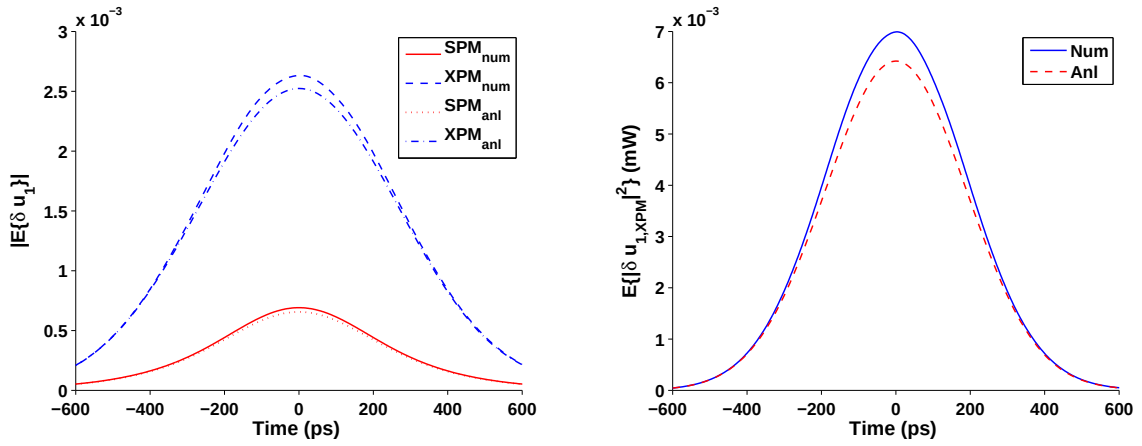

(a) (b)

Figure 4.5: (a) Absolute value of mean of XPM impairment, and (b) Mean of absolute square of XPM impairment. No. of Monte-Carlo simulations = 2000, and the other parameters are same as that of Fig. 4.4.

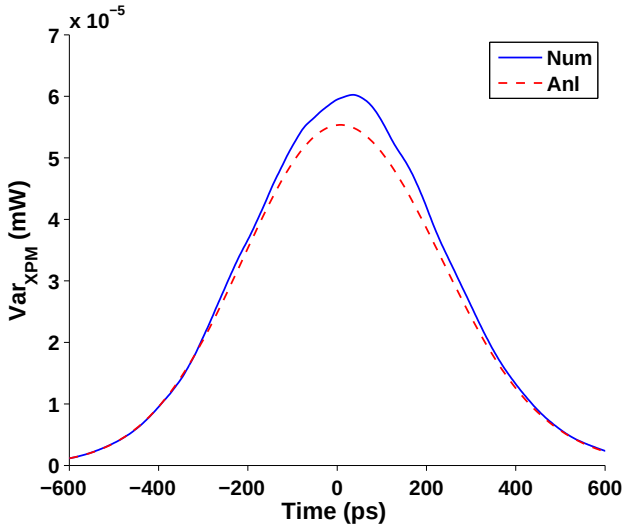

Figure 4.6: Variance of XPM impairment. Parameters are same as that of Fig. 4.4.

and beyond 10 ps^2/km, it decays slowly. When the dispersion is very large, the XPM effect is reduced since pulses walk-off quickly (Eq. (1.9)).

Fig. 4.9 shows the XPM variance versus number of spans. The variance is calculated by assuming that probe receiver is placed at the end of each span and dispersion is fully compensated before the variance calculation. As can be seen in the Fig. 4.9, the variance of XPM distortion increases almost linearly with the number of spans. The quick and rough estimate of the XPM penalty can be done by using the slope of the curve in Fig. 4.9 after one or two spans and it can be extrapolated for a fiber-optic system with larger number of spans. As can be seen, the discrepancy between analytical and numerical is less than 10% for number of span less than 16. The discrepancy increases as the number of spans increases which is due to the inaccuracy of first order perturbation technique for long reach and large power.

Fig. 4.10 shows the XPM variance versus channel spacing. As can be seen, XPM variance decreases dramatically as channel spacing increases. This is because as the

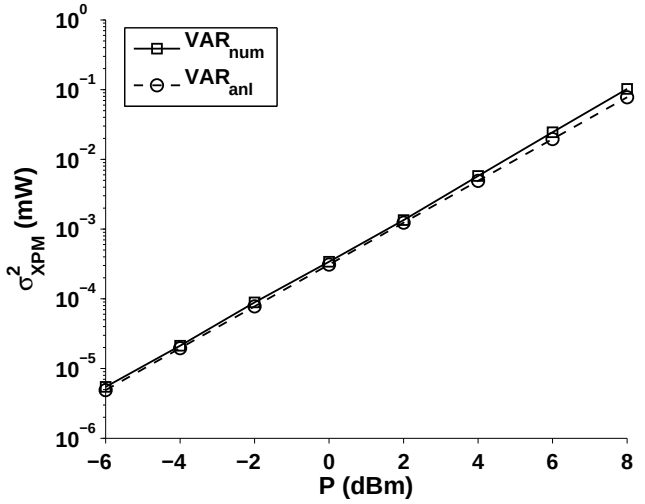

Figure 4.7: XPM variance versus peak power. Following parameters were assumed: no. of symbols in channel 1 = 1, no. of symbols in channel 2 = 38, $\beta_2 = -10$ ps^2/km, no. of spans = 10, no. of Monte-Carlo simulations = 2000.

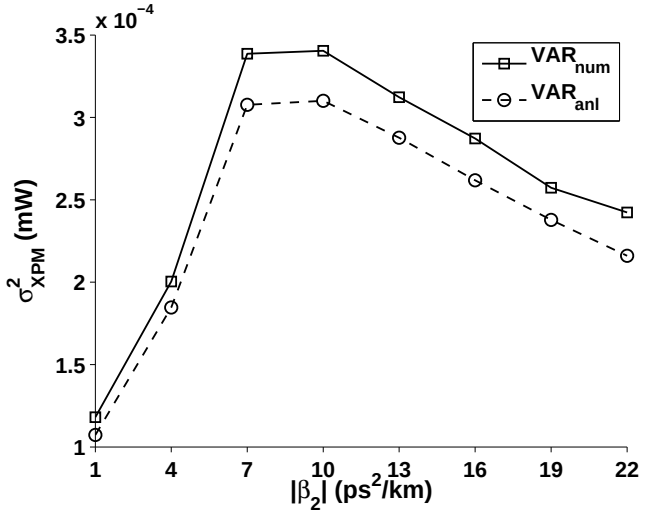

Figure 4.8: XPM variance versus fiber dispersion. Following parameters were assumed: no. of symbols in channel 1 = 1, no. of symbols in channel 2 = 76, $P_{peak} = 0$ dBm, no. of spans = 10, no. of Monte-Carlo simulations = 2000.

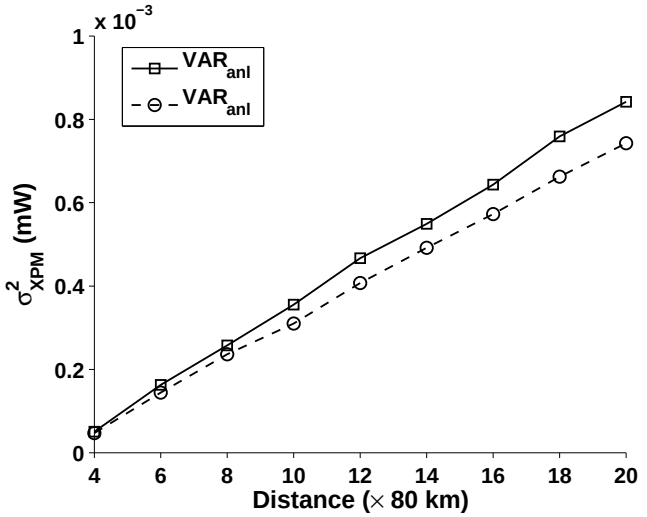

Figure 4.9: XPM variance versus no. of spans. Following parameters were assumed: no. of symbols in channel 1 = 1, no. of symbols in channel 2 = 71, $P_{peak} = 0$ dBm, $\beta_2 = -10$ ps^2/km, no. of Monte-Carlo simulations = 2000.

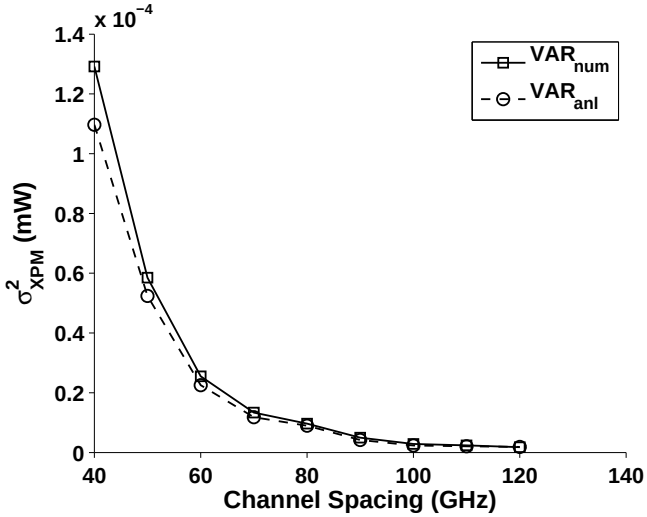

Figure 4.10: XPM variance versus channel spacing. Following parameters were assumed: no. of symbols in channel 1 = 1, no. of symbols in channel 2 = 10, $P_{peak} = 0$ dBm, $\beta_2 = -10$ ps^2/km, no. of spans = 10, no. of Monte-Carlo simulations = 2000.

channel spacing increases, the "fast" channel walks off quickly the "slow" channel (Eq. (1.9)) and hence, the nonlinear interaction time is reduced. Later in Chapter 6, multi-core fiber (MCF) is applied in WDM system to increase the channel spacing in order to mitigate the inter-channel nonlinear impairments.

4.5 Conclusions

A first order perturbation technique for SPM and XPM effects for QAM system is developed. We also developed an analytical expression for the variance of XPM impairment. From the analytical model we have found that the nonlinear impairment scales as P^3. In addition, a linear relation between the nonlinear impairment variance and system reach was found which helps reduction of computational cost by extrapolating the carve when the slope of the line is known. Simulation results showed that the analytical expression is in good agreement with numerical results.

Chapter 5

Reduction of nonlinear impairments in fiber transmission system using fiber and/or transmitter diversity

5.1 Introduction

Coherent detection techniques have enabled the spectrally efficient modulation formats. However, as the spectral efficiency increases, the signal to noise ratio (SNR) required to reach a given bit error ratio (BER) increases too [45]. Although the SNR can be increased by launching large signal power into fiber, the performance degradation occurs due to fiber nonlinear effects (Fig. 1.11). In Chapters 2, 3, and 4, nonlinear impairment variance was obtained to scale as P^3, where P is fiber input

launch power (see Eqs. (2.22) and (4.53)). In this chapter, it is proposed to use multiple core/fiber architecture so that the power launched to each core/fiber could be reduced and thereby, the nonlinear impairments can be minimized.

Typically, the transmission system cost scales linearly with fiber counts. This is because the number of photonic/optoelectronic devices such as optical amplifiers and Mach-Zehnder modulators (MZMs) in a system are directly proportional to fiber counts. However, in one of the proposed fiber diversity technique, the fiber count is increased without having to increase the number of photonic/optoelectronic devices. Since the fiber cost is only a small fraction of the total system cost, it is expected that significant performance improvement can be obtained with only a modest increase in system cost. Typically, in a terrestrial fiber cable, there could be as many as 200 fibers, out of which about 10 fibers are used for communication. The other "dark" fibers could be used to carry the data using the technique described here.

The multi-core fibers (MCFs) with each core resembling the standard single-mode fiber can be fabricated with negligible cross-talk between the signals in the neighboring cores [47]. Recently, there has been a significant interest in using multi-core fiber systems to increase the system capacity [9–12, 48, 49]. The proposed techniques can also be applied in these systems to increase the performance of the system.

The optical signals propagating in different cores/fibers undergo different amounts of phase shifts and timing delays. In this chapter, we consider two types of equalizers to compensate the phase shifts and delays. First, the optical equalizer consisting of adaptive phase shifters and time shifters compensate for the channel effect [46]. The phase shifters and time shifters are adjusted such that the power meter connected to the combiner shows the maximum power. Next, we consider the electrical equalizer in

which the phase shifts and timing shifts are adjusted electrically at the transmitter. This technique requires transmitter diversity. Each transmitter needs channel state information (CSI) which can be sent to the transmitter periodically with a low data rate line from receiver to transmitter. In this chapter, a technique is proposed to extract the CSI.

This chapter is organized as follows. Multi-core/fiber system configuration is explained in Section 5.2. In Section 5.3, the effect of polarization mode dispersion (PMD) is investigated in multi-core/fiber communication system. Simulation results for the proposed system are given in Section 5.4. At the end, in Section 5.5, the contributions of this chapter are summarized.

5.2 Multi-core/fiber system configuration

Fig. 5.1 shows the schematic of the fiber-optic system that uses multiple fibers or multi-core fibers. The output of the transmitter is divided equally among M cores/fibers using a power splitter. From Eqs. (2.22) and (4.53), we know that if the input power is reduced by a factor of M, the intrachannel/inter-channel nonlinear impairment variance is decreased with a factor of M^3 which improves system performance significantly.

The optical field in each fiber can be written as

$$\psi_m(t,z) = q_m(t,z)\exp\left[i(\omega t - \beta_{0,m}z)\right] \quad m = 1,2,...,M. \tag{5.1}$$

where $\beta_{0,m}$ is the mean propagation constant in the m^{th} core/fiber and $q_m(t,z)$ is the complex field envelope in the m^{th} core/fiber. The evolution of field envelope, q_m, in

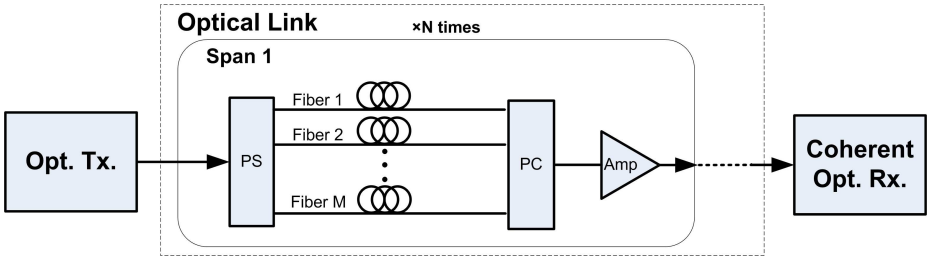

Figure 5.1: Multi-core/fiber system architecture; M: number of cores/fibers; N: number of spans; Opt. Tx.: optical transmitter; PS: power splitter; PC: power combiner; Amp: amplifier; Opt. Rx.: optical receiver.

the fiber is governed by the nonlinear Schrodinger equation (NLSE)

$$i\left(\frac{\partial q_m}{\partial z}+\beta_{1,m}(z)\frac{\partial q_m}{\partial t}\right)-\frac{\beta_{2,m}}{2}\frac{\partial^2 q_m}{\partial t^2}+\gamma_m\left|q_m\right|^2 q_m=\left(\Delta\beta_{0,m}(z)+i\frac{\alpha_m}{2}\right)q_m, \quad (5.2)$$

where $\beta_{1,m}$, $\beta_{2,m}$, α_m, and γ_m are inverse group speed, second order dispersion, loss, and nonlinear coefficient of the m^{th} core/fiber, respectively. $\Delta\beta_{0,m}(z)=\beta_0-\beta_{0,m}(z)$ where β_0 is the propagation constant, at $z=0$ of a reference fiber. $\Delta\beta_{0,m}$ is the deviation of propagation constant from its mean value due to irregularities in the fiber geometrics and it causes different phase shifts at the end of cores/fibers. In addition there may be deviation in the inverse group speed (β_1). Let $\Delta\beta_{1,m}(z)=\beta_1-\beta_{1,m}(z)$ where β_1 is inverse group speed, at $z=0$ of a reference fiber. Using the transformation $T=t-\beta_1 z$ and $Z=z$, Eq. (5.2) can be rewritten as

$$i\left(\frac{\partial q_m}{\partial Z}+\Delta\beta_{1,m}(Z)\frac{\partial q_m}{\partial T}\right)-\frac{\beta_{2,m}}{2}\frac{\partial^2 q_m}{\partial T^2}+\gamma_m\left|q_m\right|^2 q_m=\left(\Delta\beta_{0,m}(Z)+i\frac{\alpha_m}{2}\right)q_m. \quad (5.3)$$

If we ignore fiber dispersion and nonlinearity ($\beta_{2,m}=\gamma_m=0$), the fiber envelope at

the distance L is

$$q_m(T, L) = q_m(T - d_m, 0) \exp\left[-ig_m - \frac{\alpha_m}{2}L\right], \tag{5.4}$$

where

$$d_m = \int_0^L \Delta\beta_{1,m}(Z)dZ, \tag{5.5}$$

$$g_m = \int_0^L \Delta\beta_{0,m}(Z)dZ. \tag{5.6}$$

Due to deviation in propagation constants ($\Delta\beta_{0,m}$) and inverse group speeds ($\Delta\beta_{1,m}$), the optical signals reach at the end of cores/fibers at different times with different phase shifts (inter-core/fiber dispersion). Inverse group speed variations ($\Delta\beta_{1,m}$) cause the fiber-optic link to act as a low pass channel leading to performance degradations (Fig. 5.2). Fig. 5.2 shows the effect of inverse group speed variations on multi-core/fiber system. As can be seen, for a 2-core/fiber system, channel frequency response acts as a low pass filter (LPF) leading to power degradation. Moreover, propagation constant variations ($\Delta\beta_{0,m}$) cause loss of power when the signal fields are added in power combiner. Fig. 5.3 shows the effect of propagation constant variations on multi-core/fiber system. As can be seen, for a 2-core/fiber system, channel frequency response is in deep fade causing power loss. Inter-core/fiber dispersion is similar to multipath effect in wireless communication. Fig. 5.4 shows the similarity between multipath effect in wireless communication and inter-core/fiber dispersion effect in multi-core/fiber system. Multipath in wireless communication causes ISI and fading which is similar to that of inter-core/fiber dispersion. Although the electrical equalizer in the coherent receiver can compensate for the low pass characteristic of

the channel in multi-core/fiber system, noise enhancement due to the equalizer leads to performance degradation. Unlike the wireless communication, we have access to different paths (cores/fibers) separately in multi-core/fiber system which makes the equalization more efficient in this system. To mitigate these problems, we propose two kinds of equalizers.

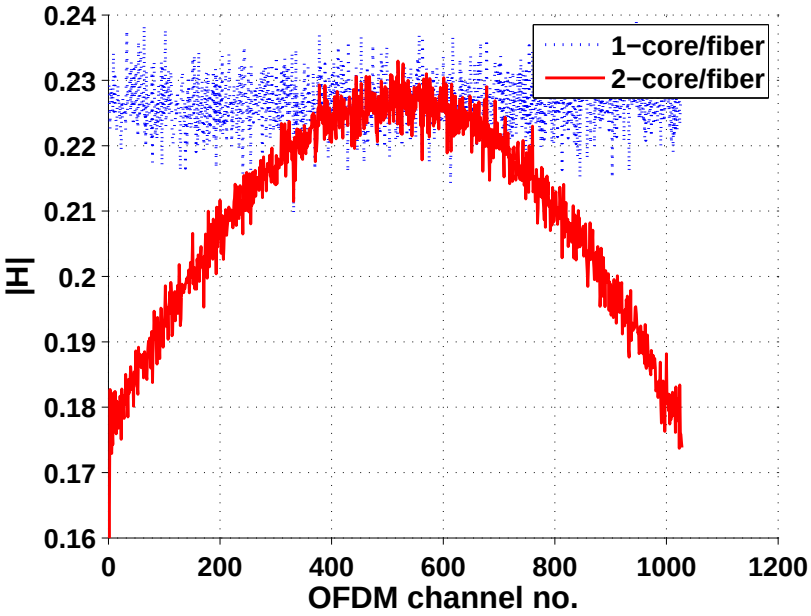

Figure 5.2: One realization of fiber-optic channel frequency response for single-core fiber and 2-core/fiber systems. Following parameters were assumed: No. of OFDM channels: 1024, $\sigma_{\beta_0} = 0$ rad/m and $\sigma_{\beta_1} = 10^{-3}$ ps/m.

In the first scenario, we used adaptive phase and time shifters in optical domain, which can be controlled by a power meter [46]. Fig. 5.5 shows the block diagram of this equalizer in unrepeatered case; power meter measures the output of the combiner and the phases (ϕ) and delays (T) are adjusted such that the output of combiner is maximum. This also ensures that the signal fields at the fiber outputs are added in phase. There are several techniques to adjust the phase shifts and time shifts. It can

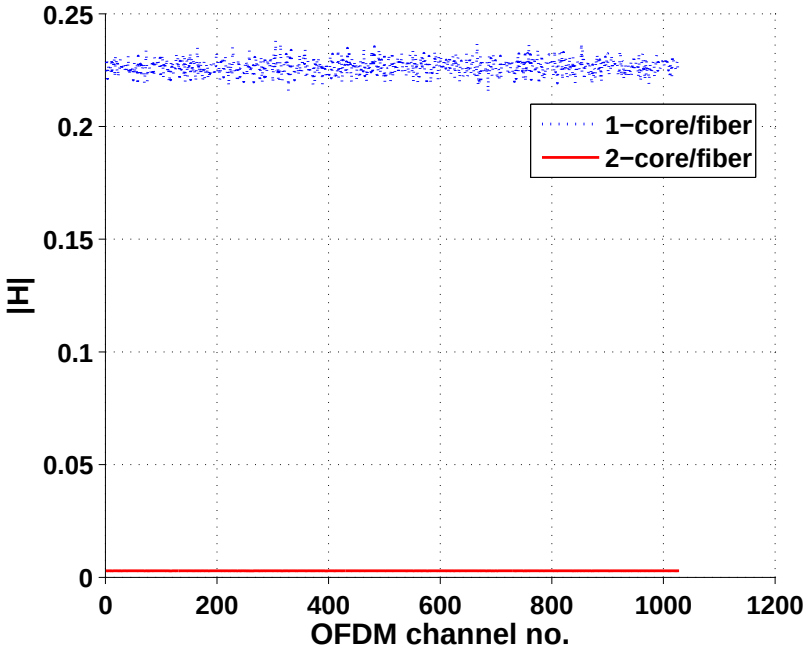

Figure 5.3: One realization of fiber-optic channel frequency response for single-core fiber and 2-core/fiber systems. Following parameters were assumed: No. of OFDM channels: 1024, $\sigma_{\beta_0} = 10^4$ rad/m and $\sigma_{\beta_1} = 0$ ps/m.

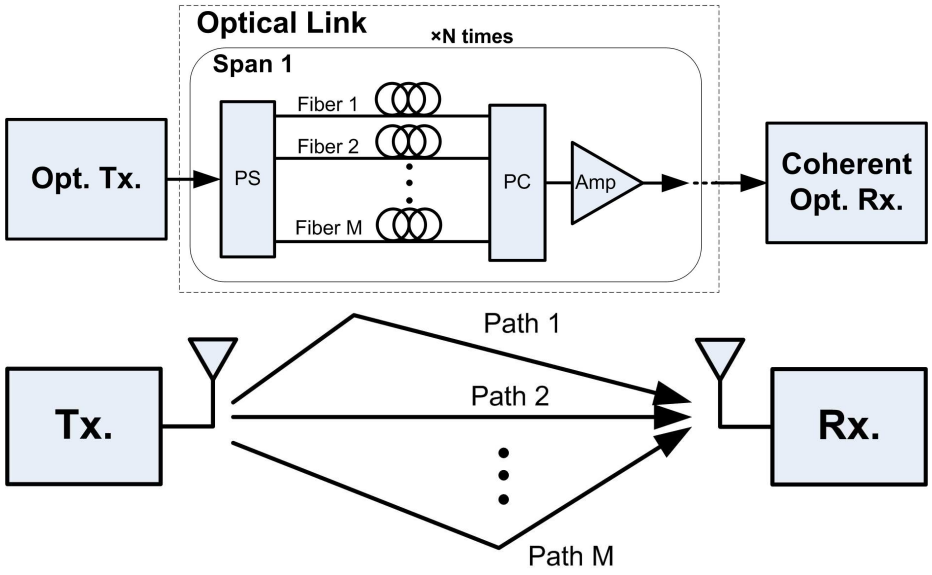

Figure 5.4: Similarity between inter-core/fiber dispersion effect in multi-core/fiber system and multipath effect in wireless system.

be realized using a lens-grating pair and two mirrors [50]. The output of the fiber is directed to the grating for spatial separation of optical frequency components. The output of the grating is collected by a lens and then reflected by a mirror placed at the focal plane of the lens. The reflected light passes through the lens again and diffracted again by the grating. By adjusting the rotation angles of the mirror, the phase delay and group delay can be controlled independently. Response time of this device is a few hundred microseconds. An advantage of this device is that the adaptive phase shifts and time shifts can be achieved using the single device. Several techniques of adaptive delay control using the piezoelectric fiber stretcher are discussed in [51]. Other choice for the adaptive time delay without using the delay lines and demultiplexing will be to utilize a slow light technique [52]. In a recent research [53], spatial light modulators (SLMs) have been proposed to compensate for intermodal delays/phase shifts in a multi-mode fiber (MMF). The amplitude and phase of individual cells of SLMs can be dynamically controlled within a few microseconds. The SLMs can be used as an adaptive time and phase-shifter in multi-core/fiber systems. Typically, the optical phase in a fiber could vary in a time scale of a few milliseconds. The electrical signal processing (ESP) unit placed after power meter and the optical devices connected to ESP could respond at a time scale faster than a few milliseconds.

The unrepeatered system can also be expanded to multi-span fiber case (Fig. 5.6). In this system, in-line adaptive phase and time shifters are used before each combiner in each span. As a result, there is no power loss due to phase mismatch in each combiner. In multi-span case, we can also use a single optical equalizer just before the receiver (Fig. 5.7). However, in this case, output of the cores/fibers should be amplified separately.

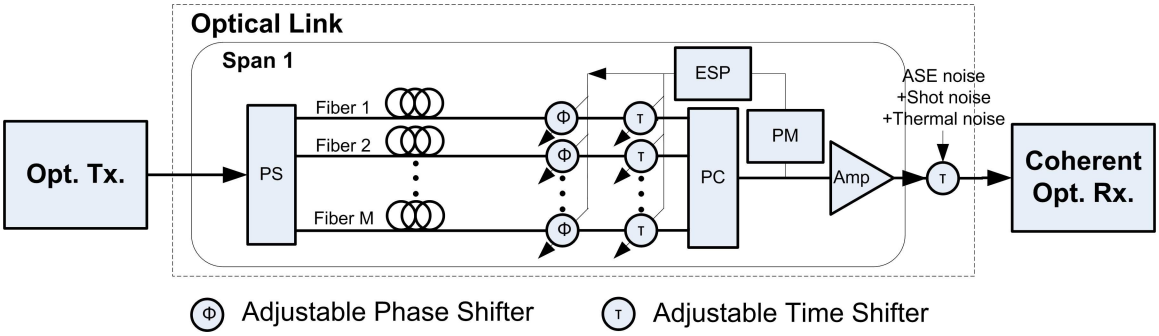

Figure 5.5: Unrepeatered multi-core/fiber system architecture with optical equalizer; M: number of cores/fibers; Opt. Tx.: optical transmitter; PS: power splitter; PC: power combiner; PM: power meter; ESP: electrical signal processor; Amp: amplifier; Opt. Rx.: optical receiver.

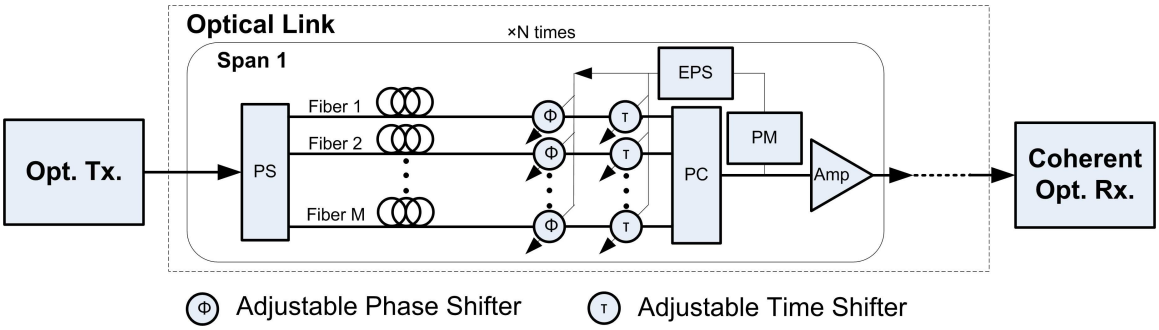

Figure 5.6: Multi-span multi-core/fiber system architecture with in-line optical equalizer; M: number of cores/fibers; N: number of spans; Opt. Tx.: optical transmitter; PS: power splitter; PC: power combiner; PM: power meter; ESP: electrical signal processor; Amp: amplifier; Opt. Rx.: optical receiver.

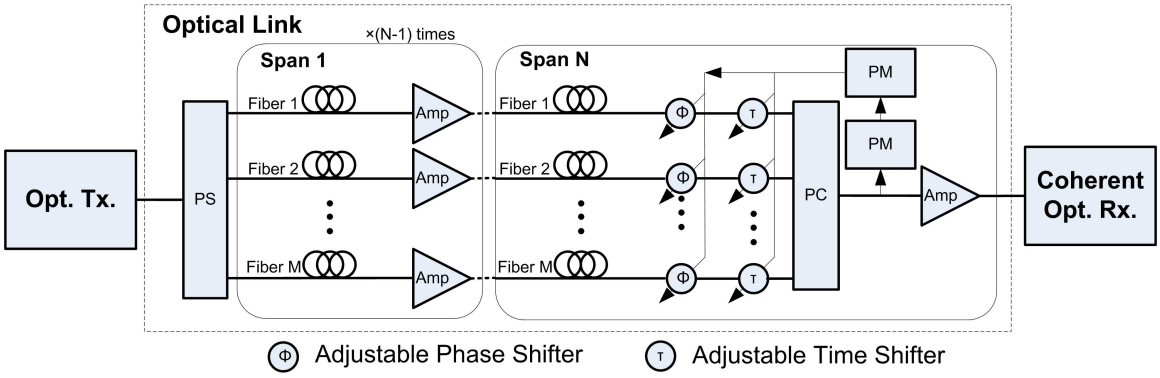

Figure 5.7: Multi-span multi-core/fiber system architecture with optical equalizer at the receiver; M: number of cores/fibers; N: number of spans; Opt. Tx.: optical transmitter; PS: power splitter; PC: power combiner; PM: power meter; ESP: electrical signal processor; Amp: amplifier; Opt. Rx.: optical receiver.

In the second scenario, the phase and time shifts are adjusted electrically at transmitter by using multi-transmitter scheme (Fig. 5.8). Thus, transmitter needs CSI to provide the proper phase and time shifts for each fiber. CSI can be provided at transmitter with a low data rate line from receiver to transmitter. Similar to first scenario, by adjusting proper phase and time shifts at transmitter, we make sure that there is no power loss at combiner. In this scheme, all the modulators share the same laser. For example, instead of a single 40 Gbaud modulator, we need four 10 Gbaud modulators when $M = 4$. Simulation results show that these two scenarios have roughly the same efficiency.

As discussed earlier, the problem with different phase shifts and time delays resemble multipath effect in wireless communication. Multipath causes power loss (fading) and inter-symbol interference (ISI). In both multi-core/fiber and wireless systems, ISI can be handled by equalizers. In wireless, fading can be mitigated by diversity techniques [54, 55]. However in multi-core/fiber case, while we have access to different paths separately, phase shifts and time delays can be compensated before adding the

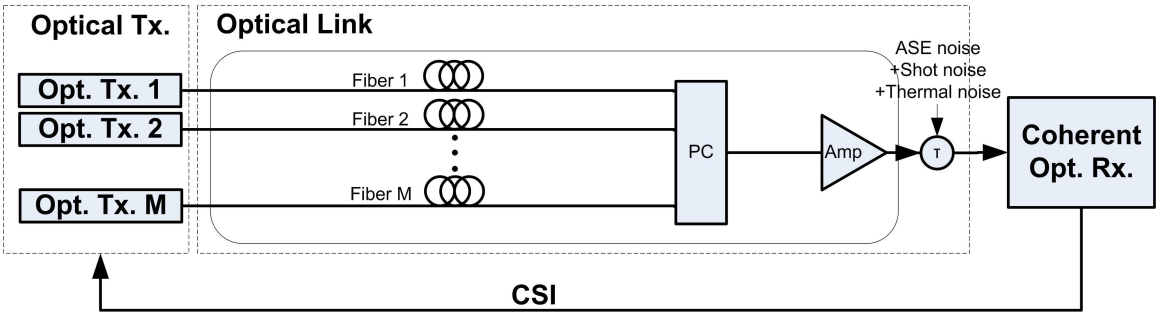

Figure 5.8: Unrepeatered multi-core/fiber system architecture with multi-transmitter (electrical equalizer); M: number of cores/fibers; Opt. Tx.: optical transmitter; PC: power combiner; Amp: amplifier; Opt. Rx.: optical receiver; CSI: channel state information.

signals.

In wireless communication system, the CSI can be obtained by different methods. One well-known method is to use training sequence. In this method, a known signal is sent first. Then by utilizing an adaptive equalization method, filter coefficients at the receiver are adjusted to compensate the channel filter [54]. Another technique which mitigates the multipath effects is called RAKE receiver which is used in code division multiple access (CDMA) spread-spectrum systems [54, 55]. In this method, a matched filter (MF) matched to the expected receive signal is used at receiver side. Location of peaks in the output of MF gives the time delays of different paths. Then each delay is compensated in one finger of RAKE receiver and then in-phase signals are added [56].

In fiber-optic communication with fiber diversity, since we have access to the different paths, a simple equalization technique is proposed here: let the channel transfer function from transmitter m to the receiver be $H_m(f)$. We turn off all the transmitters except the transmitter m and a training sequence is sent from this transmitter.

The transfer function $H_m(f)$ is estimated at the receiver and inverse transfer function $H_m^{-1}(f)$ is calculated. This information is sent back to the transmitter m and the transmitter signal is multiplied by $H_m^{-1}(f)$ to compensate the effect of channel. This procedure is repeated for all the transmitters. In our simulation, since we used orthogonal frequency division multiplexing (OFDM), one tap channel coefficient was obtained for each subcarrier by utilizing this method.

5.3 Polarization mode dispersion effect

So far, we ignored the polarization effects. To include the polarization mode dispersion (PMD), the scalar NLSE (Eq. (5.3)) should be replaced with the vector NLSE,

$$\begin{aligned} &i\left(\tfrac{\partial q_{m,x}}{\partial Z}+\Delta\beta_{1x,m}(Z)\tfrac{\partial q_{m,x}}{\partial T}\right)-\tfrac{\beta_{2,m}}{2}\tfrac{\partial^2 q_{m,x}}{\partial T^2}+\gamma_m\left\{|q_{m,x}|^2+\tfrac{2}{3}|q_{m,y}|^2\right\}q_{m,x}\\ &=\left(\Delta\beta_{0x,m}(Z)+i\tfrac{\alpha_m}{2}\right)q_{m,x}, \end{aligned} \tag{5.7}$$

$$\begin{aligned} &i\left(\tfrac{\partial q_{m,y}}{\partial Z}+\Delta\beta_{1y,m}(Z)\tfrac{\partial q_{m,y}}{\partial T}\right)-\tfrac{\beta_{2,m}}{2}\tfrac{\partial^2 q_{m,y}}{\partial T^2}+\gamma_m\left\{|q_{m,y}|^2+\tfrac{2}{3}|q_{m,x}|^2\right\}q_{m,y}\\ &=\left(\Delta\beta_{0y,m}(Z)+i\tfrac{\alpha_m}{2}\right)q_{m,y}, \end{aligned} \tag{5.8}$$

where $q_{m,x}$ and $q_{m,y}$ are the $x-$ and $y-$ polarization components of the optical field envelope propagating in fiber m, $\Delta\beta_{0x,m}$ and $\Delta\beta_{0y,m}$ are the deviation of propagation constants from the mean value, and $\Delta\beta_{1x,m}$ and $\Delta\beta_{1y,m}$ are the deviation of inverse group speeds (relative to reference frame with inverse group speed β_1) for $x-$ and $y-$ polarization components, respectively. The fibers are modeled as a randomly varying birefringent medium that is a cascade of many short fiber sections with constant birefringence [57]. The short fiber sections have identical length z_h and identical magnitude of birefringence $\Delta n = c\,(\Delta\beta_{1x} - \Delta\beta_{1y})$. The PMD parameter D_p and

birefringence Δn are related by

$$D_p = \sqrt{\frac{8}{3\pi}} \left(\frac{\Delta n}{c} \right) \sqrt{z_h}. \tag{5.9}$$

Here c is the speed of light in free space. At fictitious junctions between fiber sections, random axial rotation and addition of random phase difference between the two field components is introduced by multiplying the field envelopes by the matrix

$$M_{\theta,\varphi} = \begin{bmatrix} \cos\theta & e^{i\varphi}\sin\theta \\ -e^{-i\varphi}\sin\theta & \cos\theta \end{bmatrix}, \tag{5.10}$$

where θ and φ are uniformly distributed in the range of 0 to 2π, and 0 to π, respectively [58]. Fig. 5.9 shows the multi-core/fiber system architecture with an optical equalizer that takes into account the polarization effects. The output of the fiber-optic link passes through the adjustable time shifter. The polarization beam splitter (PBS) splits the optical signal into $x-$ and $y-$ polarization components. Since the two polarization components acquire different amount of phase shifts due to propagation, it is necessary to adjust their phases adaptively using the adjustable phase shifters. The $x-$ and $y-$ polarization components of the optical signals propagating in different fibers are combined separately and the outputs of combiners are connected to the front-end of the coherent receiver. Although the $x-$ and $y-$ polarization components acquire different amounts of group delays, it is not necessary to adjust their timing shifts separately. A single adjustable time shifter per fiber (as in the scalar case) is sufficient. The differential group delay between the polarization components is equalized by the one-tap equalizer in the electrical domain.

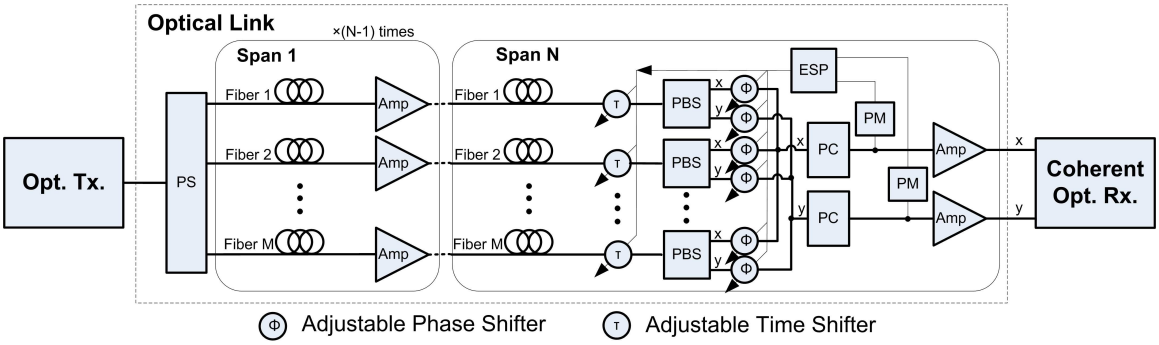

Figure 5.9: Multi-span multi-core/fiber system architecture with optical equalizer at the receiver; M: number of cores/fibers; N: number of spans; Opt. Tx.: Optical Transmitter; PS: Power Splitter; PC: Power Combiner; PBS: polarization beam splitter; PM: Power Meter; ESP: electrical signal processor; Amp: Amplifier; Opt. Rx.: Optical Receiver.

5.4 Simulation setup and results

Here we present simulation results for five scenarios. In the first one, we consider unrepeatered (single-span) fiber system with optical equalizer, and in the second one we consider the same system with multi-transmitter (electrical equalizer). In the third case, multi-span fiber system with in-line optical equalizers is presented. In the fourth case, multi-span system with optical equalizer at the receiver is considered, and in the last case, effect of PMD on this system is investigated.

We carried out the numerical simulation of the multi-core/fiber configuration with the following fiber parameters: fiber loss, $\alpha_m = 0.2$ dB/km, fiber dispersion $\beta_{2,m} = -22.1$ ps^2/km, and nonlinear coefficient $\gamma_m = 1.1$ (W.km)$^{-1}$. We assume that these fibers are nearly identical. However $\beta_{0,m}$ and $\beta_{1,m}$ could fluctuate due to temperature and other environmental factors. We further assumed that the propagation constant $\beta_{0,m}$ and inverse group speed $\beta_{1,m}$ vary randomly over the fiber length and in each fiber, $\beta_{0,m}$ and $\beta_{1,m}$ remain constant over a correlation length of 200 m. $\Delta\beta_{0,m}$

and $\Delta\beta_{1,m}$ are assumed to be zero mean Gaussian random variables with standard deviation $\sigma_{\beta_0} = 10^4$ rad/m and $\sigma_{\beta_1} = 10^{-3}$ ps/m. NLSE is solved over a length of 200 m with values of $\beta_{0,m}$ and $\beta_{1,m}$ picked from Gaussian distributions. The process is repeated until the end of span. As a result, the signal in each fiber experiences different amounts of phase shifts and delays. Because of the adjustable phase shifters and time delays at the end of cores/fibers, the performance degradation does not occur even when the standard deviation of β_0 and β_1 are larger. The phase shifter is varied in the range of $-\pi$ to π with a step of 0.001 and the corresponding range for the time delay is 0 to 1 ns with a step size of 1 ps such that the output of the combiner is maximum. In Sections 5.4.1 to 5.4.4, scalar NLSE is solved ignoring the polarization effects.

For our simulation, we used optical orthogonal frequency division multiplexing (OOFDM) (Fig. 5.10) [59–62]. However, as the goal is to mitigate nonlinearity by dividing power between different cores/fibers, any kind of modulation techniques can be used. The parameters of OFDM are as follows: symbol rate, $R_s = 12.5$ Gsym/s, number of subcarriers = 1028, with 7.78% of cyclic prefix. Quadrature amplitude modulation (QAM) technique is used for each subcarrier. Total number of OFDM blocks is 1200. Fig. 5.10 shows the block diagram of a OOFDM system. To estimate channel coefficients for each subcarrier, 16 training sequence blocks are sent at first. Then, a single-tap equalizer is used for channel compensation [62]. However, in the case of transmitter diversity, channel coefficients are obtained separately for each core/fiber. Then coefficients of each channel are multiplied by transmitting data at corresponding transmitter to compensate the effect of the channel. The linewidths of transmitter and local oscillator (LO) lasers are assumed to be 100 kHz. To estimate

the phase, 8 pilot subcarriers are used [13].

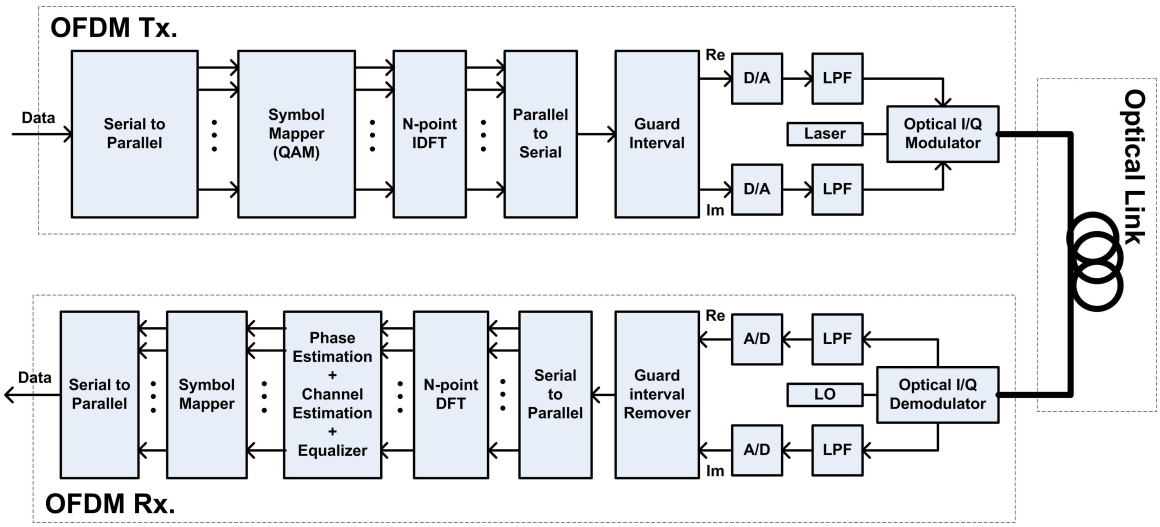

Figure 5.10: Optical OFDM system; IDFT: inverse discrete Fourier transform; DFT: discrete Fourier transform; A/D: analog to digital converter; D/A: digital to analog converter; LO: local oscillator; LPF: low pass filter.

For the unrepeatered system, a pre-amplifier was used before the balanced coherent receiver. For this system, the following parameters were assumed: local oscillator power $P_{LO} = 10$ dbm, responsivity of photodetector $R = 1$ A/W, input impedance $R_{in} = 50\ \Omega$, and amplifier noise figure $n_{sp} = 1.5$. Amplifier gain was fixed at 25 dB. Variances of ASE-LO beat noise, shot noise and thermal noise are calculated as done in ref. [63] and added as white Gaussian noise at the receiver.

In the case of multi-span system, same receiver was assumed; however, amplifiers were used at the end of each 80 km fiber span to compensate the loss of fiber (Fig. 5.6). The simulation results of five scenarios are as follows.

5.4.1 Case 1: unrepeatered fiber system with fiber diversity and optical equalizer

Fig. 5.11 shows the BER versus the fiber launch power, for different number of cores/fibers $M = 1, 2, 4$, and 8. QPSK modulation is used in each subcarrier of the OFDM, and transmission line consists of 1 span of 300 km multi-fiber/multi-core fiber. Due to power splitting between multiple cores/fibers, nonlinearity decreases in each core/fiber and performance improvement is achieved. In this case, it can be seen the optimum launch power increases from 10 dBm in the case of single-core fiber to 16 dBm (total power) when 8-core/fiber is used. The performance improvement (Q-factor) using 8-core/fiber configuration is about 6.2 dBQ_{20} as compared to single-core fiber configuration. Fig. 5.12 shows the minimum BER (after optimizing the launch power) versus transmission distance. As can be seen, the transmission distance is limited to 260 km using single-core fiber configuration which can be extended to 310 km using 8-core/fiber configuration.

5.4.2 Case 2: unrepeatered fiber system with fiber diversity and transmitter diversity

Similar to case 1, BER versus the fiber launch power for QPSK is shown in Fig. 5.13. As can be seen, in the high launch power (high SNR), the efficiency of this configuration is almost the same as previous case in which optical equalizer was used. In the low launch power (low SNR), nonlinearity of the fiber is not significant and benefit obtained by multi-core/fiber structure is negligible. On the other hand, power loss due to non-ideal channel estimation in multi-core/fiber case leads to performance

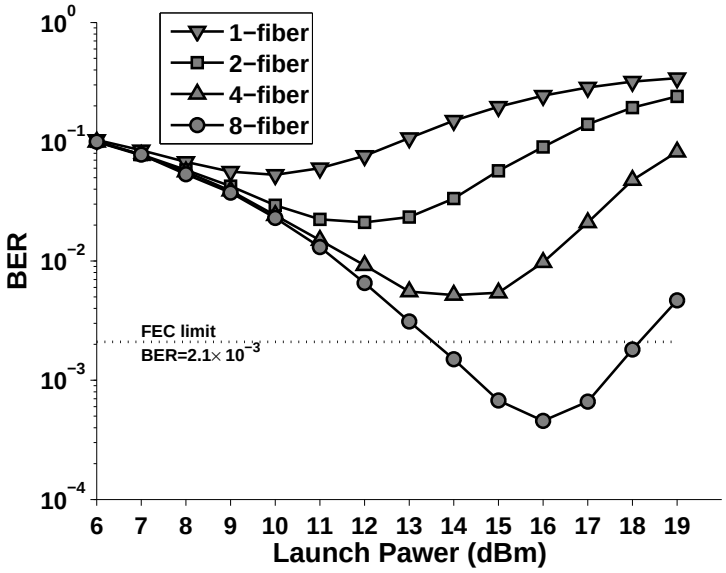

Figure 5.11: BER vs. Launch Power for 300 km unrepeatered fiber with optical equalizer (QPSK modulation).

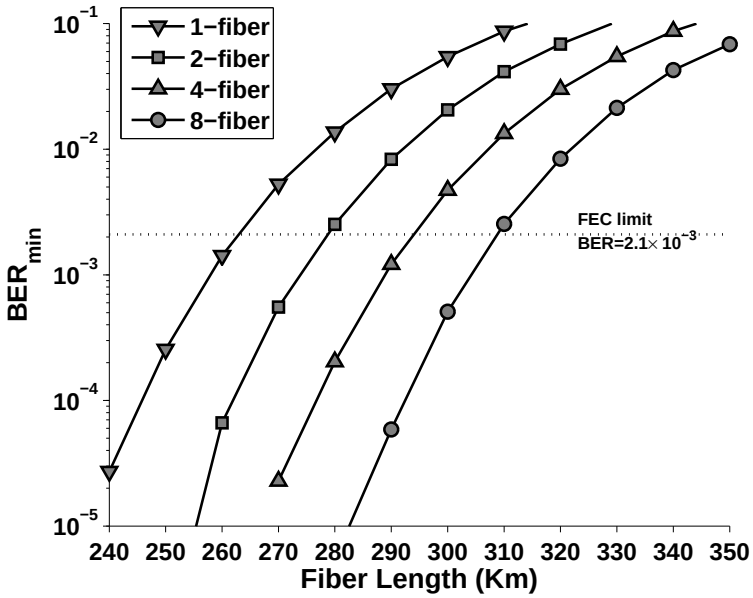

Figure 5.12: BER_{min} vs. Transmission Distance for unrepeatered fiber with optical equalizer (QPSK modulation).

degradation which leads to poorer performance of multi-core/fiber system compared to single-core fiber system.

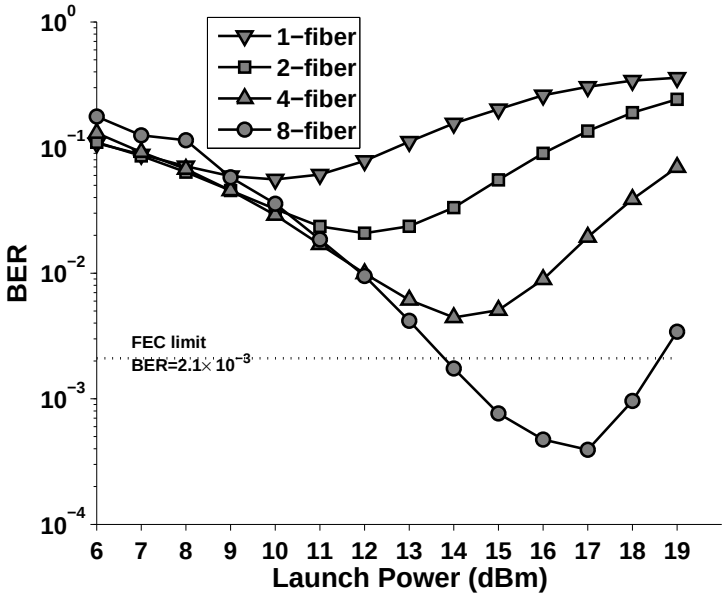

Figure 5.13: BER vs. Launch Power for 300 km unrepeatered fiber with electrical equalizer (QPSK modulation).

5.4.3 Case 3: multi-span fiber system with in-line optical equalizers

Fig. 5.14 shows the BER versus the fiber launch power for multi-span fiber system with in-line optical equalizers. In this case, transmission line consists of 5 spans of 80 km multi-fiber/multi-core fiber. 64-QAM is used for each subcarrier of OFDM system. While power is divided between multiple cores/fibers, nonlinear impairments caused by each core/fiber are reduced which leads to performance improvement. It can be seen that the optimum launch power increases as number of cores/fibers increases. The performance improvement (Q-factor) using 8-core/fiber configuration is about 5.3

dBQ_{20} as compared to single-core fiber configuration. Fig. 5.15 shows the minimum BER versus transmission distance (number of spans). Length of each span is 80 km. As can be seen, the transmission distance is limited to 240 km (three spans) using single-core fiber configuration which can be extended to 960 km (twelve spans) using 8-core/fiber configuration.

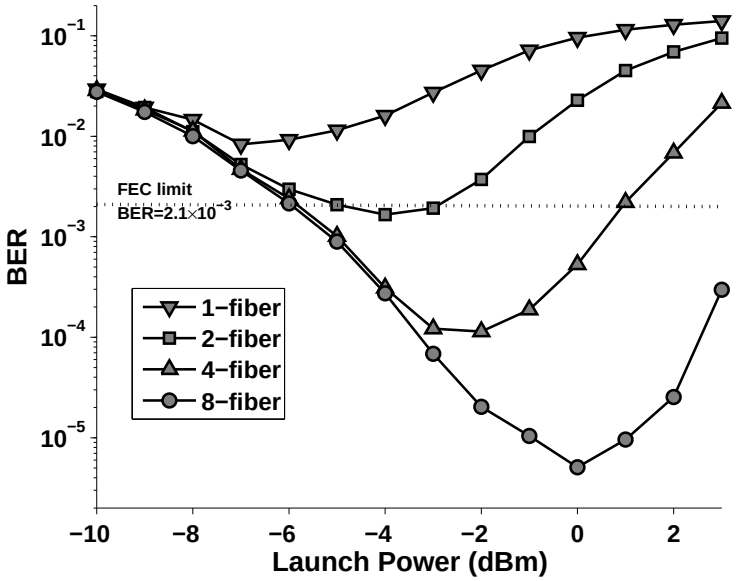

Figure 5.14: BER vs. Launch Power after 5 spans (400 km) with in-line optical equalizer (64-QAM).

5.4.4 Case 4: multi-span fiber system with optical equalizers at the receiver

Fig. 5.16 shows the BER versus the fiber launch power for multi-span fiber system with optical equalizers at the receiver. As in the previous case, transmission line consists of 5 spans of 80 km multi-fiber/multi-core fiber. 64-QAM is used for each

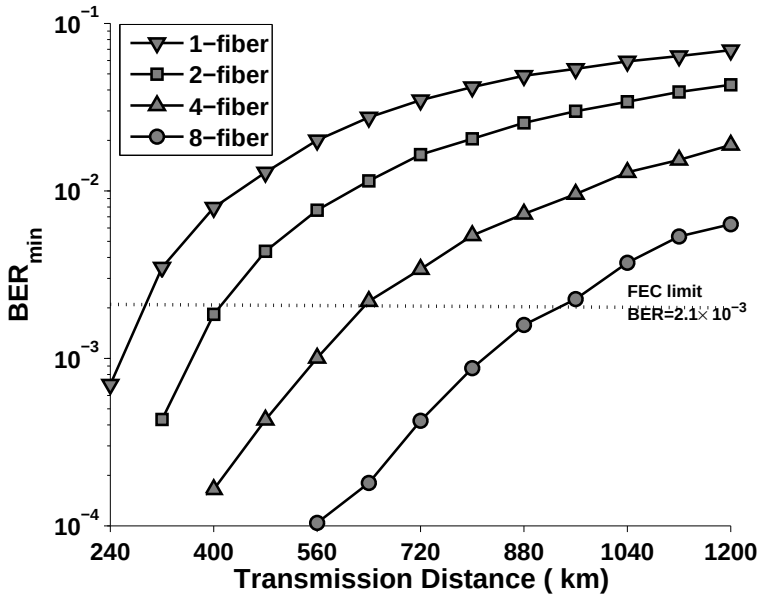

Figure 5.15: BER_{min} vs. Transmission Distance for multi-span fiber system with in-line optical equalizer (64-QAM).

subcarrier of OFDM system. As expected, the system performance is the same as case 3.

5.4.5 Case 5: effect of PMD

So far, the polarization effect was ignored. In this section, we consider the impact of PMD. Fig. 5.17 shows the BER versus the fiber launch power when system of Fig. 5.9 was used. Transmission line consists of 5 spans of 80 km multi-fiber/multi-core fiber. 64-QAM is used for each subcarrier of OFDM system. The vector NLSE is solved taking into account the PMD. For Fig. 5.17, the PMD parameter $D_p = 0.1$ ps$(\text{km})^{-1/2}$ and $z_h = 200$ m. Fig. 5.17 is obtained by taking the average BER of 10 independent runs. It can be seen that when phase shifts due to polarization effects are compensated by adaptive phase shifters, the system performance is similar to

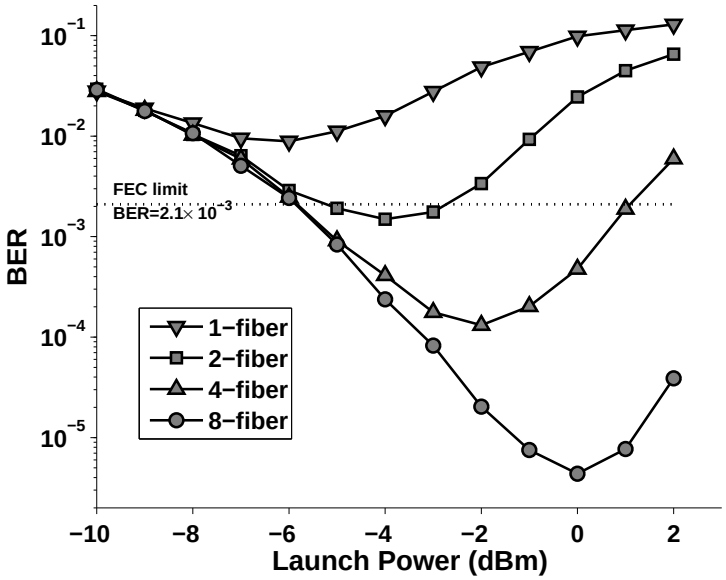

Figure 5.16: BER vs. Launch Power after 5 spans (400 km) with optical equalizer at the receiver (64-QAM).

that of case 3 or 4. In fact, in some cases, the performance is slightly better in Fig. 5.17 as compared to Fig. 5.16 (for example 2-core/fiber and 4-core/fiber cases). This is because the optical signal is divided into two orthogonal polarizations and the nonlinear coupling between the two is smaller (as compared to co-polarized case) due to the factor 2/3 appearing in Eqs. (5.7) and (5.8). As the PMD parameter increases, the walk-off between $x-$ and $y-$ polarization components increases and one may expect that the scheme of Fig. 5.9 will not work as the temporal shifts of $x-$ and $y-$ polarization components in each fiber are not adjusted. To see the impact of the PMD parameter, we carried out the simulation by changing the PMD parameter from 0.05 ps$(\text{km})^{-1/2}$ to 1 ps$(\text{km})^{-1/2}$ and the results are shown in Fig. 5.18. The parameters of Fig. 5.18 are same as that of Fig. 5.17 except for D_p. For the cases of 2-core/fiber and 4-core/fiber systems, the launch powers are -3 dBm and -1

dBm, respectively, which are optimum powers. For the case of 8-core/fiber system, we chose a lower power of -3 dBm since at the optimum power (1 dBm), it takes too much computational time. As can be seen from Fig. 5.18, the performance is not affected by PMD. This is because the one-tap equalizer in the electrical domain compensates for PMD. In addition, the delays between $x-$ and $y-$ polarization components are much smaller than the mean group delays between fibers. In the scheme of Fig. 5.9, the mean group delays are adjusted by using the adjustable time shifters, but the time shifts between $x-$ and $y-$ polarization components occurring due to the PMD is not adjusted. We have found that the power loss at the power combiner is less than 0.1 dB when D_p is 1 ps(km)$^{-1/2}$. However, for the large value of D_p and/or longer transmission distance, it may be necessary to adjust the temporal shifts of the $x-$ and $y-$ polarization components before the power combiners.

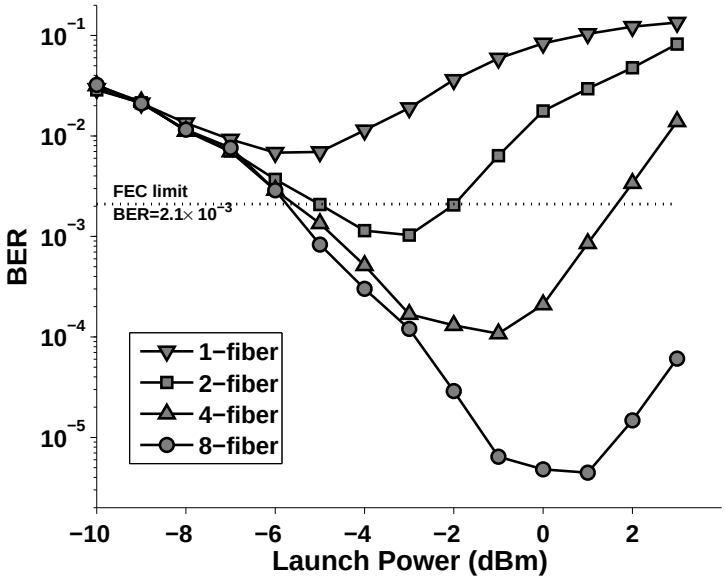

Figure 5.17: BER vs. Launch Power after 5 spans (400 km) with optical equalizer (64-QAM).

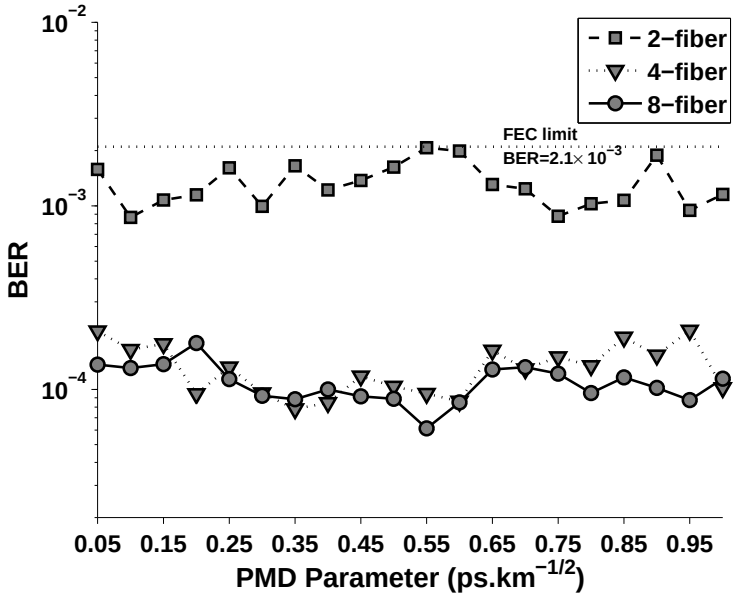

Figure 5.18: BER vs. PMD parameter after 5 spans (400 km) with optical equalizer (64-QAM).

5.5 Conclusions

We have proposed a multi-core/fiber system configuration for mitigation of fiber nonlinearities. The optical signals propagating in different fibers experience different amounts of phase shifts and timing delays leading to performance degradation. Optical and electrical equalization techniques are proposed to mitigate these impairments. Multi-core/fiber system with adaptive phase-shifters/time-shifters provides significant benefits compared to single-core system. For unrepeatered systems, the performance (Q factor) is improved by 6.2 dBQ_{20} using 8-core/fiber configuration as compared to single-core fiber system and the transmission reach increased from 260 km in the case of single-core system to 310 km in the case of 8-core/fiber system. In addition, for multi-span system, the transmission reach at a bit error ratio (BER) of 2.1×10^{-3} is quadrupled in 8-core/fiber configuration and Q factor improved by 5.3 dBQ_{20} as

compared to the single-core fiber system.

Chapter 6

A multi-core or multi-fiber WDM system

6.1 Introduction

The multi-core fibers with each core resembling the standard single-mode fiber can be fabricated with negligible cross-talk between the signals in the neighboring cores [64]. Recently, there has been a significant interest in using multi-core fiber systems to increase the system capacity [9–12, 48, 49]. In a fiber optic system, the performance degradations occur at large launch powers due to intra- and inter-channel nonlinear impairments. In a wavelength division multiplexing (WDM) system, inter-channel nonlinear impairments such as cross-phase modulation (XPM) and four wave mixing (FWM) scale directly with channel spacing and channel launch power (see Chapter 4). In Ref. [65], it is shown that interchannel nonlinear impairments can be significantly suppressed by time-interleaving the two polarizations of polarization-division-multiplexed single fiber system. In Ref. [66], propagation characteristics

of seven-core fiber for spatial and wavelength division multiplexing are evaluated. The wavelengths of the signals into the center core and those into the outer cores were interleaved. However, the propose of interleaving is not to mitigate nonlinear impairments as the transmission distance is only 5 km and launch power is around 1.5 dBm/core, and therefore there is negligible nonlinear impairments in the system studied in Ref. [66].

Based on simulation results in Chapter 4, we know that nonlinear distortion effect decreases dramatically by increasing the channel spacing (see Fig. 4.10). In this chapter, it is proposed to use multiple fiber or multi-core architecture in a WDM system in order to increase the channel spacing and decrease the input launch power. The optical wavelengths are interleaved among M fibers or M cores so that the total power launched to each fiber or core is reduced. In addition, channel spacing increases with a factor of M which leads to significant reduction in inter-channel nonlinear impairments (Fig. 4.10). Typically, the dominant contributions to the system cost comes from photonic/ optoelectronic devices such as optical amplifiers, Mach-Zehnder modulators (MZMs) and receivers and the fiber cost is a small fraction of the system cost. Therefore, in the proposed multi-core/fiber architecture, there is a slight increase in the total system cost. However, this technique leads to significant performance improvement and longer reach.

In a recent experiment, 1 petabit/s transmission over a multi-core fiber (MCF) consisting of 12 cores over a 52.4 km of fiber has been demonstrated [67]. Although this work is impressive, if extended to multi-span system, the transmission cost would increase roughly by a factor of 12 as compared to the single-core fiber since separate amplifiers are needed for each core transmission. In MCF transmission, the real

challenge is to combine all the space multiplexed and wavelength multiplexed channel through a single amplifier [9]. Fig. 6.1 shows a typical MCF system with M transmitters and M receivers. As can be seen, MCF is applied in a spatial-division multiplexing (SDM) system so that the channel capacity can be enhanced by a factor of M. Assume N-span system, total number of amplifiers is MN. In this chapter, the goal is to enhance the system reach (not the capacity) by applying MCF in WDM system while keeping the number of amplifiers same as that of in a single-core system (one amplifier per span). It is also shown that a single amplifier can be used for all the channels if the signals propagating in different cores have non overlapping spectra. Although this approach leads to a reduction in total capacity, longer transmission reach can be achieved because of the lower interchannel nonlinear impairments and it also leads to lower cost per bit because of the fewer opto-electronic/photonic devices.

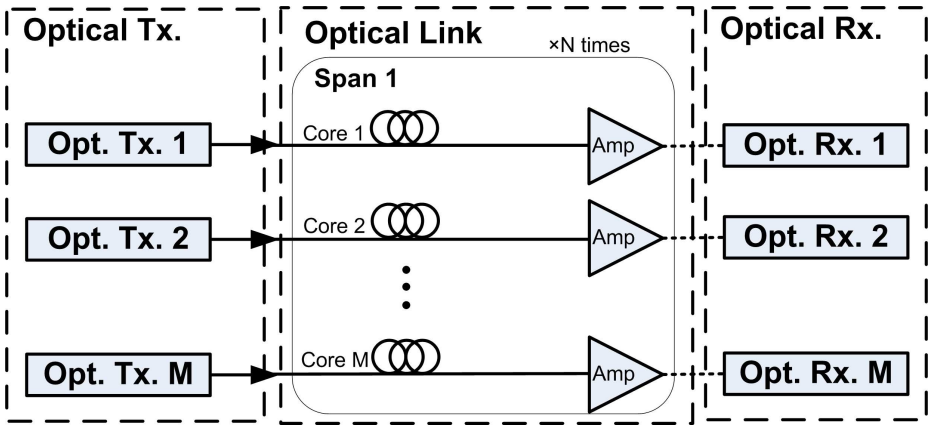

Figure 6.1: Block diagram of a typical MCF system, Amp. = amplifier.

This chapter is organized as follows. Multi-core/fiber WDM system configuration is explained in Section 6.2. Simulation results for the proposed system are given in

Section 6.3. In addition, the effect of crosstalk is investigated in multi-core communication system in this section. At the end, in Section 6.4, the contributions of this chapter are summarized.

6.2 Multi-core or multi-fiber WDM System Configuration

Fig. 6.2 displays the block diagram of a multi-core or multi-fiber WDM system. Assume R channels and M cores or fibers. The optical interleaver (IL) combines the channels $m, m+M, m+2M, ..., (R-M)+m$, $m = 1, 2, ..., M$ and this signal is launched to core/fiber m. For example, when $M = 2$, this corresponds to separating even and odd channels. The advantage of this approach is that the total launch power in a core/fiber is reduced by a factor M which helps to mitigate the inter-channel nonlinear impairments. Fig. 6.3 shows the input spectra of 12 WDM channels for the single-core and 2-core/fiber system, respectively. As can be seen, channel spacing is doubled compared to single-core system when 2-core/fiber system is used. Fig. 6.4 shows the input spectra of 12 WDM channels for the 4-core/fiber system. In this case, the channel spacing is quadrupled compared to single-core system. Just before the optical amplifier, the core/fiber outputs are combined so that a single amplifier can be used to amplify all the channels. The output of the amplifier is interleaved in the same way as done at the transmitter and is launched to M-core/fiber.

In Chapter 5 [46, 68], transmission performance of an optical orthogonal frequency division multiplexing (OOFDM) in a multi-core/fiber is investigated. Since the optical signals propagating in different cores/fibers undergo different amounts of phase shifts

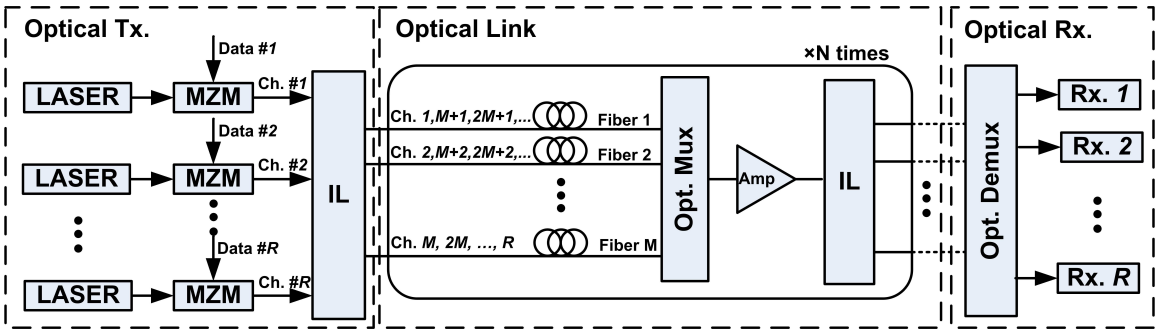

Figure 6.2: Block diagram of multi-core/fiber WDM system, MZM = Mach-Zehnder modulator, IL = interleaver, Amp. = amplifier.

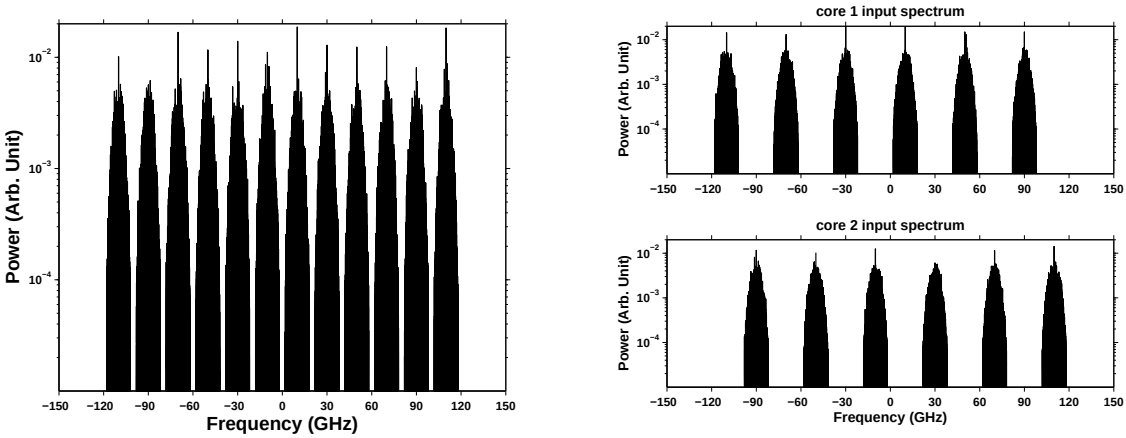

Figure 6.3: Input spectrum for single-core fiber system (left figure) and 2-core/fiber system (right figure).

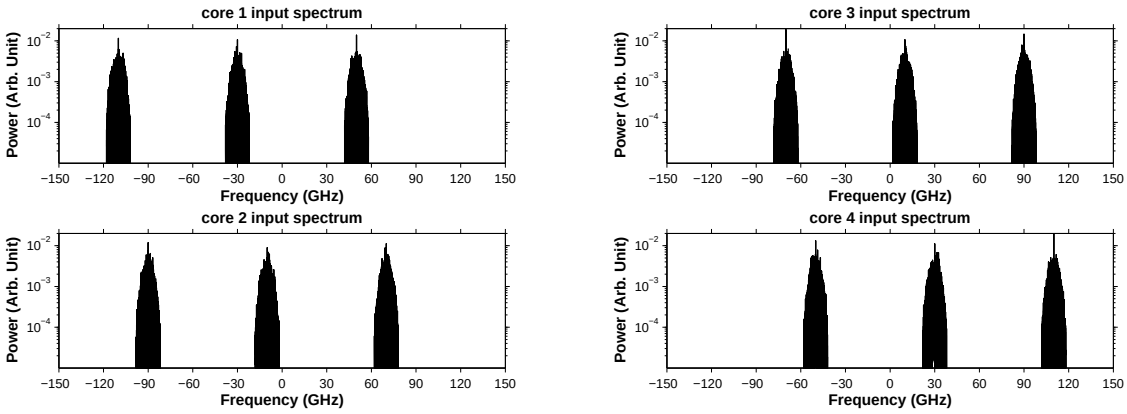

Figure 6.4: Input spectrum for 4-core/fiber system.

and timing delays, adjustable phase-shifters and timing delay lines are used in [46, 68] to align the phases and timing delays of the cores/fiber outputs. In contrast, in the proposed scheme, adjustable phase shifters and timing delay lines are not required as the signal spectra at the fiber outputs are non-overlapping and a passive multiplexer could be used to combine the fiber outputs. So, propagation constant (β_0) fluctuations and inverse group speed (β_1) fluctuations do not have any effect on the performance of the system.

As can be seen in Fig. 6.2, multi-core/fiber WDM system can be obtained by a simple modification of the conventional WDM system. Transmitters, receivers, and amplifiers are the same as conventional WDM system. However, optical multiplexers and demultiplexers are added at the end of each span. Under this condition, transmitter and receiver cost is the same as that of conventional WDM system, but the inter-channel nonlinear impairments could be significantly lower.

6.3 Simulation results

In this section, we present simulation results for the proposed system. We carried out the numerical simulation of the multi-core/fiber WDM configuration using the split-step Fourier method with the following fiber parameters: fiber loss, $\alpha = 0.2$ dB/km, fiber dispersion $\beta_2 = -22.1$ ps^2/km, and nonlinear coefficient $\gamma = 1.1$ (W.km)$^{-1}$.

For our simulation, we used 16-ary quadrature amplitude modulation (16-QAM). However, as the goal is to mitigate inter-channel nonlinearity by dividing channels between different cores or fibers, any kind of modulation techniques can be used. Raised-cosine pulses in time domain were used in each channel. To suppress the spectral side lobes, a low pass filter (LPF) with 3 dB band width of 16 GHz was

applied for each channel. Twelve channels with symbol rate of 10 Gbaud and channel spacing of 17 GHz were used. A pseudo-random bit sequence (PRBS) of length $2^{14}-1$ is used. The linewidths of transmitter and local oscillator (LO) lasers are assumed to be 100 kHz.

EDFA with a noise figure of 4.8 dB were used at the end of each 80 km fiber span to compensate the loss of fiber (Fig. 6.2). At the receiver side, digital back-propagation (DBP) with step size of 1 km was used to compensate the effect of fiber channel [69, 70]. DBP solves the nonlinear Schrodinger equation (NLSE) with the signs of dispersion parameter, loss, and nonlinear coefficients being opposite of the transmission fiber. In our simulation setup, the DBP fully compensates the intrachannel nonlinear impairments, but it does not compensate the inter-channel nonlinear impairments. We ignored the polarization effects for simplicity. However, similar results are expected when the vector NLSE are solved. The simulation results are as follows.

Fig. 6.5 shows the the constellation diagram for the channel 6 at transmission distance of 3120 km and input power of -5 dBm per channel for single-core system and -2 dBm per channel for single-core, 2-core/fiber, and 4-core/fiber systems. It can be seen that with the increase of number of cores/fibers, the spread of the constellation decreases.

Fig. 6.6 shows the average bit error ratio (BER) of all the channels in a single-core fiber system versus the launch power for different numbers of span. This BER is obtained by taking the average of the BER of all the channels. Each span consists of 80 km single-core fiber. As can be seen, the maximum reach at a BER of 2.1×10^{-3} is 33 spans (2640 km).

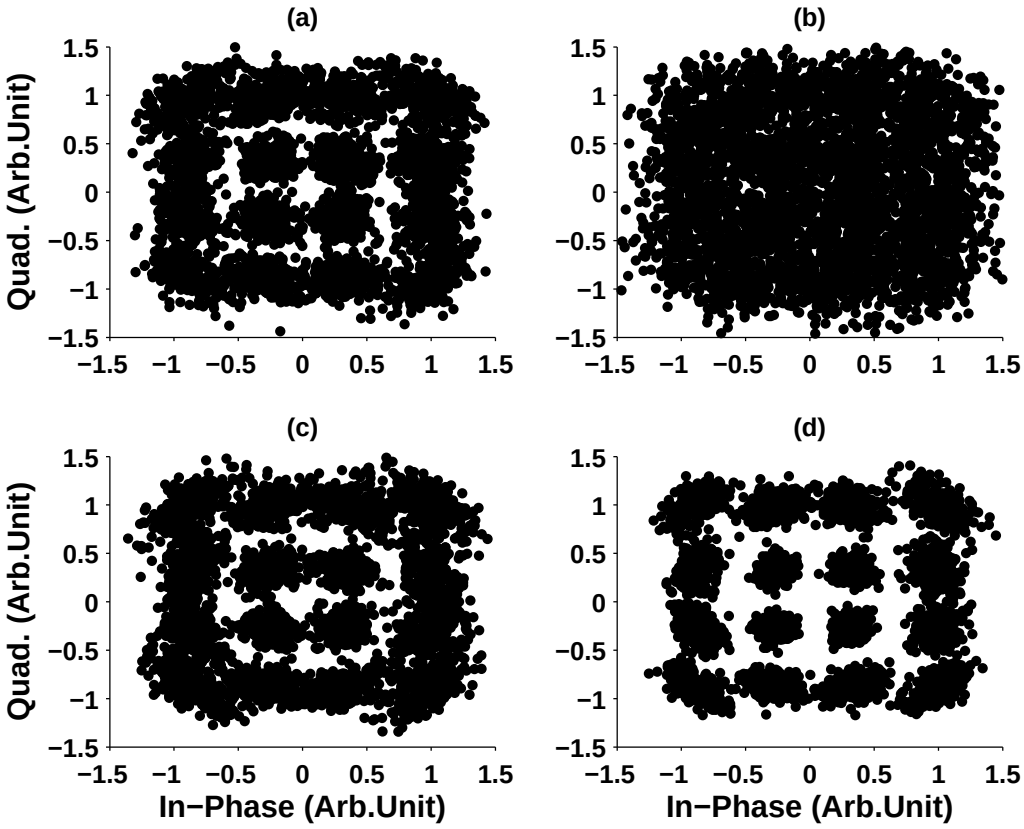

Figure 6.5: Constellation diagram for channel 6 after 39 spans (3120 km) for (a) single-core fiber system and input power of −5 dBm per channel, (b) single-core fiber system and input power of −2 dBm per channel, (c) 2-core/fiber system and input power of −2 dBm per channel, and (d) 4-core/fiber system and input power of −2 dBm per channel.

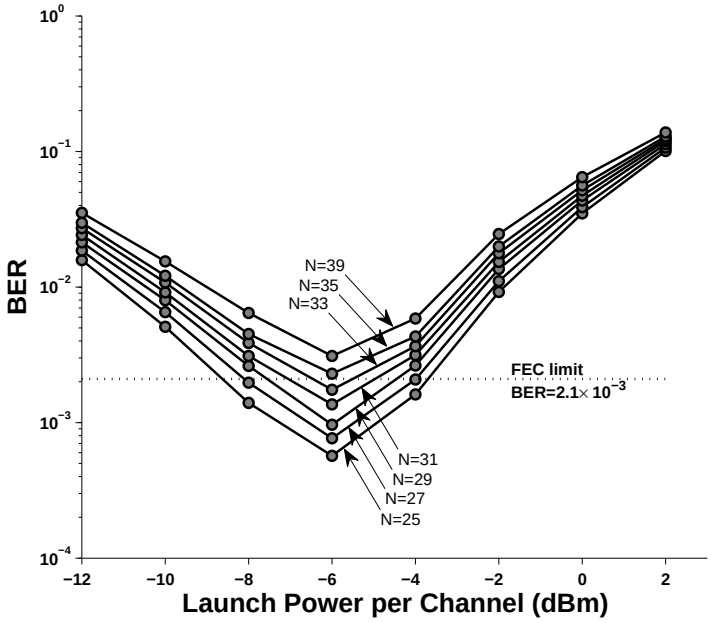

Figure 6.6: Average BER vs. launch power per channel for a single-core fiber system for different number of spans, N = number of spans.

Figs. 6.7 and 6.8 show the average BER versus the launch power for 2-core/fiber system and 4-core/fiber system, respectively. In the case of 2-core/fiber system, each fiber carries 6 optical channels. In this case, the channel spacing is doubled compared to single-core fiber system which leads to less inter-channel nonlinear impairments and longer reach (Fig. 6.7). As can be seen in Fig. 6.7, transmission distance can be extended to 47 spans (3760 km). In the case of 4-core/fiber system, each fiber carries 3 WDM channels. Channel spacing is quadrupled compared to single-core fiber system and transmission reach is extended to 67 spans (5360 km) as can be seen in Fig. 6.8. As can be seen in Figs. 6.7 and 6.8, with the increase of number of cores or fibers, optimum power shifts from -6 dBm for a single-core fiber to -4 dBm for a 2-core/fiber system and to -2 dBm for a 4-core/fiber system which shows nonlinear

impairments are lowered in a multi-core/fiber system. Adding more channels (> 3) in the 4-core system did not change the BER as the channel spacing is large. Fig. 6.9 shows the minimum BER versus the transmission reach for single-core, 2-core/fiber, and 4-core/fiber systems. From Fig. 6.9, we see that the transmission reach can be doubled by using a 4-core/fiber system as compared to single-core system.

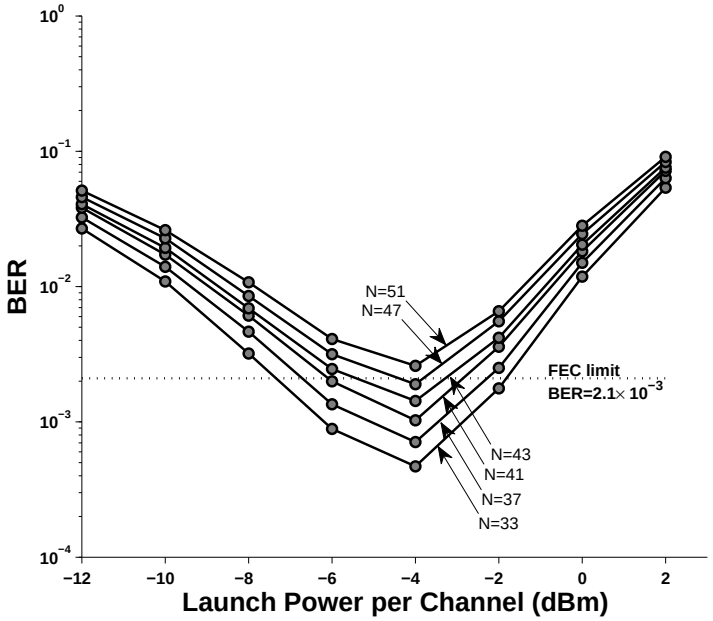

Figure 6.7: Average BER vs. launch power per channel for a 2-core/fiber system for different number of spans, N = number of spans.

6.3.1 Inter-core crosstalk effect

So far, we had ignored the inter-core crosstalk effect in MCF. However, one of the most important issues of MCF is the inter-core crosstalk. In this section, we study the sensitivity of multi-core WDM system to the inter-core crosstalk effect. For our simulation, we assumed the MCF configuration shown in Fig. 6.10 for 2-core

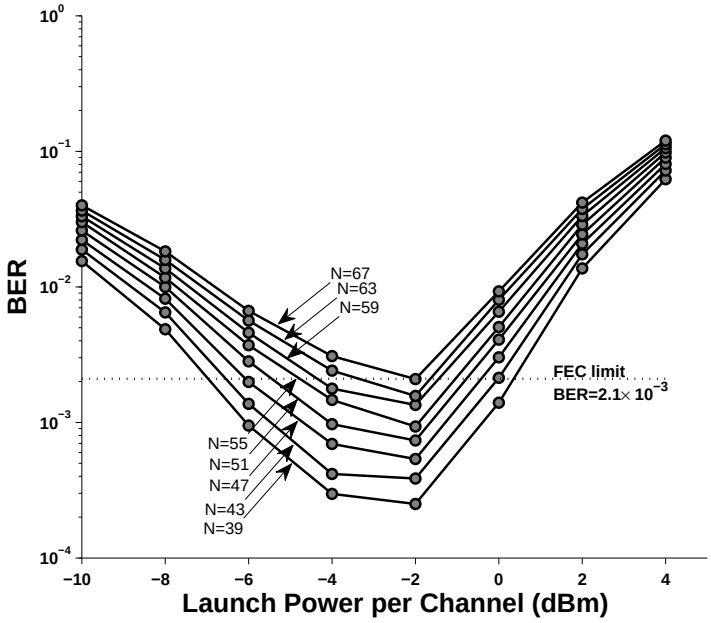

Figure 6.8: Average BER vs. launch power per channel for a 4-core/fiber system for different number of spans, N = number of spans.

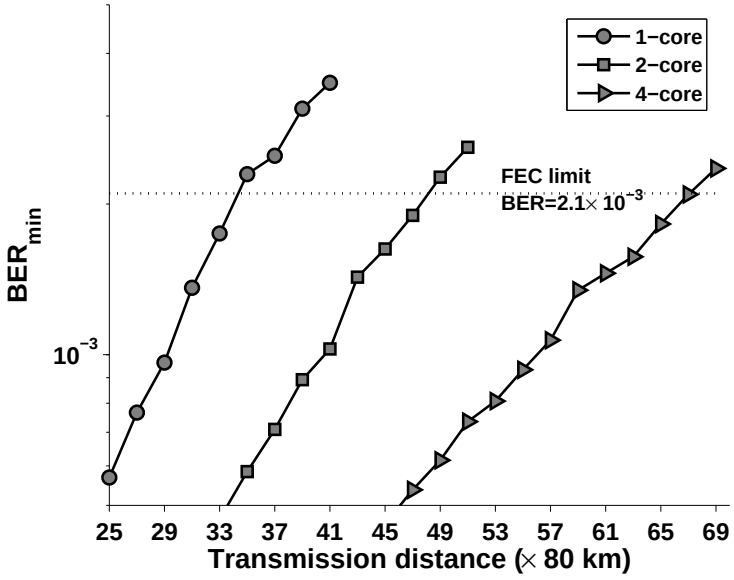

Figure 6.9: BER_{min} vs. transmission distance for single-core, 2-core/fiber, and 4-core/fiber systems.

and 4-core systems. Here, the crosstalk factor is the average crosstalk between two neighboring cores in a 80km-span, defined as

$$\text{crosstalk(dB)} = 10\log_{10}\frac{P_{\text{xtalk}}}{P_s}, \tag{6.1}$$

where P_{xtalk} is the crosstalk power due to a single neighboring core and P_s is the signal power in the core. As well as the linear crosstalk, there is a nonlinear crosstalk

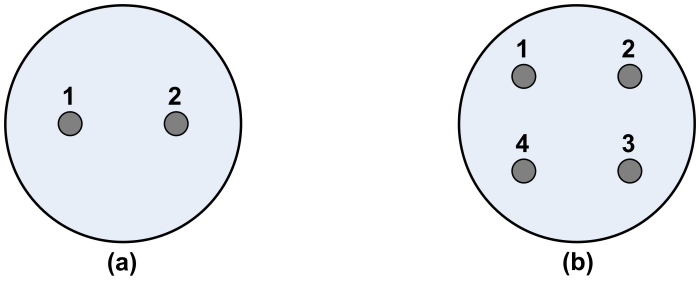

Figure 6.10: A cross section of (a) 2-core fiber, and (b) 4-core fiber.

between the cores due to the spatially overlapping of the propagating modes' fields in the neighboring cores. To take into account the nonlinear crosstalk between the cores, an extra term due to the nonlinear inter-core crosstalk is added to the nonlinear Schrodinger equation (NLSE),

$$\frac{\partial q_1(t,z)}{\partial z}+i\frac{\beta_2}{2}\frac{\partial^2 q_1(t,z)}{\partial t^2} = \left[i\gamma_{11}|q_1(t,z)|^2 + i2\gamma_{12}|q_2(t,z)|^2 - \frac{\alpha}{2}\right] q_1(t,z), \tag{6.2}$$

$$\gamma_{11} = \frac{n_2\omega_0}{cA_{\text{eff},11}}, \tag{6.3}$$

$$\gamma_{12} = \frac{n_2\omega_0}{cA_{\text{eff},12}}, \tag{6.4}$$

$$A_{\text{eff},11} = \frac{\int\int |F_{11}(x,y)|^2\, dxdy}{\int\int |F_{11}(x,y)|^4\, dxdy}, \tag{6.5}$$

$$A_{\text{eff},12} = \frac{\int\int |F_{11}(x,y)|^2 \, dxdy}{\int\int |F_{11}(x,y)|^2 \, |F_{22}(x,y)|^2 \, dxdy}, \tag{6.6}$$

where γ_{11} is the intracore nonlinear coefficient, γ_{12} is the inter-core nonlinear coefficient, n_2 is the nonlinear-index coefficient, ω_0 is the carrier frequency, c is the speed of light, $A_{\text{eff},11}$ is the effective mode area for core 1, $A_{\text{eff},12}$ is the effective overlapping modes area between cores 1 and 2, and $F_{11}(x,y)$ and $F_{22}(x,y)$ are the fundamental modes modal distributions for core 1 and core 2, respectively. For the assumed core spacing (15 μm), γ_{12} is much smaller than γ_{11} so that nonlinear crosstalk does not affect the system performance significantly. So, the nonlinear crosstalk is ignored in the simulation. We assume two types of multiplexer: (1) non-frequency selective multiplexer, and (2) frequency-selective multiplexer.

Non-frequency selective multiplexer

Assume 4 WDM channels (λ_1, λ_2, λ_3, and λ_4,) and 2 cores. The interleaver launches channels 1 and 3 (λ_1, λ_3) to core 1 and channels 2 and 4 (λ_2, λ_4) to core 2. Due to the linear crosstalk, a portion of power from core 1 couples into core 2 ($\delta\lambda_1$, and $\delta\lambda_3$) and vice versa ($\delta\lambda_2$, and $\delta\lambda_4$). Fig. 6.11 shows the output of the cores and the block diagram of the non-frequency selective multiplexer. As can be seen, at the core 1 (core 2) output, two WDM channels λ_1 and λ_3 (λ_2 and λ_4) and the crosstalk distortions $\delta\lambda_2$ and $\delta\lambda_4$ ($\delta\lambda_1$ and $\delta\lambda_3$) are present. In this case, multiplexer simply adds the cores' outputs together. So, we have $\sum_{i=1}^{4} \lambda_i + \delta\lambda_i$ at the output of the multiplexer. Since $\delta\lambda_i$ is in the same frequency as that of λ_i with different amount of phase shift, it acts like a noise for the WDM channel λ_i which leads to performance degredation.

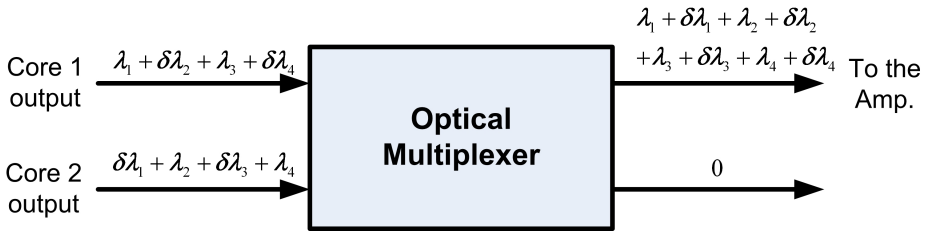

Figure 6.11: Non-frequency selective multiplexer block diagram.

Figs. 6.12(a) and 6.12(b) show the average BER versus crosstalk factor for 2-core and 4-core systems, respectively. It can be seen that with the increase of crosstalk, performance of MCF system decreases. From Fig. 6.12(a) (6.12(b)), we see that when the crosstalk exceeds -32 dB, (-34 dB), the performance of 2-core (4-core) MCF system is worse than that of a single-core system. Performance penalties at crosstalk factor -30 dB are 1.55 dBQ_{20} and 3.25 dBQ_{20} for 2-core and 4-core systems, respectively, when they are compared to crosstalk factor -55 dB.

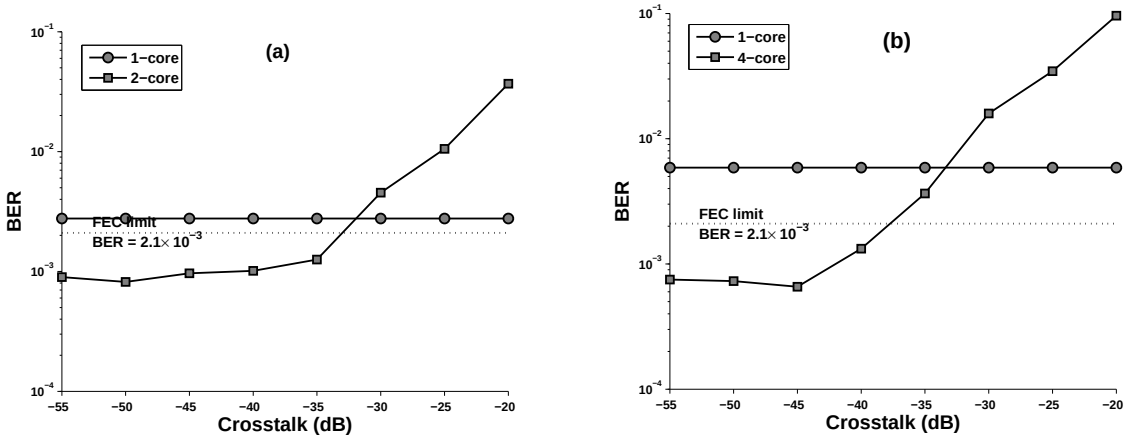

Figure 6.12: Average BER vs. crosstalk factor for (a) 1-core and 2-core fiber, No. of spans = 37, $P_{in} = -6$ dBm for the 1-core, $P_{in} = -4$ dBm for 2-core, (b) 1-core and 4-core fiber, No. of spans = 47, $P_{in} = -6$ dBm for the 1-core, $P_{in} = -2$ dBm for 4-core.

Frequency-selective multiplexer

Since the crosstalk distortions ($\delta\lambda_i$) are spatially and spectrally separated (they are in different cores and different frequencies), the multiplexer transfer function can be designed such that it eliminates the distortions. Fig. 6.13 shows the frequency-selective multiplexer block diagram. As can be seen, the multiplexer picks wavelengths λ_1 and λ_3 from core 1 output and λ_2 and λ_4 from core 2 output. The crosstalk distortions ($\delta\lambda_i$) appear in the other port of the multiplexer and they do not affect the system performance, except for the fact that the power loss due to leaking lowers the SNR.

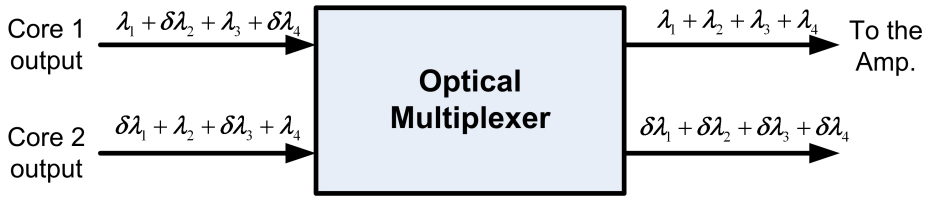

Figure 6.13: Frequency selective multiplexer block diagram.

Fig. 6.14 shows the average BER versus crosstalk factor for 2-core and 4-core systems. In the 2-core system, $P_{in} = -4$ dBm and 37 spans were assumed and in the 4-core system, $P_{in} = -2$ dBm and 47 spans were assumed. It can be seen that the system shows better tolerance to the crosstalk effect compared to the non-frequency-selective multiplexer case. From Fig. 6.14, we see that when the crosstalk exceeds -15 dB, the performance of multi-core system begins to decrease which is due to the power loss caused by crosstalk effect.

The way in which the discussed multiplexers can be built have not been studied yet and it has been left as a future work. It is worth mentioning that the proposed multi-core WDM system has better tolerance to the inter-core crosstalk effect compared to

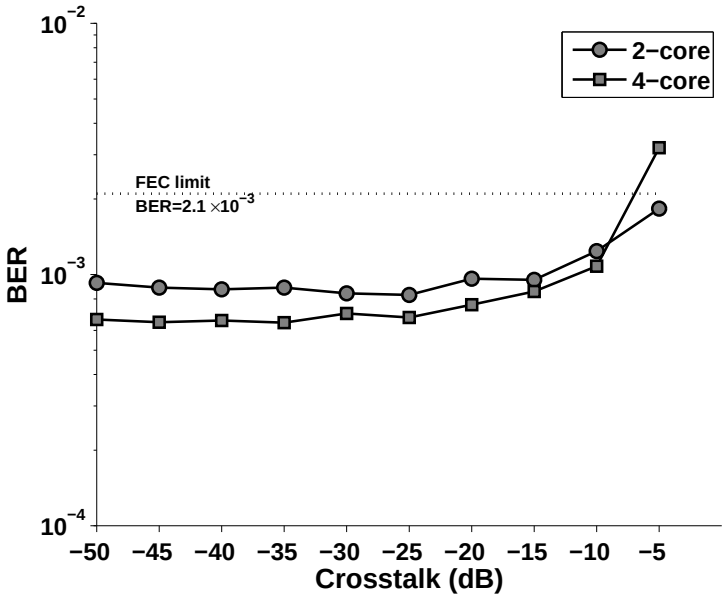

Figure 6.14: Average BER vs. crosstalk factor for (1) 2-core fiber, No. of spans = 37, $P_{in} = -4$ dBm, (2) 4-core fiber, No. of spans = 47, $P_{in} = -2$ dBm.

conventional multi-core WDM systems that uses a separate amplifier for each core (Fig. 6.1). It is due to the fact that channels propagating in each core have no correlation with channels propagating in the neighboring cores in frequency domain (Figs. 6.3 and 6.4). In contrast, in the multi-core WDM system that uses a separate amplifier for each core, inter-core crosstalk effect increases with transmission distance causing serious performance degradation.

6.4 Conclusions

In this chapter, we have proposed a multiple core or multi-fiber system configuration for a WDM system in order to mitigate the inter-channel fiber nonlinearity. Unlike the single channel multi-core/fiber (Chapter 5), multi-core/fiber WDM system does

not require adaptive phase-shifters and time-shifters which makes the system easy to implement. By decreasing the inter-channel nonlinear impairments, transmission reach can be extended from 2640 km for a single-core fiber system to 5360 km for a 4-core/fiber system with negligible crosstalk. Effect of crosstalk for two different multiplexers are studied and it is shown that the multiplexer can be designed such that it blocks the crosstalk distortions.

Chapter 7

Conclusions and future work

This thesis is focused on the analysis and mitigation of nonlinear impairments in the fiber-optic system. In the first part (Chapters 2, 3, and 4), analytical models for the single channel nonlinear distortion (intrachannel) and multi-channel nonlinear distortion (inter-channel) are developed. Then, in the second part (Chapters 5, and 6), multi-core/fiber architecture is proposed to mitigate the intrachannel and inter-channel nonlinear impairments.

In Chapter 2, an analytical expression for the intrachannel nonlinear impairments is developed based on QPSK modulation. Based on the analytical model, power spectral density (PSD) and variance due to the nonlinear distortions are obtained. It is found that intrachannel four-wave mixing (IFWM) is the only source of nonlinear distortion for the QPSK system. The IFWM variance is added to that of amplified spontaneous emission (ASE) noise to obtain the total variance so that the BER can be found analytically. Simulation results show that the analytical model is in good agreement with the numerical results. Using the analytical model, computational cost can be reduced significantly compared to Monte-Carlo simulations. For non-Gaussian

pulses, the nonlinear impairments can not be obtained analytically. However, using stationary phase approximation, convolutions are replaced by simple multiplications and a closed-form formula can be obtained. The analytical model (and also numerical results) shows that the nonlinear impairment scales as P^3 where P is the fiber input launch power. This fact is used in Chapters 5 and 6 to decrease the nonlinear effects.

In Chapter 3, the same approach as Chapter 2 is used to find the intrachannel nonlinear impairments for QAM signal. In this case, the PSD due to the self-phase modulation (SPM), intrachannel cross-phase modulation (IXPM), IFWM, and correlation between them are obtained analytically. It is found that the IXPM has the main contribution to the total PSD which suggests that a computationally inexpensive equalizer can be designed such that it only compensates for the IXPM. Design of such an equalizer is left for the future work. As an another future work, the analytical variances can be used to find the BER of a QAM system analytically.

In Chapter 4, an analytical model is developed for the inter-channel nonlinear impairments based on QAM signal. Using the model, variances for SPM and cross-phase modulation (XPM) nonlinear distortions are obtained analytically. Same as for intrachannel nonlinear variance, inter-channel nonlinear variance scales as P^3. In addition, a linear relation between the nonlinear impairment variance and the system reach is found which helps reducing the computational cost by extrapolating the carve when the slope of the line is known. As a future work, analytical BER in the WDM systems can be obtained using the model.

In Chapter 5, a multi-core/fiber system is proposed to mitigate the fiber nonlinear impairments. Since the nonlinear impairments scales as P^3, reduction of input

launch power by dividing the power between the cores/fibers leads to significant system performance improvement. Signals in different cores/fibers experience different amount of phase shifts and timing delays which causes power loss when they are combined at the power combiner. So, electrical and optical equalizers are used to make sure all signals are added in phase. Four different systems are assumed: (1) unrepeatered multi-core/fiber system with optical equalizer, (2) unrepeatered multi-core/fiber system with electrical equalizer, (3) multi-span multi-core/fiber system with in-line optical equalizers, and (4) multi-span multi-core/fiber system with optical equalizers at the receiver. For unrepeatered systems, the performance is improved by 6.2 dBQ_{20} using 8-core/fiber configuration as compared to single-core fiber system and the transmission reach increased from 260 km in the case of single-core system to 310 km in the case of 8-core/fiber system. For multi-span system, the transmission reach is quadrupled in 8-core/fiber configuration and Q factor improved by 5.3 dBQ_{20} as compared to single-core fiber system.

In Chapter 6, the multi-core/fiber system is applied in WDM systems to decrease the inter-channel nonlinear impairments. Since each core/fiber carries channels with different frequencies, adaptive phase and time shifters are not required in this system. In each core/fiber, channel spacing increases and input launch power decreases by a factor of M (M is the number of cores/fibers) by interleaving the WDM channels between M cores/fibers. As a result, inter-channel impairments decrease and system performance increases significantly. It is shown that for a 39-span system, the 4-core/fiber system with negligible crosstalk outperforms the single-core system by 2.2 dBQ_{20}. In addition, transmission reach can be extended from 2640 km for a single-core fiber system to 5360 km for a 4-core/fiber system. The effect of inter-core crosstalk

is investigated for two types of multiplexers: (1) non-frequency selective multiplexer, and (2) frequency-selective multiplexer. It is shown that for the frequency-selective multiplexer, transfer function of the multiplexer can be designed such that it blocks the crosstalk distortions. The way in which these multiplexers can be built is left as a future work.

Appendix A

Gaussian pulse case

For a Gaussian pulse shape, we have

$$p(t,0) = \exp\left(-\frac{t^2}{2T_0^2}\right), \tag{A.1}$$

and

$$\tilde{p}(f,0) = k\exp(-\xi f^2), \tag{A.2}$$

where

$$\begin{aligned} k &= \sqrt{2\pi}T_0, \\ \xi &= 2\pi^2 T_0^2. \end{aligned} \tag{A.3}$$

Equation (2.18) can be rewritten as

$$\tilde{X}_{l,m,l+m}(f,z) = \int\int \tilde{p}_1(f_1)\exp(i2\pi f_1 l T_s)\tilde{p}_2(f_2-f_1)\exp[i2\pi(f_2-f_1)mT_s]$$

$$\tilde{p}_3(f-f_2)\exp[i2\pi(f-f_2)nT_s]df_1df_2, \tag{A.4}$$

$$n = l + m, \tag{A.5}$$

$$\tilde{p}_1(f) = \tilde{p}(f,z) = \tilde{p}(f,0)\exp[i(2\pi f)^2\beta_2 z/2], \tag{A.6}$$

$$\tilde{p}_2(f) = \tilde{p}_1(f), \tag{A.7}$$

$$\tilde{p}_3(f) = \tilde{p}_1^*(-f) = k\exp[-\xi f^2 - i(2\pi f^2)\beta_2 z/2]. \tag{A.8}$$

Let

$$X_{l,m,n}(f,z) = \int M(f_2)\tilde{p}_3(f-f_2)\exp[i2\pi(f-f_2)nT_s]df_2, \tag{A.9}$$

$$\begin{aligned} M(f_2) = \int \tilde{p}(f_1,0)\exp[i2\pi f_1 lT_s + i\delta f_1^2]\tilde{p}(f_2-f_1,0) \\ \exp[i2\pi(f_2-f_1)mT_s + i\delta(f_2-f_1)^2]df_1, \end{aligned} \tag{A.10}$$

where $2\pi^2\beta_2 z = \delta$. Using Eq. (A.2) in Eq. (A.10), we find

$$\begin{aligned} M(f_2) &= k^2\int \exp[-\xi f_1^2 + i\delta f_1^2 - \xi(f_2-f_1)^2 + i2\pi f_1 lT_s \\ &\quad +i2\pi(f_2-f_1)mT_S + i\delta(f_2-f_1)^2]df_1, \\ &= k^2\exp[-\xi f_2^2 + i\delta f_2^2 + i2\pi f_2 mT_s] \\ &\quad \int \exp\{-2[\xi - i\delta]f_1^2 + i2\pi f_1(l-m)T_s + 2\xi f_1 f_2 - i2\delta f_1 f_2\}df_1. \end{aligned} \tag{A.11}$$

Equation (A.11) may be rewritten as

$$M(f_2) = k^2 \exp[-(\xi - i\delta)f_2^2 + i2\pi f_2 m T_s] I(f_2), \tag{A.12}$$

where

$$\begin{aligned} I(f_2) &= \int \exp\{-2(\xi - i\delta)f_1^2 + 2f_1[i\pi(l-m)T_s + (\xi - i\delta)f_2]\} df_1, \\ &= \exp\left\{\frac{[(\xi - i\delta)f_2 + i\pi(l-m)T_s]^2}{2(\xi - i\delta)}\right\} \frac{\sqrt{\pi}}{\sqrt{2(\xi - i\delta)}}. \end{aligned} \tag{A.13}$$

Substituting Eq. (A.13) in Eq. (A.12), we find

$$M(f_2) = J \exp(-\beta f_2^2 + i\mu f_2), \tag{A.14}$$

$$J = \frac{k^2\sqrt{\pi}}{\sqrt{2(\xi - i\delta)}} \exp\left(\frac{-\pi^2(l-m)^2 T_s^2}{2(\xi - i\delta)}\right), \tag{A.15}$$

$$\beta = \frac{\xi - i\delta}{2}, \tag{A.16}$$

$$\mu = \pi T_s (l + m). \tag{A.17}$$

Substituting Eq. (A.14) in Eq. (A.9) and noting that

$$\tilde{p}_3(f - f_2) = k \exp[-(\xi + i\delta)(f - f_2)^2], \tag{A.18}$$

Eq. (A.9) becomes

$$\begin{aligned} X_{l,m,l+m} = J \exp[-(\xi + i\delta)f^2 + i2\pi f n T_s] \int \exp[-(\xi \\ -i\delta)f_2^2/2 - (\xi + i\delta)f_2^2 + (\xi + i\delta)2f f_2] df_2, \end{aligned}$$

$$= D\exp(Af^2 + Bf + C), \tag{A.19}$$

$$A = -\frac{(\xi^2 + \delta^2)f^2}{3\xi + i\delta}, \tag{A.20}$$

$$B = \frac{i4\pi f T_s(l+m)\xi}{3\xi + i\delta}, \tag{A.21}$$

$$C = -\frac{2\pi^2 T_s^2[(l^2+m^2)\xi - lm(\xi + i\delta)]}{(3\xi + i\delta)(\xi - i\delta)}, \tag{A.22}$$

$$D = \frac{k^3\pi}{\sqrt{(\xi - i\delta)(3\xi + i\delta)}}. \tag{A.23}$$

Appendix B

Stationary phase approximation

From Eq. (A.10), we have

$$M(f_2) = \int \tilde{p}(f_1,0)\tilde{p}(f_2-f_1,0)\exp\left[i2\pi f_1 l T_s + i\delta f_1^2 + i\delta(f_2-f_1)^2 + i2\pi(f_2-f_1)mT_s\right]df_1$$
$$= \exp(i2\pi f_2 mT_s + i\delta f_2^2)I(f_2), \tag{B.24}$$

$$I(f_2) = \int \tilde{p}(f_1,0)\tilde{p}(f_2-f_1,0)\exp\left[i2\delta f_1^2 + i2\pi f_1(l-m)T_s - 2i\delta f_1 f_2\right]df_1. \tag{B.25}$$

Let

$$\theta(f_1) = 2\delta f_1^2 - 2\delta f_1 f_2 + f_1 2\pi(l-m)T_s, \tag{B.26}$$

so that

$$I(f_2) = \int \tilde{p}(f_1,0)\tilde{p}(f_2-f_1,0)\exp\left(i\theta(f_1)\right)df_1. \tag{B.27}$$

We assume that $p(t)$ is real and symmetric with respect to origin so that $\tilde{p}(f)$ is real. Since $\theta(f_1)$ is varying rapidly, the dominant contribution to the integral in Eq. (B.27)

comes when

$$\frac{d\theta}{df_1} = 0, \tag{B.28}$$

or

$$f_{1,opt} = \frac{\pi(m-l)T_s}{2\delta} + \frac{f_2}{2}. \tag{B.29}$$

Substituting Eq. (B.29) in Eq. (B.26), we find

$$\theta(f_{1,opt}) = -\frac{\delta}{2}\Big[f_2 + \frac{\pi(m-l)T_s}{\delta}\Big]^2. \tag{B.30}$$

Under the stationary phase approximation, Eq. (B.27) becomes

$$I(f_2) \cong \tilde{p}(f_{1,opt}, 0)\tilde{p}(f_2 - f_{1,opt}, 0)\exp\left[i\theta(f_{1,opt})\right]l_1, \tag{B.31}$$

$$\begin{aligned} l_1 &= \sqrt{\frac{2\pi}{|\theta''(f_{1,opt})|}}\exp\left[\mathrm{sgn}(\theta''(f_{1,opt}))i\pi/4\right], \\ &= \sqrt{\frac{\pi}{2|\delta|}}\exp\left(i\mathrm{sgn}(\delta)\pi/4\right), \end{aligned} \tag{B.32}$$

where $''$ denotes differentiating twice. Using Eqs. (B.29) and (B.32) in Eq. (B.31), we find

$$\begin{aligned} I(f_2) = l_1\tilde{p}\Big(\frac{\pi(m-l)T_s + f_2\delta}{2\delta}, 0\Big)\tilde{p}\Big(\frac{\delta f_2 - \pi(m-l)T_s}{2\delta}, 0\Big) \\ \exp\Big\{-\frac{i\delta}{2}\Big[f_2 + \frac{\pi(m-l)T_s}{\delta}\Big]\Big\}. \end{aligned} \tag{B.33}$$

Substituting Eq. (B.33) in Eq. (B.24), we find

$$M(f_2) = s_1(f_2) \exp\Big[\frac{i\delta f_2^2}{2} - \frac{i\pi^2(m-l)^2T_s^2}{2\delta} + i\pi f_2(m+l)T_s\Big], \tag{B.34}$$

where

$$s_1(f_2) = \tilde{p}\Big(\frac{\pi(m-l)T_s + f_2\delta}{2\delta}, 0\Big)\tilde{p}\Big(\frac{\delta f_2 - \pi(m-l)T_s}{2\delta}, 0\Big). \tag{B.35}$$

Substituting Eq. (B.34) in Eq. (A.9) and simplifying, we obtain

$$\tilde{X}_{l,m,l+m}(f) = \exp\Big[-\frac{i\pi^2(m-l)^2T_s^2}{2\delta} - i\delta f_2\Big]\int s_2(f_2)\exp\left(i\theta_2(f_2)\right)df_2, \tag{B.36}$$

where

$$s_2(f_2) = s_1(f_2)\tilde{p}(f - f_2, 0), \tag{B.37}$$

$$\theta_2(f_2) = -\frac{\delta f_2^2}{2} + 2\delta f f_2 - \pi T_s f_2(l+m). \tag{B.38}$$

Since θ_2 is varying rapidly, we use the stationary phase approximation again to evaluate the integral in Eq. (B.36). Differentiating Eq. (B.38) with respect to f_2 and setting the result to zero yields

$$f_{2,opt} = 2f - \frac{\pi T_s(l+m)}{\delta}. \tag{B.39}$$

Proceeding as before, Eq. (B.36) can be simplified as

$$\tilde{X}_{l,m,l+m}(f) = \frac{\pi}{|\delta|}\tilde{p}\Big(f - \frac{\pi l T_s}{\delta}, 0\Big)\tilde{p}\Big(f - \frac{\pi m T_s}{\delta}, 0\Big)\tilde{p}\Big(- f + \frac{\pi(l+m)T_s}{\delta}, 0\Big) \exp\Big[i\Big(\delta f^2 + \frac{2\pi^2 T_s^2 lm}{\delta}\Big)\Big]. \tag{B.40}$$

Appendix C

Differential equation solution

Taking the Fourier transform of Eq. (4.19), we have

$$\frac{d\tilde{f}(z,\omega)}{dz} - \frac{j\omega^2\beta_2(z)}{2}\tilde{f}(z,\omega) = -j\tilde{F}(z,\omega), \tag{C.41}$$

where $\tilde{f}(z,\omega)$ is the Fourier transform of $f(z,T)$ and

$$\begin{aligned}\tilde{F}(z,\omega) &= \eta(z)\exp\left(-\sum_{k=1}^{3} C_k^2 R_k\right)\int_{-\infty}^{\infty}\exp[-RT^2 + T(2C + i\omega)]dT \\ &= \frac{\sqrt{\pi}\eta'}{\sqrt{R}}\exp\left[\frac{-\omega^2}{4R} - D\omega\right],\end{aligned} \tag{C.42}$$

where

$$R = R_1 + R_2 + R_3, \quad C = C_1R_1 + C_2R_2 + C_3R_3, \tag{C.43}$$

$$D = \frac{iC}{R}, \tag{C.44}$$

$$\eta'(z) = \eta(z)\exp\left(-\sum_{k=1}^{3} C_k^2 R_k + \frac{C^2}{R}\right). \tag{C.45}$$

The solution of Eq. (C.41) with the initial condition $\tilde{f}(0,\omega) = 0$, is

$$\tilde{f}(z,\omega) = -j \int_0^z \tilde{F}(s,\omega) \exp[j\omega^2 A(z,s)/4] ds, \tag{C.46}$$

where

$$A(z,s) = 2[S(z) - S(s)]. \tag{C.47}$$

Using Eq. (C.42) in Eq. (C.46) and inverse Fourier transforming, we obtain

$$f(z,T) = \frac{-j\sqrt{\pi}}{2\pi} \int_0^z \frac{\eta'(s)}{\sqrt{R(s)}} \int_{-\infty}^{\infty} \exp[-4\omega^2\delta - \omega(D + jT)] d\omega ds, \tag{C.48}$$

where

$$\delta(z,s) = \frac{1}{R(s)} - jA(z,s). \tag{C.49}$$

After evaluating the inner integral in Eq. (C.48), we obtain

$$f(z,T) = -j \int_0^z \frac{\eta'(s)}{\sqrt{\delta(z,s)R(s)}} \exp\left[\frac{(D(s) + jT)^2}{\delta(z,s)}\right] ds. \tag{C.50}$$

Using Eqs. (C.43)-(C.45) and Eq. (C.50), and after some algebra, we arrive at Eq. (4.21).

Bibliography

[1] G. P. Agrawal, *Fiber-Optic communication Systems*, 3rd Ed., John Wiley and Sons, Inc., New York (2002).

[2] R. Tkach, "Scaling optical communications for the next decade and beyond," *Bell Labs Tech. J.* **14**, p. 3, (2010).

[3] T. H. Maiman, "Stimulated optical radiation in ruby," *Nature* **187**, p. 493 (1960).

[4] K. C. Kao and G. A. Hockham, *Proc. IEE* **113**, p. 1151 (1966).

[5] T. Miya, Y. Terunuma, T. Hosaka, and T. Miyashita, "Ultimate low-loss single-mode fibre at 1.55 μm," *Electronics Letters* **15**, p. 106 (1979).

[6] K. Kikuchi, "Coherent optical communications: Historical perspectives and future directions," *High Spectral Density Optical Communication Technologies*, p. 11, Springer Berlin Heidelberg, (2010).

[7] R-J. Essiambre, G. Kramer, P. J. Winzer, G. J. Foschini, and B. Goebel. "Capacity limits of optical fiber networks," *J. Lightw. Technol.*, **28**, p. 662 (2010).

[8] G. Li, "Recent advances in coherent optical communication," *Advances in optics and photonics* **1**, p. 279 (2009).

[9] P. J. Winzer, "Coherent Communication (Tutorial)," IEEE Photonics Conference (IPC), Burlingame, CA, September 2012.

[10] J. Sakaguchi, Y. Awaji, Naoya Wada, A. Kanno, T. Kawanishi, T. Hayashi, T. Taru, T. Kobayashi, M. Watanabe, "109-Tb/s (7x97x172-Gb/s SDM/WDM/PDM) QPSK transmission through 16.8-km homogeneous multi-core fiber," *OFC/NFOEC Postdeadline Paper* (2011).

[11] B. Zhu, T. Taunay, M. Fishteyn, X. Liu, S. Chandrasekhar, M. Yan, J. Fini, E. Monberg, F. Dimarcello, "Space-, Wavelength-, Polarization-Division Multiplexed Transmission of 56-Tb/s over a 76.8-km Seven-Core Fiber," *OFC/NFOEC Postdeadline Paper* (2011).

[12] T. Hayashi, T. Taru, O. Shimakawa, T. Sasaki, E. Sasaoka, "Ultra-Low-Crosstalk Multi-Core Fiber Feasible to Ultra-Long-Haul Transmission," *OFC/NFOEC Postdeadline Paper*(2011).

[13] X. Yi, W. Shie and Y. Tang, "Phase estimation for coherent optical OFDM," *IEEE Photon. Tech. Lett.* **19**, p. 919 (2007).

[14] E. Ip, and J. M. Kahn. "Digital equalization of chromatic dispersion and polarization mode dispersion," *J. Lightw. Technol.* **25**, p. 2033 (2007).

[15] G. P. Agrawal, *Nonlinear fiber optics*, 4th Ed., Academic Press (2007).

[16] I. Shake, H. Takara, K. Mori, S. Kawanishi, and Y. Yamabayashi, "Influence of inter-bit four-wave mixing in optical TDM transmission," *Electron. Lett.* **34**, p. 1600 (1998).

[17] R. J. Essiambre, B. Mikkelsen, and G. Raybon, "Intra-channel crossphase modulation and four-wave mixing in high-speed TDM systems," *Electron. Lett.* **35**, p. 1576 (1999).

[18] P. V. Mamyshev and N. A. Mamysheva, "Pulse-overlapped dispersion managed data transmission and intrachannel four-wave mixing," *Opt. Lett.* **24**, p. 1454 (1999).

[19] M. Eiselt, M. Shtaif and L.D. Garrett, "Contribution of timing jitter and amplitude distortion to XPM system penalty in WDM systems," *IEEE Photon. Tech. Lett.* **11**, p. 748 (1999).

[20] A. Mecozzi, C. B. Clausen, and M. Shtaif, "Analysis of intrachannel nonlinear effects in highly dispersed optical pulse transmission," *IEEE Photon. Tech. Lett.* **12**, p. 292 (2000).

[21] S. Kumar, "Intrachannel four-wave mixing in dispersion managed RZ systems," *IEEE Photon. Tech. Lett.* **13**, p. 800 (2001).

[22] A. Mecozzi, C. B. Clausen, and M. Shtaif, "System impact of intrachannel nonlinear effects in highly dispersed optical pulse transmission," *IEEE Photon. Tech. Lett.* **12**, p. 1633 (2000).

[23] M. Nazarathy, J. Khurgin, R. Weidenfeld, Y. Meiman, P. Cho, R. Noe, I. Shpantzer, and V. Karagodsky, "Phased-array cancellation of nonlinear FWM in coherent OFDM dispersive multi-span links," *Opt. Express* **16**, p. 15777 (2008).

[24] D. Yang and S. Kumar, "Intra-channel four-wave mixing impairments in

dispersion-managed coherent fiber-optic systems based on binary phase-shift keying," *J. Lightw. Technol.* **27**, p. 2916 (2009).

[25] A. Bononi, P. Serena, N. Rossi, E. Grellier, and F. Vacondio, "Modeling nonlinearity in coherent transmissions with dominant intrachannel-four-wave-mixing," *Opt. Express* **20**, p. 7777 (2012).

[26] A. Carena, V. Curri, G. Bosco, P. Poggiolini, and F. Forghieri, "Modeling of the impact of nonlinear propagation effects in uncompensated optical coherent transmission links," *J. Lightw. Technol.* **30**, p. 1524 (2012).

[27] A. Mecozzi, Rene Essiambre, "Nonlinear Shannon limit in pseudolinear coherent systems," *J. Lightw. Technol.* **30**, p. 2011 (2012).

[28] S. Turitsyn, M. Sorokina, and S. Derevyanko, "Dispersion-dominated nonlinear fiber-optic channel," *Opt. Lett.* **37**, p. 2931 (2012).

[29] S. Kumar and D. Yang, "Second-order theory for self-phase modulation and cross-phase modulation in optical fibers," *J. Lightw. Technol.* **23**, p. 2073 (2005).

[30] J. D. Jackson, *Classical Electrodynamics* (Wiley, 1998).

[31] U. Madhow, "Chapter 3: Demodulation," in *Fundamentals of Digital Communication* (Cambridge University Press, 2008).

[32] A. Carena, G. Bosco, V. Curri, P. Poggiolini, M. T. Taiba, and F. Forghieri, "Statistical characterization of PM-QPSK signals after propagation in uncompensated fiber links," in *Proceedings ECOC*, p. 1 (2010).

[33] M. Nazarathy, "Accurate evaluation of bit-error rates of optical communication systems using the Gram-Charlier series," *IEEE Trans. Commun.* **54**, p. 295 (2006).

[34] A. H. Gnauck, P. J. Winzer, A. Konczykowska, F. Jorge, J. Dupuy, M. Riet, G. Charlet, B. Zhu, and D. W. Peckham. "Generation and transmission of 21.4-Gbaud PDM 64-QAM using a novel high-power DAC driving a single I/Q modulator," *J. Lightw. Technol.* **30**, p. 532 (2012).

[35] S. Kumar, S. N. Shahi, and D. Yang. "Analytical modeling of a single channel nonlinear fiber optic system based on QPSK," *Opt. Express* **20**, p. 27740 (2012).

[36] D. Marcuse, A.R. Chraplyvy and R.W. Tkach, "Dependence of cross-phase modulation on channel number in fiber WDM systems," *J. Lightw. Technol.* **12**, p. 885, (1994).

[37] R. Hui, Y. Wang, K. Demarest and C. Allen, "Frequency response of cross-phase modulation in multispan WDM optical fiber systems," *IEEE Photon. Tech. Lett.* **10**, p. 1271 (1998).

[38] R. Hui, K. Demarest and C. Allen, "Cross-phase modulation in multispan WDM optical fiber systems," *J. Lightw. Technol.* **17**, p. 1018 (1999).

[39] A.T. Cartaxo, "Cross-phase modulation in intensity modulation-direct detection WDM systems with multiple optical amplifiers and dispersion compensators," *J. Lightw. Technol.* **17**, p. 178 (1999).

[40] Z. Jiang and C. Fan, "A comprehensive study on XPM-and SRS-induced noise

in cascaded IM-DD optical fiber transmission systems," *J. Lightw. Technol.* **21**, p. 953 (2003).

[41] S. Kumar, and D. Yang. "Second-order theory for self-phase modulation and cross-phase modulation in optical fibers," *J. Lightw. Technol.* **23**, p. 2073 (2005).

[42] J. Tang, "The channel capacity of a multispan DWDM system employing dispersive nonlinear optical fibers and an ideal coherent optical receiver," *J. Lightw. Technol.* **20**, p. 1095 (2002).

[43] Z. Tao, W. Yan, L. Liu, L. Li, S. Oda, T. Hoshida, and J. C. Rasmussen, "Simple Fiber Model for Determination of XPM Effects," *J. Lightw. Technol.* **29**, p. 974 (2011).

[44] P. Poggiolini, A. Carena, V. Curri, G. Bosco, F. Forghieri, "Analytical modeling of non-Linear propagation in uncompensated optical transmission links," *IEEE Photon. Tech. Lett.* **23**, p. 742 (2011).

[45] J. M. Kahn and K. P. Ho, "Spectral Efficiency Limits and Modulation/Detection Techniques for DWDM Systems," *IEEE. J. on Sel. Topics in Quantum Electron.* **10**, p. 259 (2004).

[46] S. Naderi Shahi and S. Kumar, "Reduction of Nonlinear Impairments in Fiber Transmission System Using Fiber Diversity," in Signal Processing in Photonic Communications (SPPCom), Toronto, Canada, June 2011.

[47] S. Kumar, U. Manyam and V.Srikant, "Optical fibers having cores with different propagation constants, and methods of manufacturing the same," US Patent #091/852173 (2003).

[48] D. Butler, M.-J. Li, B. J. Hoover, V. N. Nazarov, D. D. Fortusini, J. P. Luther, Y. Geng and R. R. Grzybowski, "Multicore Optical Fibers and Connectors for Short Reach, Computer Compatible, High Density Links," *IEEE Photonics Conference (IPC)* Burlingame, USA, September 2012.

[49] G. P. Agrawal, S. Mumtaz , and R-J Essiambre, "Nonlinear Performance of SDM Systems Designed with Multimode or Multicore Fibers," *OFC/NFOEC* (2013).

[50] G. J. Tearney, M. E. Brezinski, B. E. Bouma, S. A. Boppart, C. Pitris, J. F. Southern and J. G. Fujimoto, "In Vivo Endoscopic Optical Biopsy with Optical Coherence Tomography," *Science* **276**, p. 2037 (1997).

[51] N. S. Mohd Shah and M. Matsumoto, "Analysis and experiment of all-optical time-interleaved multi-channel regeneration based on higher-order four-wave mixing in a fiber," *Opt. Comm.* **284**, p. 4687 (2011).

[52] B. Zhang, L. S. Yan, J. Y. Yang, I. Fazal, and A. E. Willner, "A single slow-light element for independent delay control and synchronization on multiple Gb/s data channels," *IEEE Photon. Tech. Lett.* **19**, p. 1081 (2007).

[53] P. Krummrich, "Optical Amplifiers and Optical Filters for a Cost and Energy Efficient Realization of Spatial Division Multiplexing," invited talk in *Photonics North Conference* Ottawa, Canada, June 2013.

[54] T. S. Rappaport, *Wireless communications: principles and practice*, (Prentice Hall PTR 2002).

[55] D. Tse and P. Viswanath, *Fundamentals of wireless communication*, (Cambridge University Press, 2005).

[56] K. Cheun, "Performance of direct-sequence spread-spectrum RAKE receivers with random spreading sequences," *IEEE Transactions on Communications* **45**, (1997).

[57] M. Matsumoto, Y. Akagi, and A. Hasegawa, "Propagation of solitons in fibers with randomly varying birefringence: Effects of soliton transmission control," *J. Lightw. Technol.* **15**, p. 584 (1997).

[58] Z. Chen and S. Kumar, "A fiber-optic transmission system based on differential polarization-shift keying," *Opt. Comm.* **284**, (2011).

[59] W. Shie and C. Athaudage, "Coherent optical orthogonal frequency division multiplexing," *Electron. Lett.* **42**, p. 587 (2006).

[60] A.J. Lowery and J. Armstrong, "Orthogonal frequency division multiplexing for dispersion compensation of long haul optical systems," *Opt. Express* **14**, p. 2079 (2006).

[61] I.B. Djordjevic and B. Vasic, "Orthogonal frequency division multiplexing for high-speed optical transmission," *Opt. Express* **14**, p. 3767 (2006).

[62] W. Shieh, H. Bao and Y. Tang, "Coherent optical OFDM: theory and design," *Opt. Express* **16**, p. 841 (2008).

[63] K. Kikuchi and S. Tsukamoto, "Evaluation of sensitivity of the digital coherent receiver," *J. Lightw. Technol.* **26**, p. 1817 (2008).

[64] S. Kumar, U. Manyam and V.Srikant, "Optical fibers having cores with different propagation constants, and methods of manufacturing the same," *US Patent* #091/852173 (2003).

[65] C. Xie, "Interchannel Nonlinearities in Coherent Polarization-Division-Multiplexed Quadrature-Phase-Shift- Keying Systems," *IEEE Photon. Tech. Lett.* **21**, p. 274 (2009).

[66] J. Sakaguchi, Y. Awaji, N. Wada, T. Hayashi, T. Nagashima, T. Kobayashi, and M. Watanabe, "Propagation characteristics of seven-core fiber for spatial and wavelength division multiplexed 10-Gbit/s channels," in *OFC/NFOEC*, p. 1 (2011).

[67] H. Takara, A. Sano, T. Kobayashi, H. Kubota, H. Kawakami, A. Matsuura, Y. Miyamoto, Y. Abe, H. Ono, K. Shikama, Y. Goto, K. Tsujikawa, Y. Sasaki, I. Ishida, K. Takenaga, S. Matsuo, K. Saitoh, M. Koshiba, and T. Morioka, "1.01-Pb/s (12 SDM/222 WDM/456 Gb/s) Crosstalk-managed Transmission with 91.4-b/s/Hz Aggregate Spectral Efficiency," *ECOC Postdeadline Paper* (2012).

[68] S. N. Shahi, and S. Kumar, "Reduction of nonlinear impairments in fiber transmission system using fiber and/or transmitter diversity," *Opt. Comm.* **285**, p. 3553 (2012).

[69] E. Ip, and J. M. Kahn, "Compensation of Dispersion and Nonlinear Impairments Using Digital Backpropagation," *J. Lightw. Technol.* **26**, p. 3416 (2008).

[70] L. B. Du, and A. J. Lowery, "Improved single channel backpropagation for intra-channel fiber nonlinearity compensation in long-haul optical communication systems," *Opt. Express* **18**, p. 17075 (2010).